Title
System Hardware and in vivo Cell Tracking in Magnetic Particle Imaging

Author
Zheng, Bo

Publication Date
2015

Peer reviewed|Thesis/dissertation

System Hardware and *in vivo* Cell Tracking in Magnetic Particle Imaging

by

Bo Zheng

A dissertation submitted in partial satisfaction of the
requirements for the degree of
Joint Doctor of Philosophy
with University of California, San Francisco

in

Bioengineering

in the

Graduate Division

of the

University of California, Berkeley

Committee in charge:

Professor Steven Conolly, Chair
Professor Chris Diederich
Professor Seth Sanders

Summer 2015

System Hardware and *in vivo* Cell Tracking in Magnetic Particle Imaging

Abstract

System Hardware and *in vivo* Cell Tracking in Magnetic Particle Imaging

by

Bo Zheng

Joint Doctor of Philosophy
with University of California, San Francisco in Bioengineering

University of California, Berkeley

Professor Steven Conolly, Chair

Magnetic Particle Imaging (MPI) is an emergent medical imaging technology that directly images the intense magnetization of clinically safe superparamagnetic iron oxide (SPIO) nanoparticles. Because biological tissues do not produce signals detectable in MPI scanners, MPI images have extremely high image contrast and sensitivity for SPIO tracers, akin to nuclear medicine imaging techniques. The MPI signal is also linearly proportional to SPIO tracer concentrations in the imaging volume, making it a truly quantitative imaging technique. Hence, because of its high image contrast, sensitivity, quantitativeness, and tracer safety, MPI may be useful in applications ranging from coronary angiography to stem cell therapy tracking and is extremely promising for translation to the clinic.

The physical basis behind signal generation in MPI is unlike that of any other imaging modality, giving MPI the potential to be one of the most sensitive medical imaging modalities. However, several limitations have prevented existing MPI scanners from reaching the physical limits of detection sensitivity. These limitations include direct feedthrough interference from the MPI transmitter to the receiver, which can obscure the desired SPIO magnetization signal and limit SNR. In Chapter 2 of this dissertation, I aim to determine the sources of interference generation in MPI scanners and to develop engineering solutions to attenuate the feedthrough interference in the detected signal spectrum. My results indicate that feedthrough interference can arise from high-power passive components used to generate the MPI drive fields, as well as from the interaction between the MPI drive field and the magnets used to generate the MPI magnetic field gradient. To remove these interfering signals for improved detection sensitivity, I designed an actively-controlled magnetic interference cancellation system using a Cartesian feedback controller. Data from this active cancellation system has shown the ability to suppress interfering MPI signals by over 55 dB.

Another limitation in the sensitivity of existing MPI scanners is the use of non-optimized electronics in the MPI detector chain, which can add substantial noise beyond the noise mechanisms generated in the patient and in the detector coil. In Chapter 3 of this dissertation, I investigate the sources of electronic noise in MPI and describe three methods

to reduce noise from the MPI detector preamplifier to below the noise generated by the MPI detector coil. Using these noise-matching techniques, I then describe the design and implementation of a custom transformer-coupled MPI preamplifier. Finally, using a 7 T/m preclinical MPI scanner, I demonstrate that the custom MPI preamplifier can achieve an 11-fold improvement in the signal-noise ratio (SNR) of MPI scanners over a commercially available low-noise preamplifier.

Building upon these improvements in the sensitivity and SNR of our preclinical MPI scanners, I then perform the first two *in vivo* experiments to track implanted stem cell therapies in rodent models. In Chapter 4, we show that MPI can be used to sensitively and quantitatively track stereotactically implanted neural progenitor cell xenografts over an 87-day period. In Chapter 5, we show the first use of MPI to systemically monitor intravenously implanted therapeutic cells. MPI was able to visualize the entrapment of large mesenchymal stem cells in lung vasculature during circulation and quantify the gradual clearance of these cells through the liver over a period of 12 days. Importantly, these experiments demonstrate the ability of MPI to sensitively trace small quantities of SPIOs in the body, potentially enabling new clinical approaches to metastatic cancer detection and the diagnosis of other systemic diseases.

To Fred Nashold, the greatest mentor that I could have ever known.

Acknowledgments

My graduate advisor, Prof. Steve Conolly, always said that grad school is a marathon, not a sprint. He couldn't be more right. Through this journey with him, I learned not only the concrete technical expertise to break any system down to its physical equations, the virtues of engineering robust systems based on solid physical intuition, and the importance of a good presentation and writing style, but I also learned about what it means to be steadfast in persevering toward a goal. Steve also exemplifies the virtue of caring for others, no matter how distant their interests and background may be from his own. I have seen many times now how Steve can agonize over the difficulties of graduate students who are not his own and how he does everything in his power to ensure their well-being and success in school. These are lessons I have learned that reach beyond academia and career; I am both extremely fortunate and grateful to have had a teacher like Steve.

I also want to thank Dr. Patrick Goodwill, with whom I have had the pleasure of working together for the past 6 years. Patrick is superhuman; it remains hard for me to fathom that so much engineering knowledge, physical intuition, and problem-solving prowess can be packaged into one person. Without Patrick, there is no way I could have learned or accomplished so much in my PhD career. He patiently helped me almost every step of the way with each of my projects and always provided interesting new directions when I would become stuck. Patrick inspires me to do likewise, that I might become a nurturing presence for others to learn and grow.

All of my labmates in the Conolly lab have made our lab one of the most fun work environments at Berkeley. Actually, I can't really believe that we were able to do much work at all, because we were constantly talking and having a great time. I want to thank Dr. Gary Lee and Xinyi Zhou for their constant supply of confectionary goods. I am thankful for my good friends Daniel Hensley, Elaine Yu, Ryan Orendorff, and Paul Keselman, who have been a most interesting and opinionated group and have constantly pushed me to be at my technical best. I am also extremely grateful to the undergraduate researchers who have worked with me: Wisely Yang, Neerav Dixit, Di Xiao, John Zhang, Mindy Bishop, and Beliz Gunel, who soldered 200-pound filter boxes, designed low-noise circuits, debugged late at night, came up creative coil designs, and generally kept me more on my toes than I expected (or enjoyed, sometimes). They are an incredible group who, I am certain, will excel in their graduate school experience and future endeavors. I want to especially acknowledge our excellent and industrious lab manager, Robert Frawley, who has taken on all of the real challenges in research - money and logistics - and thus made it a joy for us to be able to conduct research. I am grateful to Drs. Laura Rose Croft and Justin Konkle, together with whom I began to explore the field, attended my first conferences, taught courses, and grew as researchers. Finally, I want to thank Prof. Emine Saritas, whose constant warm and patient presence always set all of our hearts at ease.

I also want to acknowledge all of the sources of my research funding over the years: the Siebel Scholars Foundation, NSF GRFP under grant number DGE 1106400, NIH 1R01 EB013689, CIRM RT2-01893, Keck Foundation 009323, NIH 1R24 MH106053 and NIH

1R01 EB019458, and ACTG 037829. The support of these organizations have enabled MPI technology to develop and mature over the years.

On a more personal note, I want to thank my family for bearing with me these many years in grad school. My mom has always been extremely supportive of me. It was not easy for her to raise a family in America, which was a new and foreign country for me. Many times she has considered other options beside staying here, but each time she decided to stay in America for my sake. This is as much her PhD as it is mine. My father's family in China has also been an unending source of support for me and I feel constantly loved by their care and concern. I also especially want to thank my late stepfather, Fred, whose passion for learning has inspired my own. He was an amazingly patient and loving man, being slow to anger and quick to teach. He instilled in me the values of listening more than speaking and considering the needs of others before oneself. Without his presence in my life, I would be a very different person. Truly he is the greatest mentor that I could have ever known.

I am beyond blessed to have Kuan Lu as my wife and my best friend. We first met during our research rotation in Steve's lab six years ago and have been together ever since. We have since gone through the ups and downs of school and life together. During times of trouble, we have carried each others' burdens. Even as she was so busy with her own research, Kuan always made time for me: taking care of me when I was sick, being patient with me as I trudged through writing, and comforting me when research was not working well. In many ways she is my opposite, being constantly optimistic and outgoing while I am brooding and frustrated. Her energy recharges me; her faith anchors me; and her presence is a stabilizing force in my life.

Finally, I want to thank God for all of these people that He has blessed me with. Growing up, I actually pushed many people away because of my competitiveness and a constant desire to be the best. My competitiveness and pride actually hurt many people in my life, including my friends and family. Coming to graduate school in Berkeley, I never expected to meet a group of friends who were Christian graduate students, who seemed to genuinely care for each other as they strove to live out the Bible. They cooked for others who were sick despite their own busy schedules, they made care packages for people taking quals, they prayed for one another, they pushed each other daily to become more Christ-like people. Noticing their love for one another and even for someone new like me, I was curious and began a long investigation into what the Bible taught, the compatibility of science and faith, and about myself. I realized that my initial life direction was fueled by competitiveness, which was in turn fueled by a desire for approval and a sense of worth. I also learned that God's love is unconditional through Jesus, and accepting this love, I became Christian through grad school. Afterwards, I began to notice and appreciate much more of the things that I have. It didn't have to be the case that I have such a great advisor, meaningful research, a loving family, or great friends and a great church. So instead of becoming more competitive, I gradually became more thankful. Now, I am confident that no matter what happens in my life, I can choose to be thankful and secure in God.

Contents

List of Figures

List of Tables

Chapter 1

Introduction to Magnetic Particle Imaging

1.1 Magnetic Particle Imaging is a safe tracer imaging modality for clinical diagnostic applications

Magnetic Particle Imaging (MPI) is an emerging imaging technique that directly images superparamagnetic iron oxide (SPIO) tracers. The signal contrast in MPI images is only generated by SPIOs in the body; there is no signal from native biological tissue [1, 2, 3]. This high image contrast and contrast-to-noise ratio for SPIO tracers in MPI is ideal for detecting and diagnosing small disease features that would otherwise be difficult to detect with anatomical imaging modalities such as MRI or CT [4]. MPI is therefore best compared to nuclear medicine techniques like Positron Emission Tomography (PET) and Single Photo Emission Computed Tomography (SPECT), which are the only available tracer imaging technologies currently in clinical use. Unlike PET and SPECT, however, MPI does not use ionizing radiation, and the SPIO tracers used in MPI are not radioactive and are safe for injection into the body even at significant doses for iron-deficiency anemia treatment [5, 6, 7].

MPI was invented and first demonstrated experimentally in 2005 by Gleich and Weizenecker at Philips Research in Hamburg, Germany [1]. Since then, there has been significant effort to expand the field toward improving system hardware for resolution and sensitivity improvement, developing the underlying systems theory for MPI (akin to the development of k-space techniques and pulse sequences for MRI), improving the SPIO nanoparticles in MPI for higher resolution and circulation time, and making MPI scanners available for clinical translation. In 2010, the first International Workshop on Magnetic Particle Imaging was held in Lübeck, Germany with 70 attendees. This number increased to around 200 in 2012 and continues to grow. The IWMPI conference has since also been held in Berkeley, CA, Berlin, Germany, and Istanbul, Turkey.

There are currently at least 7 groups in the world with operating custom-built MPI scan-

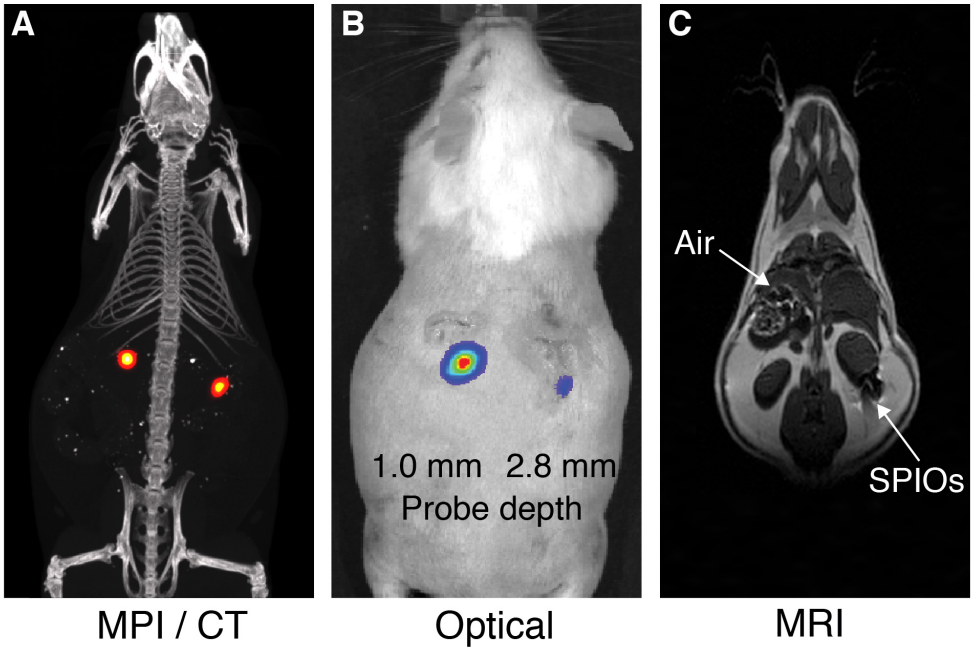

Figure 1.1: *In vivo* comparison of MPI/CT, fluorescent imaging, and MRI. Two probes filled with a mixture of Nanomag-MIP SPIOs and Angiosense 680 EX fluorescent probe were implanted 1.0 mm and 2.8 mm below the dorsal skin surface of a mouse. (A) A representative MPI image directly visualizes SPIO tracer with high image contrast and no signal modulation by biological tissue. MPI: 5 × 3.75 × 10 cm FOV, 6.8 min scan. CT: 15 min scan, 184 µm isotropic resolution. (B) Fluorescent imaging of implanted probes shows a decrease in signal with tissue depth. Fluorescent imaging: 5 sec scan. (C) In magnetic resonance images, the presence of SPIO tracer corresponds to a signal dropout similar to those generated at air-tissue interfaces. MRI: 4 × 8 cm FOV, 313 µm in-plane resolution, 17 min scan.

ners at Philips, UC Berkeley, University of Lübeck in Germany, Bruker Biospin, University of Würzburg, the Technical University of Braunschweig, and Osaka University [3, 8, 9, 10, 11, 12]. As the MPI field is nascent and a standard MPI system theory has not been established, each group uses differing and rapidly evolving scanner designs, pulse sequences, and reconstruction schemes. Commercial scanners are being developed for both clinical (Philips Healthcare, Netherlands) and preclinical (Bruker Biospin, Germany and Magnetic Insight, Inc, California) use. A Bruker preclinical small-animal imaging MPI scanner is estimated to become available commercially within the next several years [13].

At UC Berkeley, the development of Magnetic Particle Imaging was started by Patrick Goodwill and Prof. Steven Conolly in 2006. Since then, the Berkeley group has designed and constructed 8 generations of scanners, each building upon the advances made in the lab

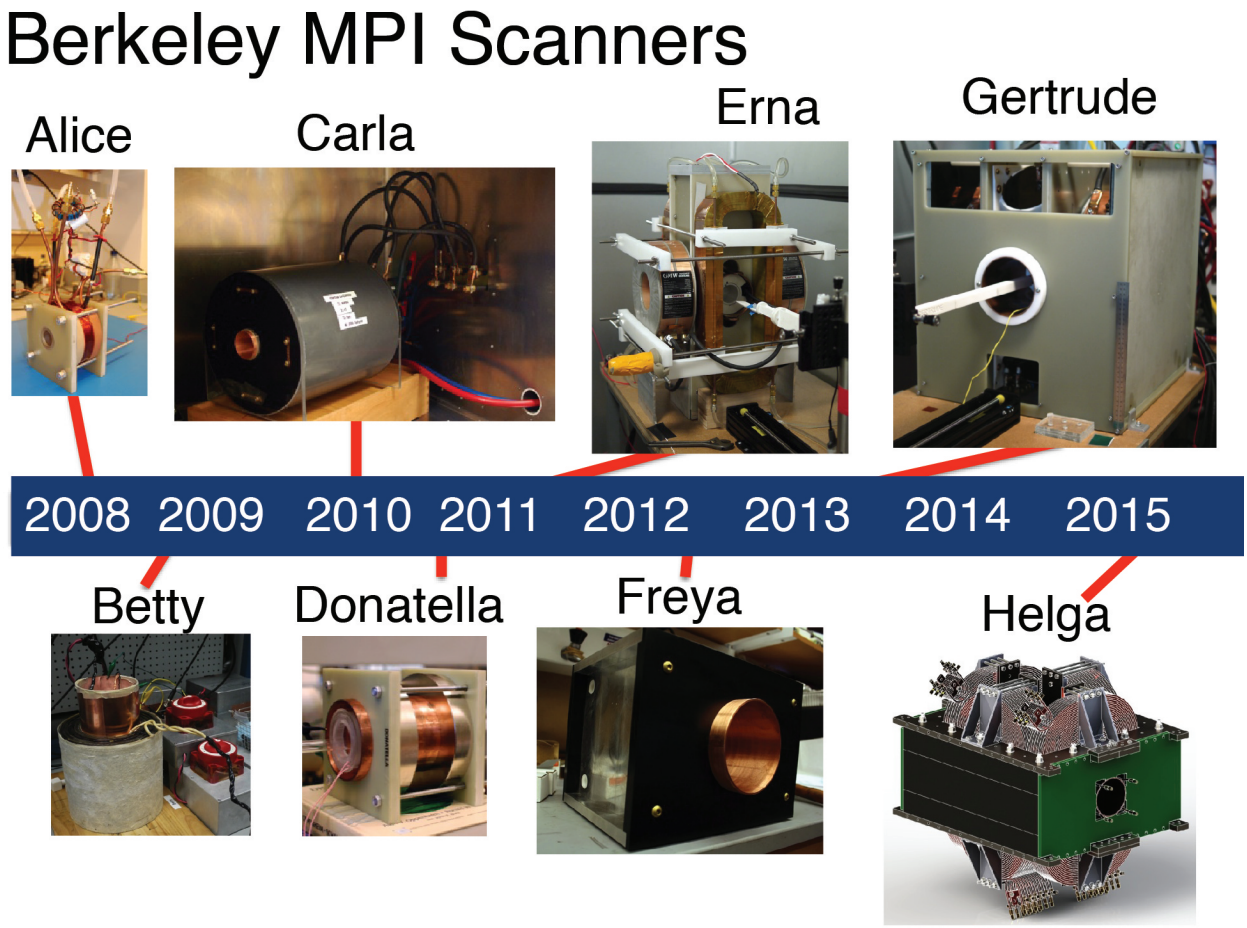

Figure 1.2: MPI scanners developed at UC Berkeley since 2006. Each generation of MPI scanner design improves upon the previous generation in spatial resolution and sensitivity, based on recent theoretical and hardware advancements in MPI.

for improving system sensitivity, resolution, and scanning speed, seen in Fig. 1.2. Our most recent scanner has achieved 50 ng iron detection sensitivity at 1 mm isotropic resolution for small animal imaging, which is comparable with small animal PET/SPECT spatial resolution and can still be improved with better scanner design and more optimized SPIO nanoparticles.

As a safe tracer imaging technique, MPI has the potential to replace many existing methods for disease diagnosis in the clinic. In the next sections, we describe two future clinical applications of Magnetic Particle Imaging that may enable disease diagnosis with greater safety and sensitivity than existing imaging modalities.

Figure 1.3: MPI imaging of human-scale coronary angiogram phantom. $9 \times 4 \times 4$ cm field-of-view (FOV), 10 minute scan. Image courtesy Dr. Justin Konkle.

1.1.1 MPI for safer angiography and blood volume imaging

Heart disease remains the top cause of death in America. In 2009, heart disease accounted for six hundred thousand deaths in America, or approximately one quarter of all deaths nationwide [14]. A key method in the diagnosis of atherosclerosis-based heart disease is angiography, or an imaging method to visualize occlusions in vasculature. X-ray angiography with iodinated contrast agent is the most commonly used angiographic method, with over 8 million procedures performed in 2006. Computed tomography (CT) angiography, also using iodinated contrast agents, is performed around 4 million times/year in the United States [15, 16]. In conventional X-ray angiography, an iodine-based contrast agent is injected directly into the coronary arteries via a catheter and visualized using fluoroscopic X-ray imaging in real time. In CT-based angiography, iodine contrast agents are injected intravenously and imaged post-injection via a 3D CT scan. These techniques have exquisite sensitivity and specificity for diagnosing heart disease. X-ray angiography has remained the gold standard diagnostic technique for over 50 years.

However, patients with chronic kidney disease (CKD) face significant risk of kidney damage from the most common contrast agents used in conventional angiography, which are iodine and gadolinium. CKD patients constitute 25% of all patients undergoing angiographic procedures each year in the US. Unfortunately, up to 20% of CKD patients undergoing iod-

inated X-ray/CT angiography develop contrast-induced nephropathy, which has a one-year mortality rate of over 22% [17, 18]. Moreover, 9% of late-stage CKD patients undergoing gadolinium-based magnetic resonance angiography develop nephrogenic systemic fibrosis, which arises due to an inability to clear the gadolinium contrast agent in patients with renal failure [5, 19, 20]. CKD patients that develop nephrogenic systemic fibrosis have a one-year mortality of 67% [21, 22]. As a result, gadolinium-based MR angiography is contraindictated for late-stage CKD patients.

An ideal angiographic method for CKD patients would use safe contrast agents while maintaining or improving image sensitivity, resolution, and contrast over existing modalities. The iron oxide nanoparticles used in MPI are not only safe for CKD patients, they are commonly used as therapeutic iron supplements for the treatment of iron-deficiency anemia in the CKD patient population [5, 7]. Hence, we can potentially use MPI as a safe replacement technique for angiography for CKD patients. Moreover, because MPI only sees the presence of SPIO particles in the imaging volume and no biological tissue background, its image contrast may exceed that of conventional angiography for greater diagnostic sensitivity and specificity of heart diseases. An example MPI image of a coronary angiogram phantom is shown in Figure 1.3.

1.1.2 MPI for dynamically tracking cell-based therapeutics *in vivo*

Stem cell-based therapies hold tremendous therapeutic potential for treating many degenerative and debilitating diseases, such as myocardial infarction, stroke, spinal cord injuries, and Parkinson's disease. The evaluation of cell transplantation efficacy and integration currently relies on destructive analytical methods like histology or functional improvements that can take months to manifest [23]. Inaccuracies in cell localization during initial deliver are common, with one clinical study reporting a 50% misadministration rate by experienced operators under ultrasound guidance [24]. Late detection of such outcomes can seriously impact the development of cell-based therapies. Clinical translation and adoption of cell therapies could be accelerated by safe, quantitative *in vivo* imaging methods [25].

All standard preclinical imaging modalities have been used to track cells *in vivo* with varying degrees of success [25]. Few existing tracer imaging modalities can quantitatively image injected cells over a weeks- or months-long timescale without the use of genetically encoded reporter tracers, which are challenging for clinical translation [25]. Nuclear medicine is an exquisitely sensitive and high-contrast technique that images radioactive tracers, but faces limitations in tracer half-life and radioactive dose for longitudinal imaging. Fluorescent and bioluminescent imaging are the most common preclinical cell-tracking techniques; however, they are limited in their ability to image tracers deep in tissue, which prevents quantification, real-time dynamic cell tracking, and clinical translation. 19F MRI, which detects the nuclear magnetism of fluorine atoms, is a promising positive-contrast imaging technique that has shown success for cell-tracking [26, 27]. It remains to be seen whether

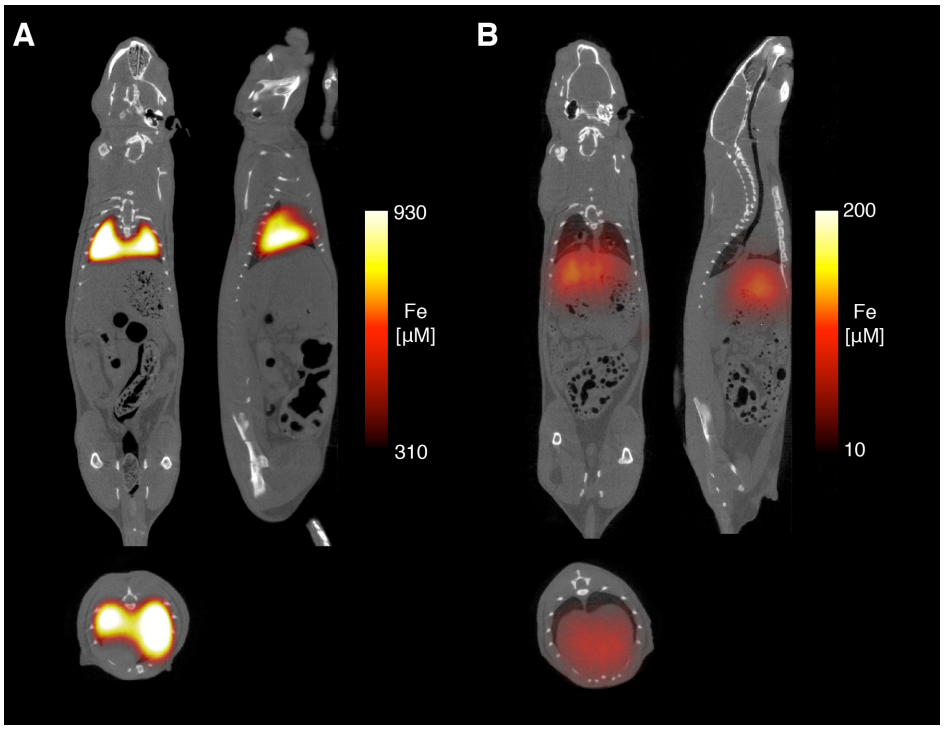

Figure 1.4: MPI-CT imaging of intravenously injected mesenchymal stem cells labeled using Resovist SPIO tracer, with representative coronal, sagittal, and axial slices shown from full 3D MPI datasets. (A) MPI imaging of mesenchymal tail vein injections at less than one hour post-injection shows substantial cell localization to lung tissue. (B) 12 days after injection, mesenchymal tail vein injections show significant total clearance and liver migration. MPI imaging (n = 4 for each animal): $4 \times 3.75 \times 10$ cm FOV, 9 minute acquisition. CT imaging: 25 minute acquisition, 184 µm isotropic resolution.

19F MRI can be used for whole-body cell tracking, particularly for organs near tissue-air susceptibility boundaries, such as lungs or the GI tract.

Clinically, most cell tracking studies have used SPIO labeled cells, because SPIO-based methods have minimal effects on cell viability, proliferation, and differentiation [28, 29, 30, 31], along with excellent depth penetration and *in vivo* persistence measured in months. However, the primary challenge for MRI-based SPIO cell tracking is that SPIOs induce MRI signal dropouts that are difficult to distinguish from tissues with naturally low MRI signal (e.g., bones, tendon, lungs, or any tissues near air). Moreover, MRI methods with positive contrast suffer from robustness and sensitivity challenges [32, 27]. Until now, no technique has been able to combine high specificity with sensitive and quantitative imaging of the distribution and *in vivo* fate of SPIO-labeled cells [25, 28].

Magnetic Particle Imaging, which directly images the intense magnetization of SPIOs rather than indirectly detecting SPIOs via MRI signal dropouts, is a unique addition to

this repertoire of existing stem-cell tracking technologies. MPI images SPIO tracers deep in tissue with high image contrast and high quantitative accuracy compared to fluorescent and T_2* MR imaging (Fig. 1.1). The SPIO tracers used in MPI are equivalent to to those used in MRI and have been shown to be safe for both clinical use and cell labeling [33, 34, 35, 36]. Specifically, cells labeled using SPIOs show no decrease in cell viability, proliferation, or differentiation. In addition to the safe SPIO tracer, MPI uses safe low frequency magnetic fields that are non-ionizing, making it a safe tool for clinical cell tracking applications.

In Chapters 4 and 5 of this dissertation, we describe the first *in vivo* use of MPI to track labeled stem cells. Specifically, in Chapter 4 we describe the use of MPI to longitudinally monitor neural cell grafts, which are being investigated for clinical applications ranging from stroke repair to Parkinson's disease, over a period of three months . In Chapter 5, we show that MPI can be used to quantitatively monitor the dynamic biodistribution of intravenously injected mesenchymal cells, which show therapeutic promise for their immunomodulatory effects *in vivo*.

1.2 MPI theory and system architecture

In this section, we will explore the nature of signal generation and spatial localization in MPI. We first describe the magnetic properties of the superparamagnetic iron oxide tracers used in MPI. To date, the SPIO tracers used in MPI have been composed of an iron oxide core at sizes ranging from 10-25 nm with an organic coating, typically comprised of dextran or carbodextran [37, 33].

At these particle core sizes, the bulk magnetization of SPIO particles increases and quickly saturates in response to an externally applied magnetic field. This process can be analytically described using a nonlinear Langevin equation [1]. Typical magnetic field strengths to cause SPIOs with core sizes on the order of 15-25 nm to saturate in magnetization range around 8-15 mT. As an example, when a strong, time-varying magnetic field from -20 mT to 20 mT is applied to a distribution of SPIOs, bulk SPIO magnetization responds by traversing its entire nonlinear magnetization curve from saturation in the negative direction to the positive direction (Fig. 1.5).

If we place a detector coil near the distribution of SPIOs, this time-varying SPIO magnetization produces a detectable voltage signal according to Faraday's law of induction. Hence, if we apply a linearly ramping magnetic field to a population of SPIOs, the voltage signal induced in the detector coil is exactly the derivative of the SPIO magnetization curve. This Langevin derivative (Fig. 1.5) forms the basis of the MPI image blurring function, or point-spread function (PSF), and ultimately determines the spatial resolution of MPI images [2].

To spatially localize the SPIO signal for imaging, we apply a static magnetic field gradient, which saturates the magnetization of all SPIOs in the imaging field-of-view except those in the central field-free region (shown as a field-free point, or FFP, in Figure 1.6). To form an MPI image, the FFP is rastered across the entire 3D field-of-view (FOV) using a

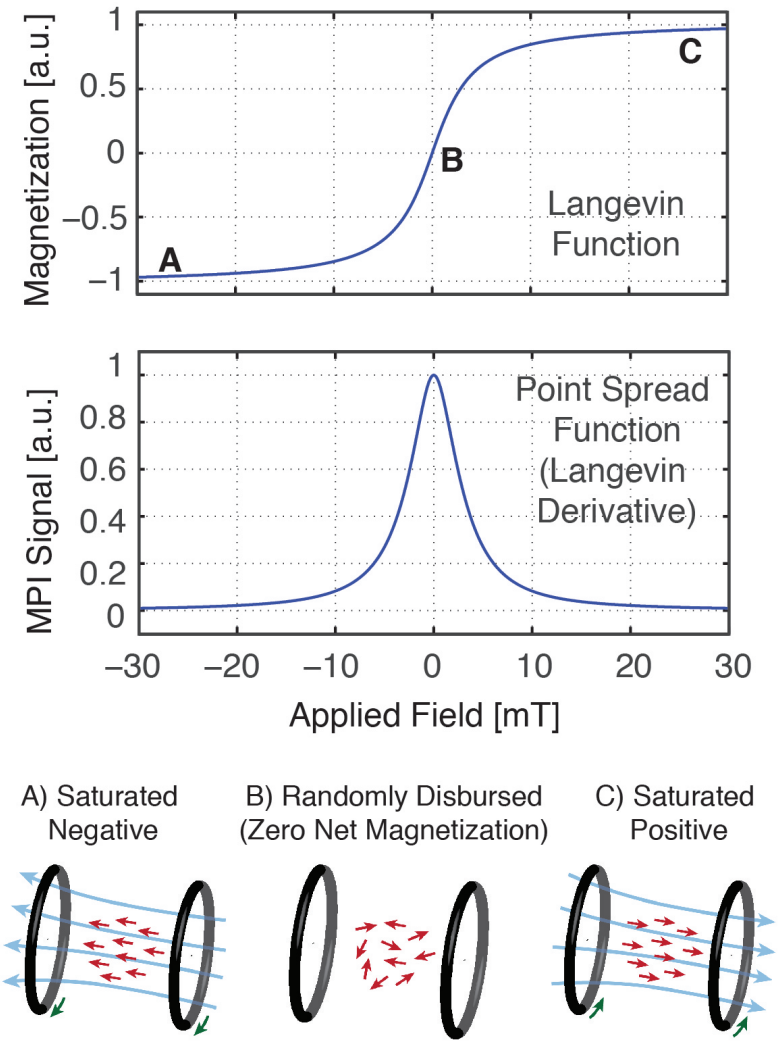

Figure 1.5: Magnetic properties of SPIO tracers used in MPI. The bulk SPIO magnetization is a nonlinear function of an externally applied magnetic field and saturates in bulk magnetization at high applied magnetic fields. This nonlinear SPIO magnetization can be described using a Langevin model. In MPI, an externally applied magnetic field from a drive coil causes SPIOs in the imaging volume to traverse curve. A detector coil then inductively detects the changing SPIO magnetization, which is the time-derivative of the Langevin curve. This Langevin derivative forms the basis of the image blurring function, or the point spread function (PSF), in MPI.

combination of electromagnets (shown in Fig. 1.7). As FFP traverses a location containing SPIOs, SPIO magnetization at that location changes in both magnitude and orientation in

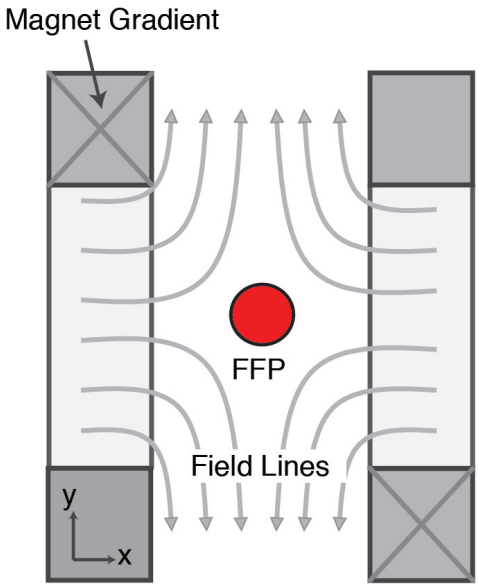

Figure 1.6: A magnetic gradient field saturates all SPIOs except those in a central field-free region for spatial localization in MPI. SPIO particles at the field-free region, shown here as a field-free point (FFP), are not saturated in magnetization, whereas SPIO particles outside the FFP are magnetically saturated. Hence, by moving the FFP across a spatial distribution of SPIO particles, we can cause the particles to de-saturate and re-saturate in magnetization. This time-varying particle magnetization can be detected using a detector coil.

response [38]. The resulting voltage signal sensed via a detector coil can then be assigned to the instantaneous FFP location to form the final MPI image.

Thus far, there have been two predominant methods to perform scanning and image construction in MPI. The imaging and reconstruction process described above is commonly referred to as the x-space MPI scanning method and relies on image reconstruction directly from the nanoparticle magnetization signal and knowledge of the instantaneous FFP location. We have previously proven that x-space MPI is linear and shift-invariant as an imaging system [2, 39]. As a result, MPI images can be used to quantify SPIO tracer *in vivo* anywhere in the imaging volume.

Another approach for MPI scanning, called the system function approach, has been championed by Philips MPI researchers since the invention of MPI [1]. Briefly, in the system matrix scanning technique, the entire MPI scanning process (which includes the imaging trajectory, particle signal generation, detector coil sensitivity, and spatial localization of SPIO signal) is encapsulated into a single system matrix [1, 40]. This system matrix is probed and characterized via the use of a calibration scan, where a point source of SPIOs is rastered to every position within the imaging volume and distinct MPI voltage signals are acquired at each SPIO location. This input (SPIO location) to output (voltage signals at the

detector) relationship is then used to build the system matrix (on the order of gigabytes or larger) that characterizes the MPI system. For actual imaging, a subject is scanned using the same imaging parameters as the calibration scans in the MPI scanner. The detected voltage signals from the MPI scan is multiplied by the inverse of the calibrated system matrix via an optimization algorithm using several regularization parameters to reconstruct the particle image. Unfortunately, it has been shown that the use of regularization parameters may cause the reconstructed images to no longer be linear and shift-invariant and may additionally introduce image artifacts during reconstruction [41]. As the MPI field continues to develop rapidly, an optimized scanning and reconstruction scheme remains an active and exciting area of investigation.

Despite the differing approaches toward MPI scanning and image reconstruction, most MPI scanner hardware architecture designs and implementations are remarkably similar. For both preclinical and clinical MPI imaging, three sets of magnetic field generators are necessary. The first magnetic field needed is a static gradient field used to generate a field-free region, which can be in the form of either a field-free point or a field-free line (FFL). The static gradient field itself has been previously generated using either electromagnets or permanent magnets [42, 3] and may be generated using superconducting magnets in future clinical designs. A schematic and photo of the permanent neodymium iron-boride gradient magnets for a 7 T/m FFP MPI scanner constructed at UC Berkeley is shown in Fig. 1.7.

In addition to the gradient field magnets, electromagnets are necessary to shift the field-free region across the entire imaging volume. As the field-free region is shifted across a location with SPIOs, SPIO magnetization changes rapidly to produce a detectable signal. To create this time-varying magnetic field, a spatially homogeneous, time-varying electromagnet is used. This magnet is called a drive coil in MPI. To achieve high SNR in MPI, the drive field needs to be rastered quickly across the imaging volume. The drive field is typically generated using a resonant inductor at around 25 kHz, although higher frequencies are also feasible. The amplitude of the drive field can be limited by power losses in the drive coil or power amplifier and ultimately by magnetostimulation limits in the patient [43]. However, because the imaging FOV is directly proportional to the drive field amplitude [2], limitations in the drive field amplitude due to magnetostimulation safety limits or power constraints would cause limitations in the maximum achievable imaging volume.

To extend the imaging FOV, a third magnetic field is needed to shift the field-free region slowly across the entire imaging FOV. Unlike the drive field, this slow-shift field does not need to excite the SPIO particle magnetization and therefore can be driven slowly to avoid magnetostimulation effects in the patient. Depending on the scanner geometry, two or three sets of electromagnets are needed to shift the field-free region to cover the entire imaging FOV. Therefore, the instantaneous magnetic field in MPI can be regarded as a superposition of three magnetic fields: the static gradient field to generate a field-free region, the quasi-static slow-shifting field to spatially offset the imaging FOV, and the drive field to rapidly raster the field-free region for inducing SPIO tracer magnetization signals.

This system hardware architecture in MPI is unique and completely distinct from the designs of existing medical imaging systems, leading to specific hardware challenges for

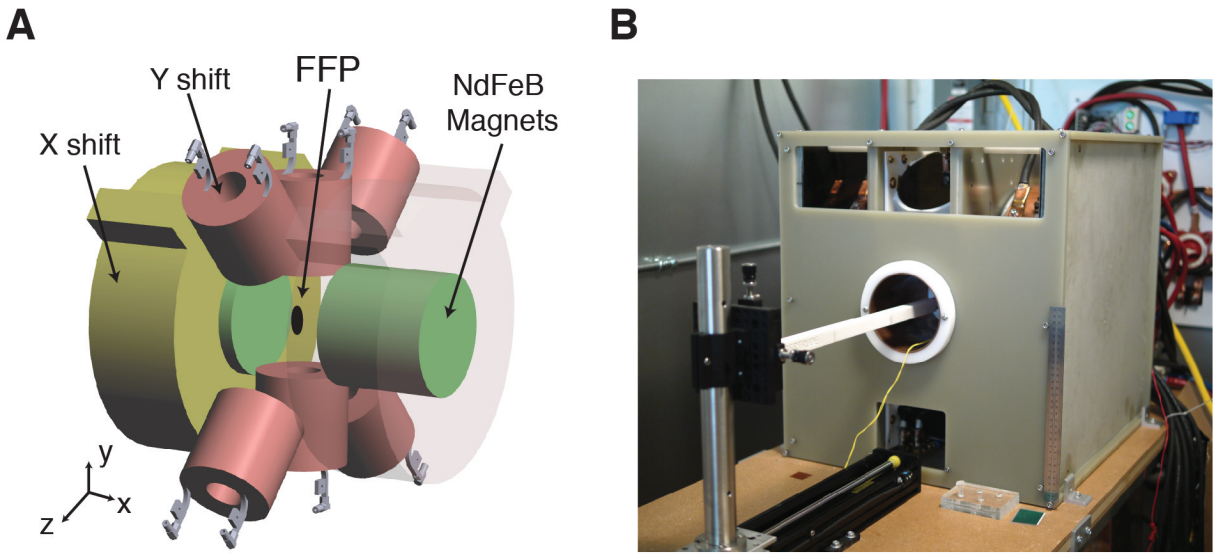

Figure 1.7: Diagram of magnets used in MPI scanning. (A) MPI scanners are comprised of three sets of magnetic field generators. First, a pair of magnets create a static magnetic field gradient. In the UC Berkeley MPI scanner shown here, a pair of opposing neodymium iron-boride permanent magnets create a 7 T/m magnetic gradient along the X direction and 3.5 T/m gradient along the Y and Z directions, with a central field-free point (FFP). Second, the FFP can be shifted slowly throughout the imaging volume via electromagnets in the X and Y directions to cover the entire scanning FOV. Last, a drive coil (not shown) rapidly translates the FFP in the Z direction to excite SPIO magnetization that can be detected using a detector coil. (B) Photograph of UC Berkeley MPI scanner with assembled magnets.

achieving optimal tracer detection sensitivity and image signal-to-noise ratio. In the following chapters, we will introduce and address two major challenges in MPI scanner sensitivity: feedthrough interference between the drive field system and the detector coil (Chapter 2) and optimal noise matching for the MPI detector (Chapter 3). Based on these hardware improvements, we then describe the first studies using MPI to image, quantify, and track the biodistribution of SPIO-labeled cells implanted *in vivo* in a neural cell transplant model over 3 months (Chapter 4) and in a preclinical mesenchymal cell therapy model (Chapter 5).

Chapter 2

Drive Field Interference Suppression in MPI

2.1 Introduction to Feedthrough Interference in the MPI Drive Field

Magnetic Particle Imaging is a medical imaging modality that uses low-frequency magnetic fields to probe inside the body for visualizing implanted SPIO tracers with exquisite image contrast. The theory and method of operation for MPI scanners is unlike that of any other medical imaging modality. As described in Chapter 1, three magnetic fields are required in the operation of an MPI scanner. First, a static magnetic gradient field generates a magnetically field-free region, such as a field-free point (FFP), outside of which all SPIO particle magnetization is saturated. Then, a set of slow-shift electromagnets positions the FFP in 3D within a specified location in the imaging FOV. Finally, a time-varying homogeneously rasters the FFP within the FOV. As the FFP traverses a location containing SPIOs, the SPIOs at that location instantaneously change the amplitude and orientation of their magnetization in response to the drive field. For image reconstruction, this changing SPIO magnetization signal can be detected using a detector coil and assigned to the instantaneous FFP location [39, 2].

To generate power-efficient drive fields in MPI, the typical drive field is a sinusoidally time-varying, spatially homogeneous magnetic field. These fields are easily generated using resonant inductors (called drive coils) at around 25 kHz and 10-60 mTpp field amplitude [2, 44, 1, 45]. A diagram of the MPI drive field and detector system architecture is shown in Fig. 2.1. Briefly, a digital time-varying sinusoid signal is converted to an analog voltage signal and amplified using a commercially available linear power amplifier. The high-voltage signal is then filtered for spectral purity using a bandpass filter and transmitted as a time-varying magnetic field using a resonant drive coil. On the detector side, the detector coil receives both the time-varying particle magnetization signal and the simultaneous, but undesirable, drive field signal. The sinusoidal interfering drive field signal is filtered from the detector

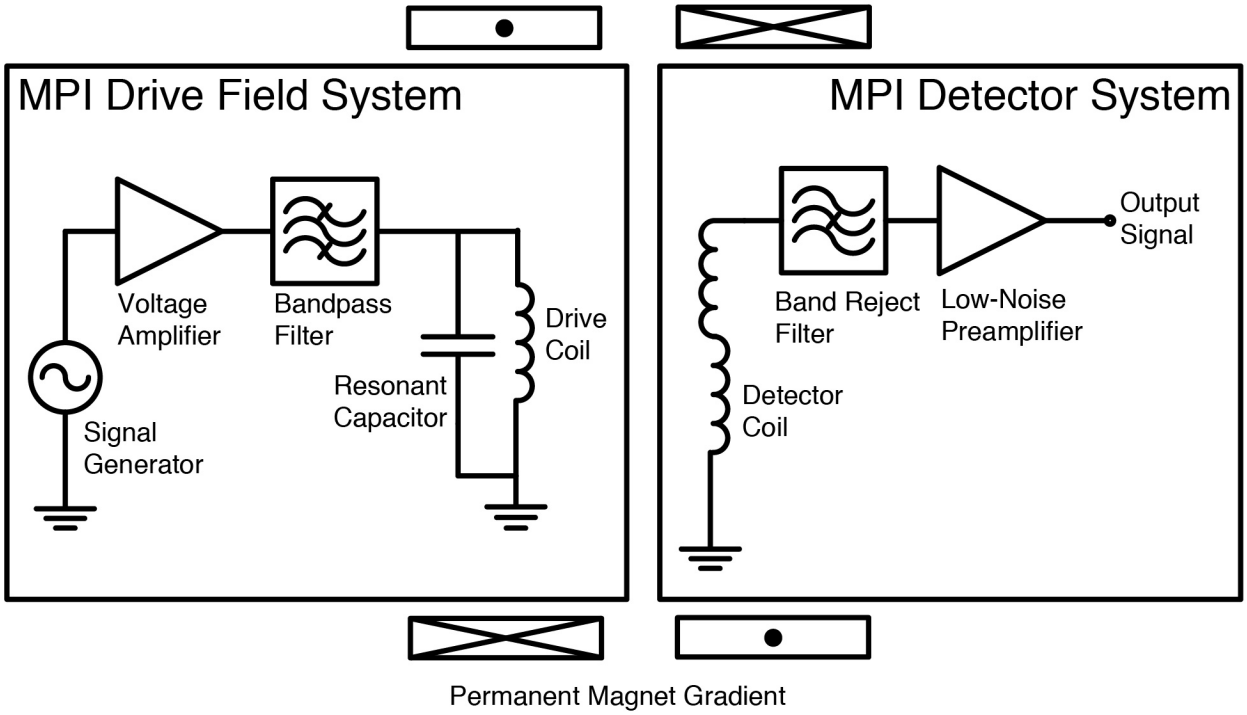

Figure 2.1: Diagram of the architecture of the MPI drive field and signal detection electronic systems. To generate a drive field for particle excitation in MPI, we use a low-distortion sine wave, which is generated digitally and converted to an analog voltage signal, amplified by a power amplifier, filtered for spectral purity, and used to generate a magnetic drive field. As explained in detail in this chapter, the harmonic distortion in the MPI drive field signal must be exceedingly low so as to prevent detectable feedthrough interference in the detector signal. On detector side, a detector coil is wound in a gradiometer configuration to reduce total magnetic coupling to the drive field. The detector signal is then filtered using a band-reject filter to remove direct feedthrough interference from the drive field sinusoid signal before preamplification and digitization.

signal using a band-reject filter before preamplification and digitization.

As the single-tone sinusoidal drive field traverses a location with SPIO particles, the time-varying, nonlinear, SPIO magnetization also changes periodically. However, because SPIO magnetization responds nonlinearly with applied magnetic field, the time-varying SPIO magnetization is a distortion of the input sinusoidal drive field. Hence, the detected particle signal contains a rich signal spectrum at higher harmonics of the fundamental drive field frequency (Figure 2.2). Ideally, we can then simply use the detected SPIO magnetization time signal to reconstruct an MPI image by gridding, or assigning, the detected time-varying voltage signal to the instantaneous location of the FFP, which is user-controlled [2].

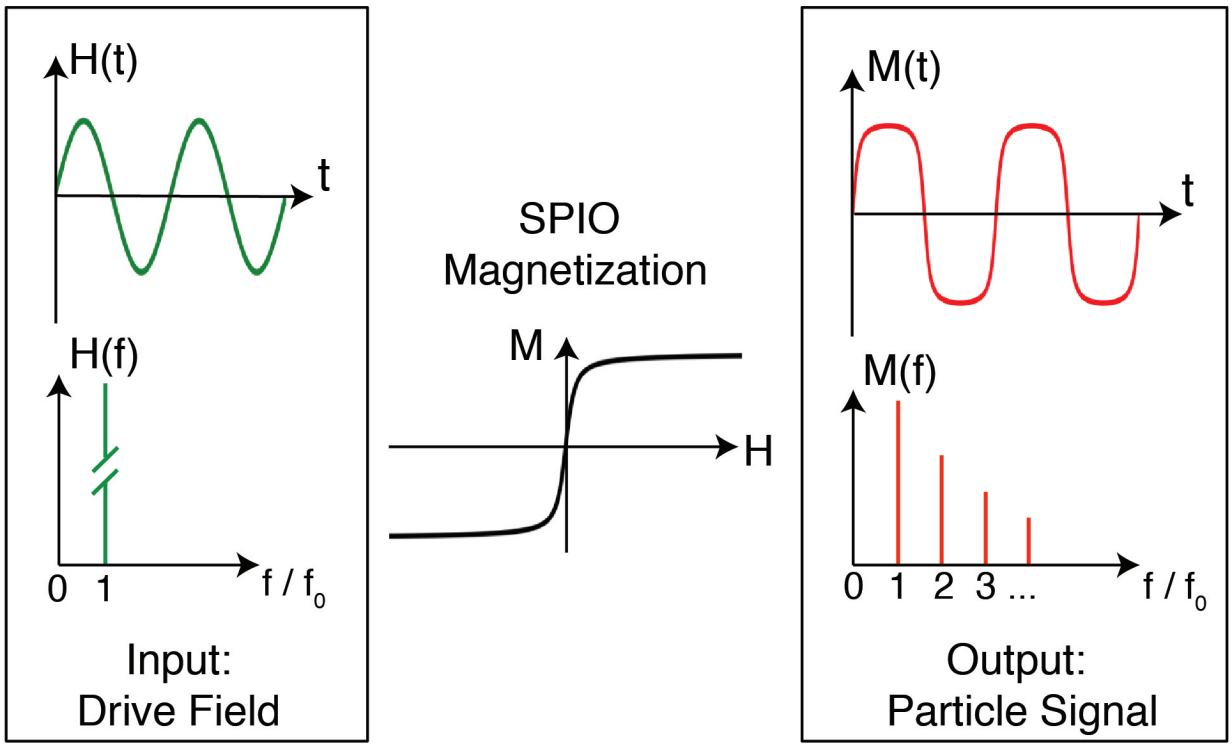

Figure 2.2: Typical MPI drive fields are comprised of a low-distortion time-varying sinusoid. The use of a sine-wave drive field to excite the nonlinear SPIO magnetization causes the SPIO magnetization to be a time-periodic signal that is a nonlinearly distorted version of the input waveform. This particle signal has a characteristic broadband particle signal spectrum at harmonics of the drive field frequency.

One major challenge in MPI is that the SPIO tracer magnetization aligns instantaneously in response to the application of a a time-varying drive field. This instantaneous particle magnetization response can be contrasted with techniques like magnetic resonance imaging, where a radio-frequency magnetic excitation causes nuclear magnetization to precess about a dipole and generate a free-induction decay magnetization signal that can be detected even after the RF excitation field is turned off. Because particle excitation and signal detection in MPI occur simultaneously, the voltage signal detected at the receiver coil comprises of both the desired particle signal as well as undesirable feedthrough interference signal from the sinusoidally time-varying magnetic drive field. Unfortunately, it is not possible to temporally or spectrally decouple the particle signal from the direct feedthrough interference signal, since they are both periodic and necessarily share the same fundamental time period. Moreover, the interfering feedthrough signal at the fundamental frequency from the drive field can be many orders of magnitude larger than the SPIO nanoparticle signal and can saturate the dynamic range of downstream preamplifiers and digitization circuitry. As a result, the

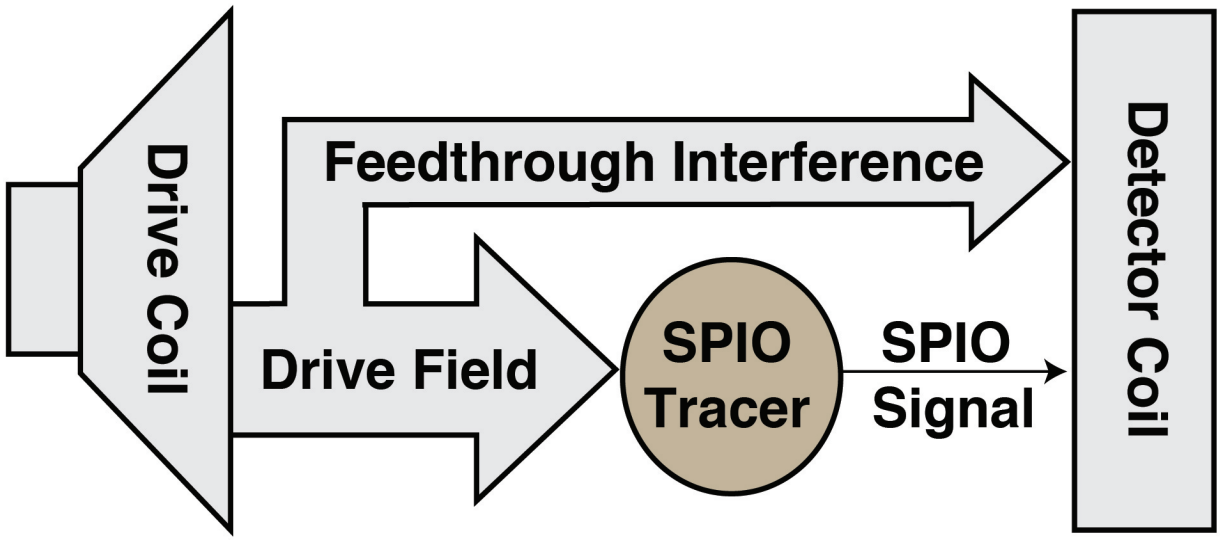

Figure 2.3: Simultaneous particle excitation and signal detection in MPI leads to feedthrough interference from the drive coil to the detector coil.

fundamental frequency component of the detected MPI signal spectrum, containing both the direct feedthrough signal and the fundamental frequency component of the SPIO particle signal, is filtered out of the detector voltage signal using a high-attenuation band-reject filter (Figure 2.1) [46, 1, 2, 39].

Fortunately, we have shown previously that filtering out the direct feedthrough interference at the fundamental drive-field frequency results in a benign and recoverable loss of the DC signal in the reconstructed MPI image. We show that a simple and robust algorithm is sufficient and robust to recover this lost DC signal from the loss of the fundamental frequency component of the particle signal [39].

Unfortunately, in real MPI systems, the drive field is not comprised of a perfectly pure sinusoidal signal. Due to nonlinearities in the system hardware, the feedthrough interference spectrum from the drive field is not only comprised of the fundamental frequency component, but can contain higher harmonic signals that can directly add to SPIO particle signals. It was previously thought that this broadband harmonic interference was only due to nonlinear behavior in the drive field power amplifiers (see Fig. 2.1) [47, 48]. As a result, there have been significant engineering efforts to attenuate high-frequency power amplifier distortion interference by the use of high-power passive electronic filtering [1, 48, 46, 47]. In a previous work [47], we demonstrated the use of a 7^{th}-order Butterworth lowpass filter downstream of the drive field power amplifiers to remove high-frequency harmonics of the fundamental frequency. This filter was able to achieve 125 dB of signal suppression at the third harmonic, which was close to a simulated suppression value at 140 dB (Fig. 2.6).

Despite the high-attenuation filters, however, our MPI experiments showed persisting

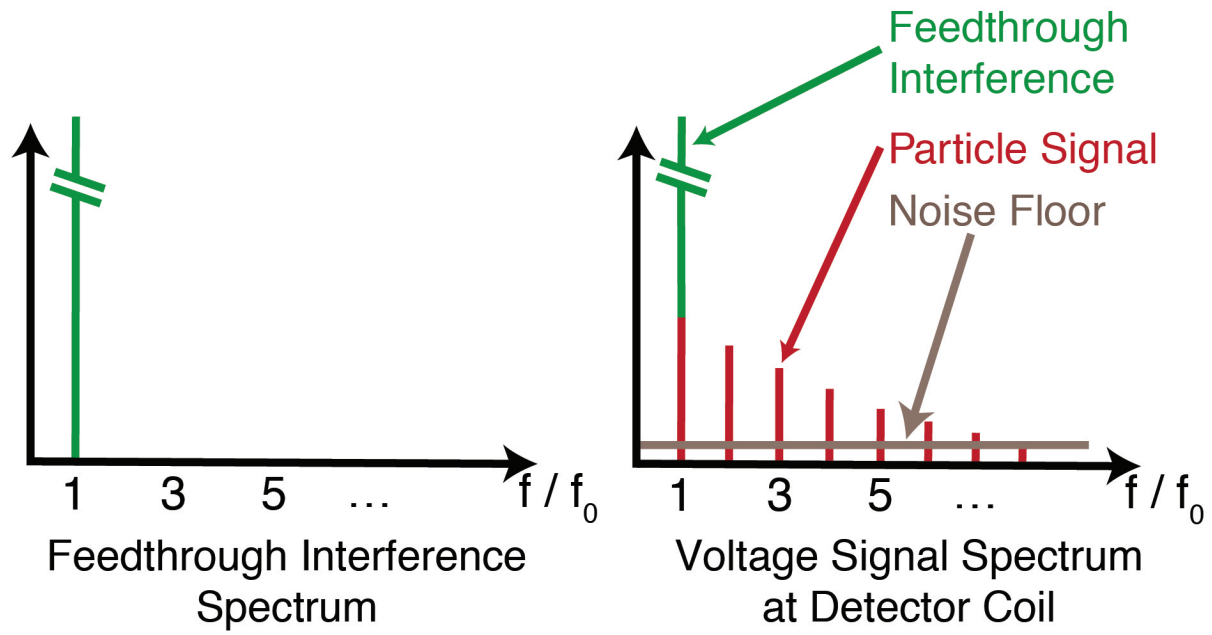

Figure 2.4: Ideally, feedthrough interference signal is only at the fundamental frequency. Although the simultaneous nature of MPI excitation and signal detection causes the detected voltage signal to contain both the SPIO magnetization signal and direct feedthrough interference, which can be orders of magnitude higher than the particle signal amplitude, removal of the direct feedthrough interference at the fundamental frequency of the drive field results in a benign and recoverable image artifact. We have previously shown that the loss of the fundamental frequency of the particle signal corresponds to the loss of a DC offset in the reconstructed image, which can be recovered via a simple algorithm [39].

broadband harmonic distortion interference in the detector signal spectrum. Therefore, we conclude that additional harmonic interference sources must exist in the MPI drive field or detector systems after the power amplifier stage. As MPI is a nascent field, these interfering mechanisms, and methods to suppress this harmonic interference, have not yet been fully explored.

This broadband interference can severely limit the signal-to-interference ratio and detection sensitivity of the MPI system, particularly when imaging small quantities of SPIO tracer. As an example, our existing MPI scanners have shown feedthrough interference at the second and third harmonics of the fundamental frequency that are at least 40-fold (32 dB) above the system noise floor. Reducing this coupled interference is extremely important for the clinical translation of MPI. For example, a 40-fold improvement in detection sensitivity would enable smaller SPIO injection doses to the patient, visualize smaller blood vessels in angiography, track fewer numbers of cell implants *in vivo*, or improve image acquisition

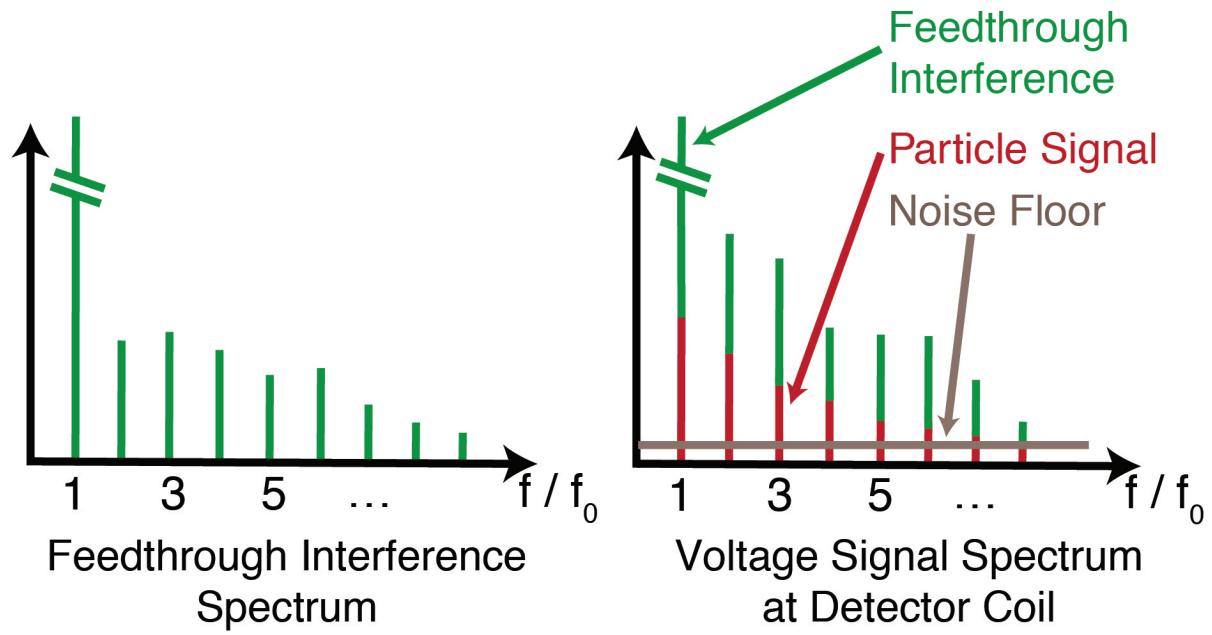

Figure 2.5: Real MPI systems contain broadband harmonic interference in the drive field. This broadband interference from the drive field, which can arise from nonlinearities in the drive field hardware, has the same frequency components as the particle magnetization signal. Unlike the fundamental frequency interference, these broadband interfering signals cannot be recovered robustly and can severely limit the SNR of the MPI detector.

speed dramatically. Removal of this distortion interference would enable visualization of smaller blood vessels and more accurate diagnosis while potentially negating the need for catheterized arterial injections.

In this chapter, we show the design and construction of a non-imaging modular MPI testbed to investigate sources of harmonic distortion interference in the MPI drive field and engineer methods to suppress harmonic interference sources. We demonstrate the use of this modular MPI scanner testbed to study harmonic interference in the resonant capacitor in the drive field chain, the band reject filter in the MPI detector system, and the effects of a nearby permanent magnet used to create the static gradient used in MPI. Finally, we show the use of an actively controlled harmonic distortion cancellation technique that enables the suppression of broadband feedthrough interference to below the system noise floor.

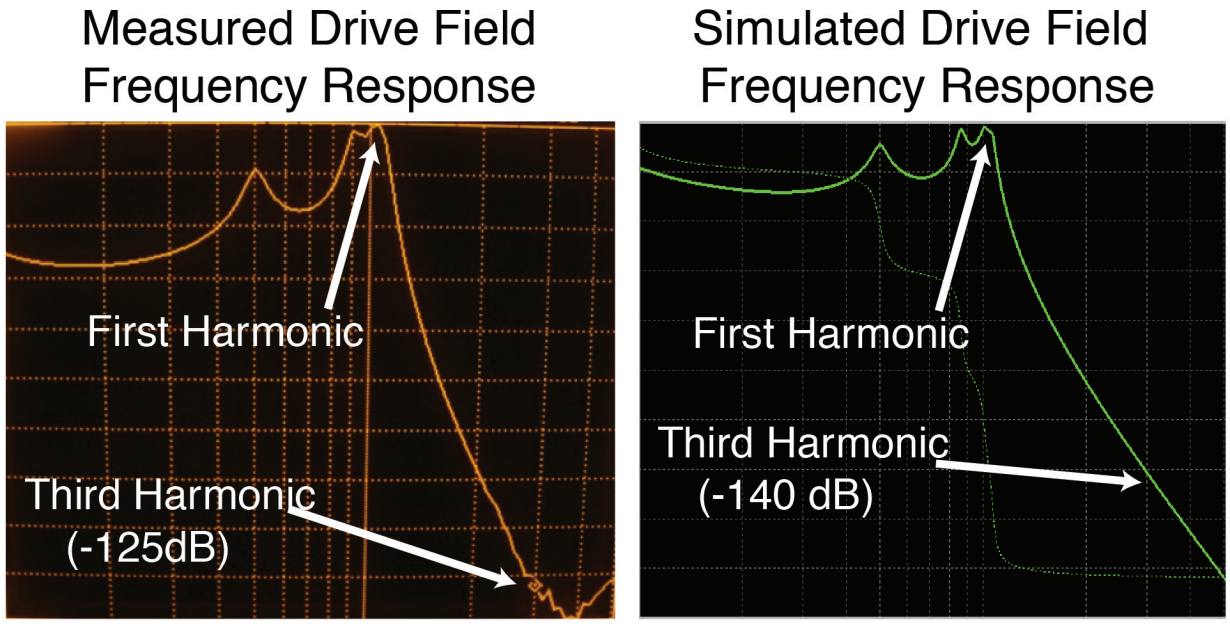

Figure 2.6: A 7$^{\text{th}}$-order Butterworth low-pass filter can suppress harmonic interference from the drive field power amplifier by as much as 125 dB at the third harmonic. Though not explored in detail in this dissertation, the design and construction of these drive-field filters require careful impedance matching to the power amplifier and resonant drive coil load as well as design for high currents used for the drive field.

2.2 Initial Investigation of Harmonic Interference Sources in MPI System Hardware

2.2.1 A Modular MPI Testbed for Investigating and Mitigating Feedthrough Interference

In order to systematically diagnose interference in MPI systems, I constructed a non-imaging testbed that has all the components of a standard MPI scanner design except a set of slow-shift electromagnets (Fig. 2.7 and 2.8). The design of this testbed includes a 7 T/m magnetic field gradient, created using a pair of NdFeB permanent magnets (at 5 inches diameter and 0.75 inches thick) and fixed in place in a aluminum and Delrin plastic enclosure. The size of the assembly is 10.5 inches wide by 7.5 inches tall by 7 inches deep with a bore at 4 inches diameter. To generate the drive field used in MPI, I designed an MPI drive coil constructed using 8 AWG round magnet wire on a custom 3D-printed coil former. The drive coil has total inductance of 16.9 µH and is connected in parallel with 3 parallel-connected polypropylene film capacitors (CDE940C, Cornell Dubilier, Liberty, SC) with total capacitance of 10 µF,

for a resonant frequency at 12.24 kHz. The resonant drive coil system can generate drive fields in excess of 30 mTpp at the resonant frequency. I also constructed a receive coil using 15 AWG round magnet wire in a gradiometer configuration and a total inductance of 35 µH. The system had a 3.5 inch diameter free bore. To isolate magnetic field coupling between the drive field system and the magnetic gradient permanent magnets, we placed a 9 inch long, 4 inch outer diameter, 0.1 inch thick copper tube shield between the drive coil and the permanent magnet. The drive field system for the MPI testbed was connected using modular nonmagnetic system connections.

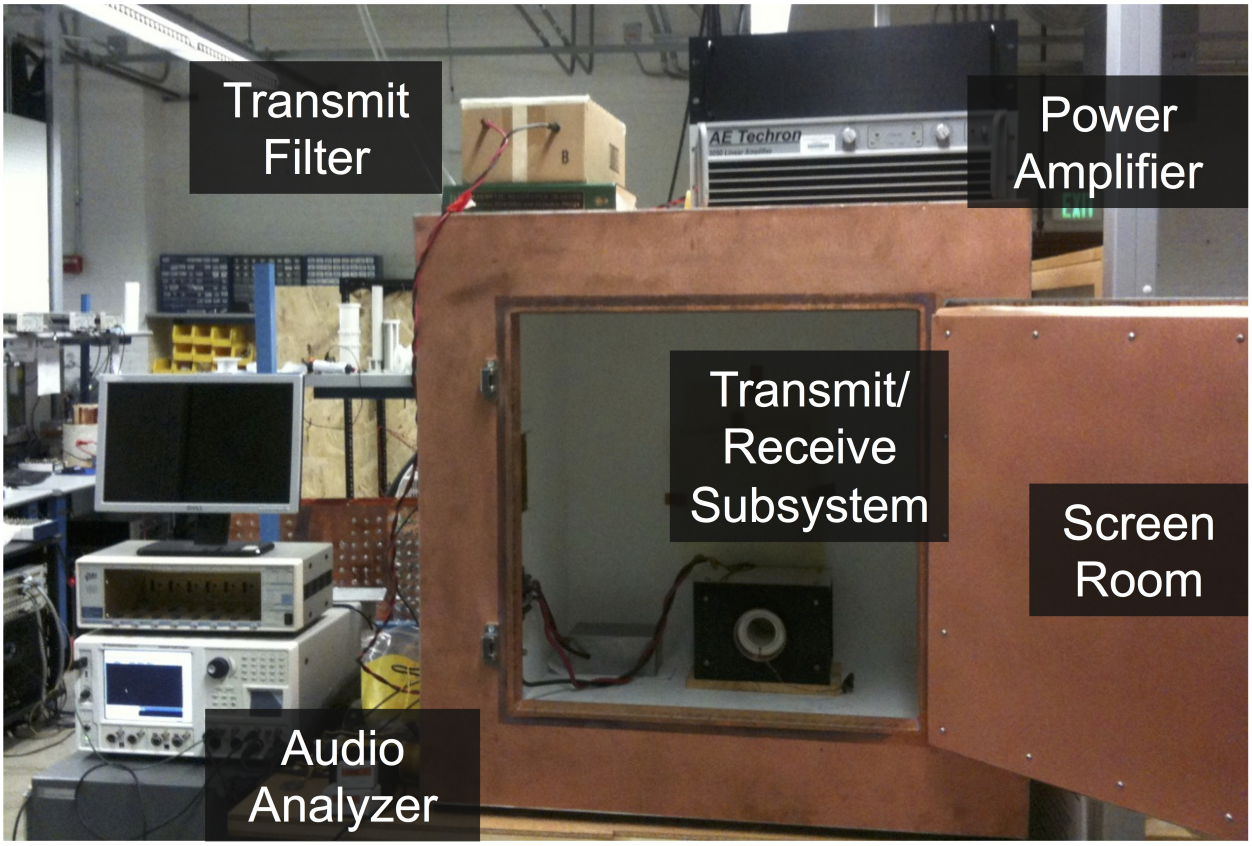

Figure 2.7: Modular testbed for diagnosing harmonic interference sources in MPI scanner systems. The system contains all necessary components for assembling an operational MPI scanner except slow-shifting electromagnets. To generate a drive field, a voltage signal is generated using a low-distortion audio analyzer or DAQ card, amplified using a power amplifier, conditioned using a passive high-power bandpass filter, and generated as a magnetic field in a resonant drive coil. The drive field and detector subsystems are shielded from environmental electrical noise using a copper screen room.

The modular testbed scanner was placed in a RF shielded copper chamber (ETS-Lindgren, St. Louis, MO) for suppression of environmental noise. To generate a drive field, a low-

distortion sinusoidal signal at $f_0 = 12.125$ kHz is generated using an audio analyzer (SR1, Stanford Research Systems, Sunnyvale, CA) or in Matlab (Mathworks, Natick, MA), output using a NI-6259 (National Instruments, Austin, TX) analog output channel, and amplified with one channel of a Crown CE2000A or LVC5050 power amplifier (AE Techron, Elkhart, IN). The high-power drive field signal is then filtered at f_0 using a 2-stage resonant LC bandpass filter to remove harmonic distortion interference from the power amplifiers and transmitted in a resonant coil to create a time-varying magnetic field.

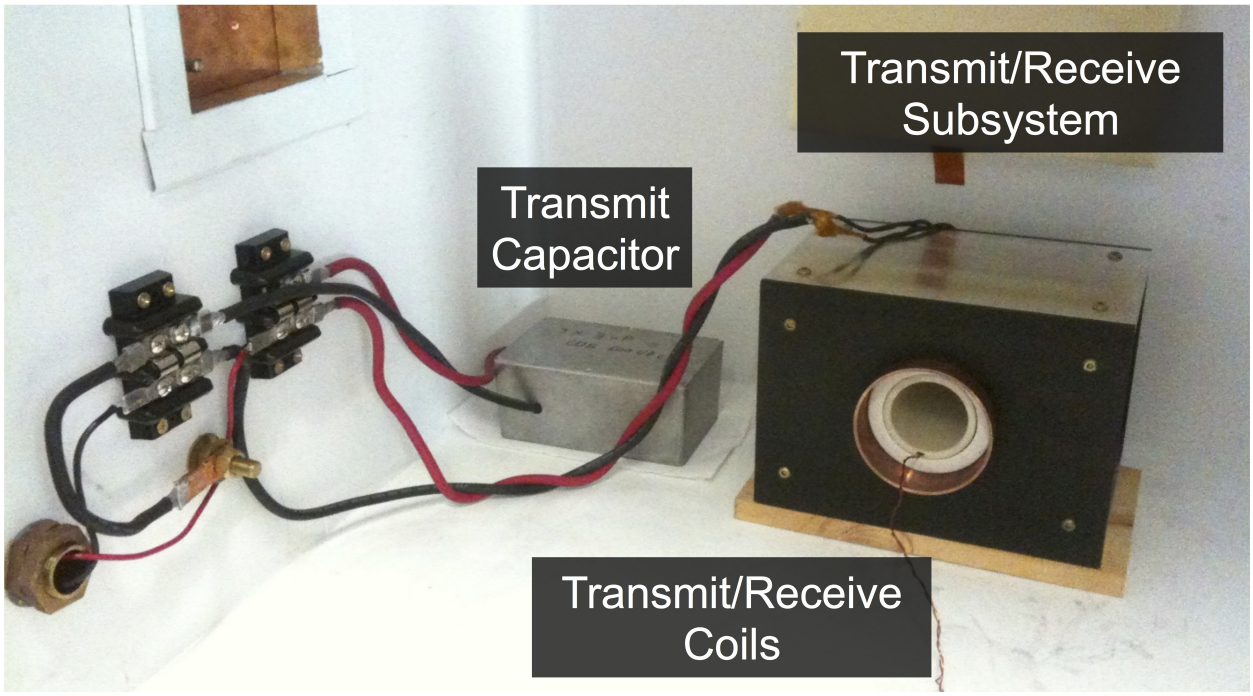

Figure 2.8: Drive field generation detector system for modular MPI feedthrough interference testbed. An MPI drive coil is constructed using 8 AWG round magnet wire on a custom 3D-printed coil former. The drive coil is connected with a capacitor in parallel for a resonant frequency at 12.24 kHz and drive field amplitude greater than 30 mTpp. The constructed MPI detector coil uses 15 AWG round magnet wire in a gradiometer configuration. This transmit/receive system has 3.5 inch diameter free bore and uses a copper tube as a magnetic shield between the drive coil and the permanent magnet. Modular nonmagnetic connectors are used for high-power system components.

Feedthrough and particle signals received using the detector coil are notch filtered at f_0, preamplified using a commercial preamplifier (SR560, Stanford Research Systems, Sunnyvale, CA), and digitized using a NI-6259 DAQ card. The detected feedthrough and particle signals are also analyzed using a commercial audio analyzer for spectral and noise analysis (SR1, Stanford Research Systems).

2.2.2 Investigating Nonlinear Distortion in the MPI Detector Notch Filter

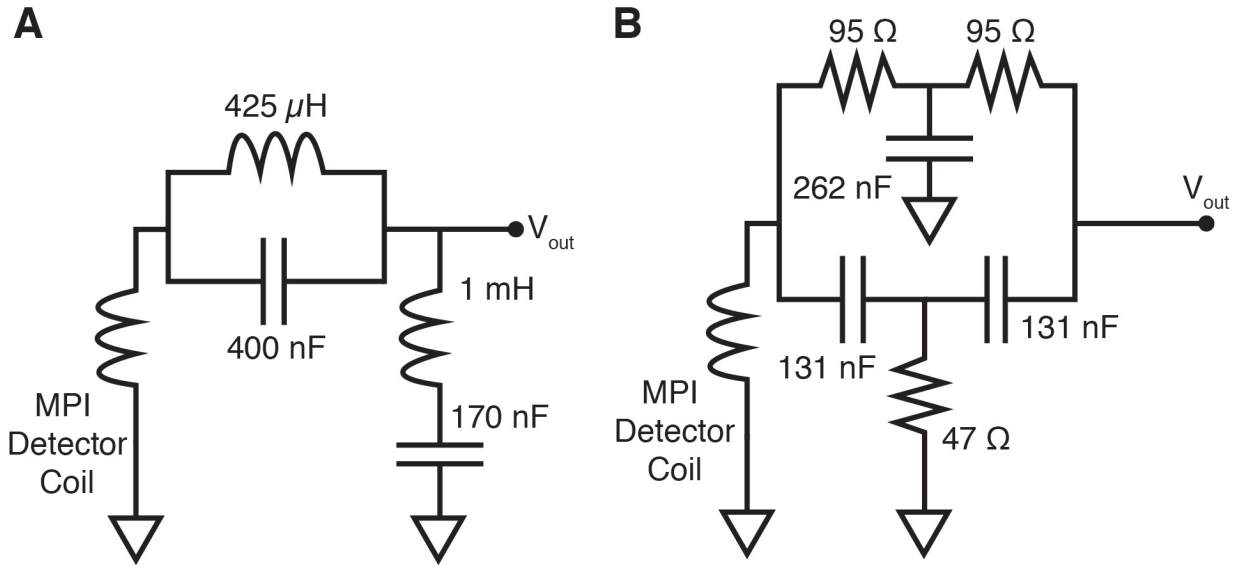

Figure 2.9: MPI detector system notch filters tested for systemic harmonic distortion interference. (A) Doubly resonant LC notch filter used to attenuate the fundamental frequency of the drive field that feeds through to the detected voltage signal. This notch filter can achieve 45 dB of attenuation at the fundamental frequency, but may introduce additional harmonic interference due to its use of a high-permeability ferrite core in its inductor construction. (B) Alternate Twin-T notch filter design used as a comparison. This filter topology does not use inductors or high-permeability materials.

Band reject filters are necessary in MPI to suppress the direct feedthrough signal at f_0, which can be over one million-fold larger than particle magnetization signals, to prevent saturating downstream amplification stages. Existing filter topologies typically use passive LC resonant circuits for notch filtering. Because the inductors in these filters typically use high-permeability ferrite material, they may contribute to the system's distortion interference from the nonlinear magnetic response of these materials. Using the constructed MPI testbed, we first investigated the possibility that the notch filters in the MPI detector could actually contribute distortion interference in the receive spectrum. To test this, we replaced the LC passive notch filter with an inductorless twin-T notch filter which is entirely designed using resistors and capacitors. Both filters are designed to suppress the feedthrough signal at the fundamental frequency by 40 dB. A diagram of the two detector notch filter designs is shown in Figure 2.9.

After constructing the filters, I measured the frequency responses of the two receive notch filter topologies (Fig. 2.10). Both filter types achieve 40dB suppression of the fundamental

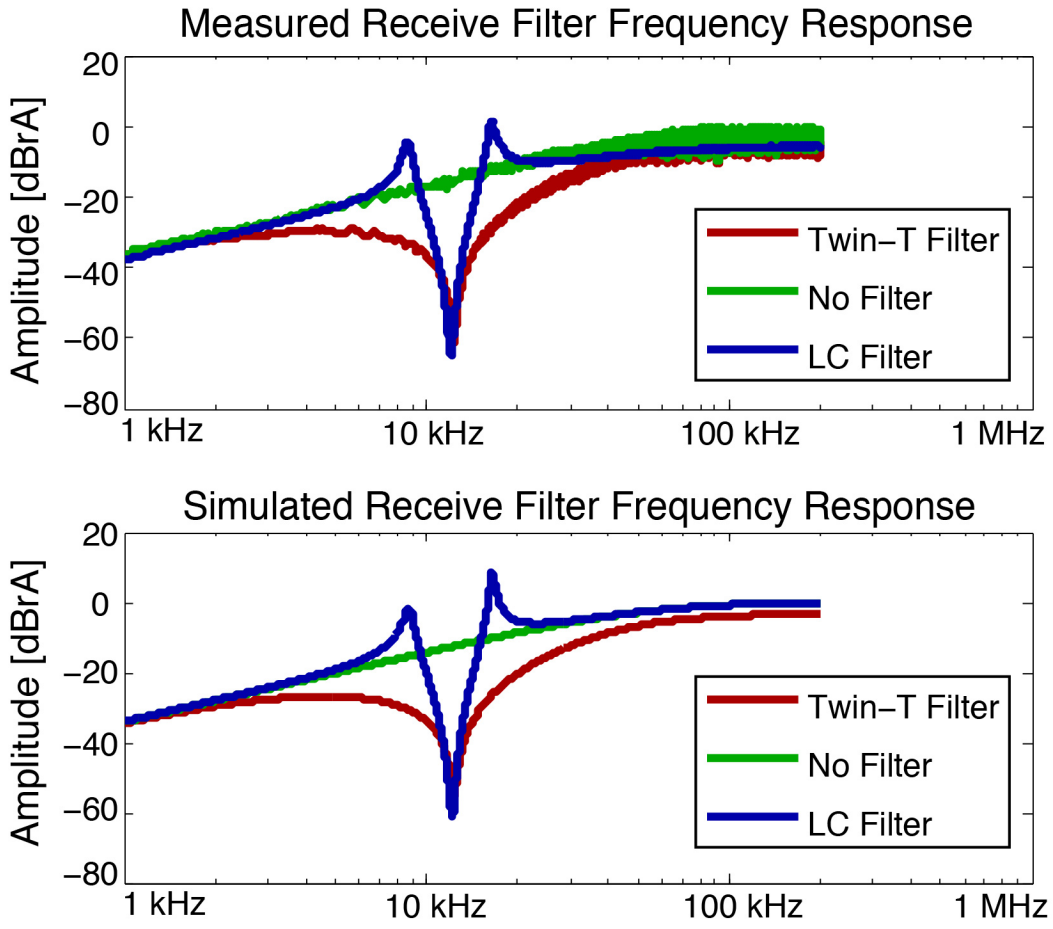

Figure 2.10: Measured and designed transfer functions of the filters compared to no detector system filter. Both filters achieve 40dB suppression of the direct feedthrough signal at the fundamental frequency and match well with simulation.

feedthrough signal and match well with simulation.

I then measured the feedthrough interference spectra for the two filters, as well as the testbed system without the use of a notch filter, and compared the spectra for distortion interference levels at harmonic frequencies of f_0. A measurement (Fig. 2.11) of the feedthrough spectrum shows that inductor elements in the LC notch filters do not contribute significantly to the distortion interference of the MPI system compared to inductorless Twin-T filters or the testbed system with no receive filters.

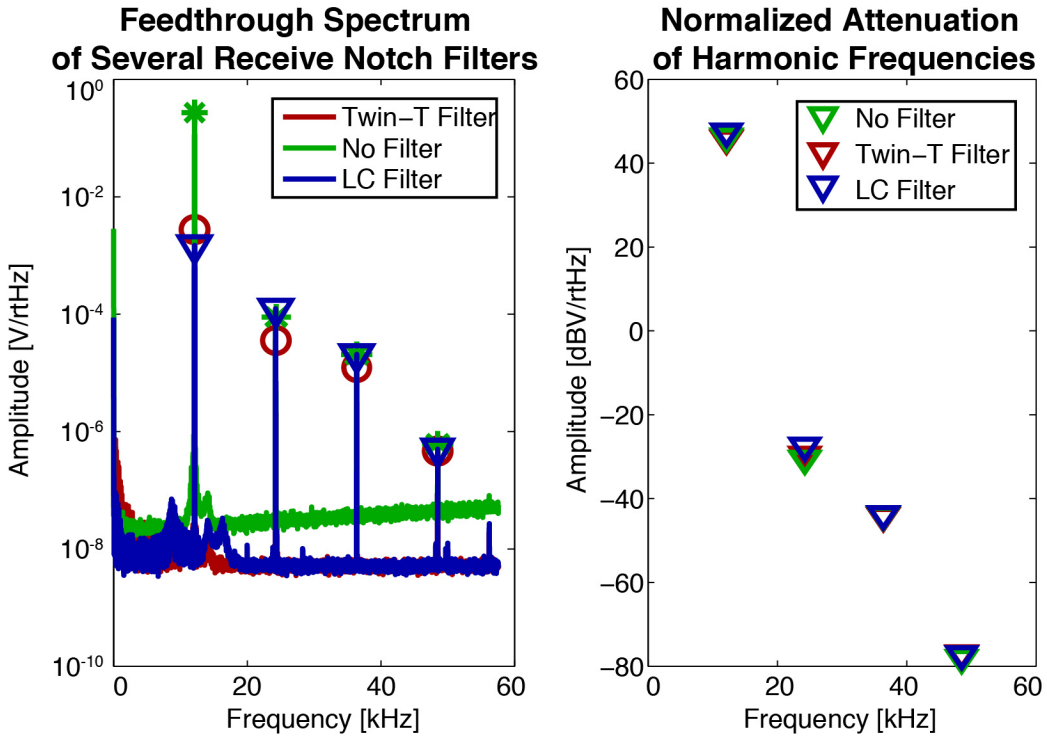

Figure 2.11: MPI detector system LC notch filters do not contribute harmonic distortion interference in the detector voltage signal. The harmonic interference from the 2^{nd}-4^{th} harmonic frequencies showed < 1 dB difference when a LC notch filter, an inductor-less Twin-T filter, or no filter was applied in the MPI detector system.

2.2.3 Capacitor Distortion in Magnetic Particle Imaging

I also investigated the contribution of the resonant drive coil capacitor as a potential distortion interference mechanism in MPI. Because these capacitors are resonant with the drive coil, they have the same the high currents used to generate the drive field as the drive coil, which can be on the order of 100 A. Several models for nonlinear capacitor distortion have been proposed in audio literature, including dielectric memory [49] and nonlinear capacitance changes due to applied voltage [50]. Hence it is possible that even highly linear capacitors such as the polypropylene capacitors typically used in MPI scanners can distort at high power. Moreover, the amount of total distortion in the capacitors does not need to be substantial: even nonlinear changes in the ppm range may be detected as interference in the MPI detected signal spectrum. Here, we measure system interference using resonant capacitors with four operating voltage ratings to investigate the contribution of capacitor distortion in MPI.

Four high-power polypropylene film capacitors (Fig. 2.12) were tested as resonant drive field capacitors in the custom MPI testbed with AC operating voltage ratings of 75 V_{rms}

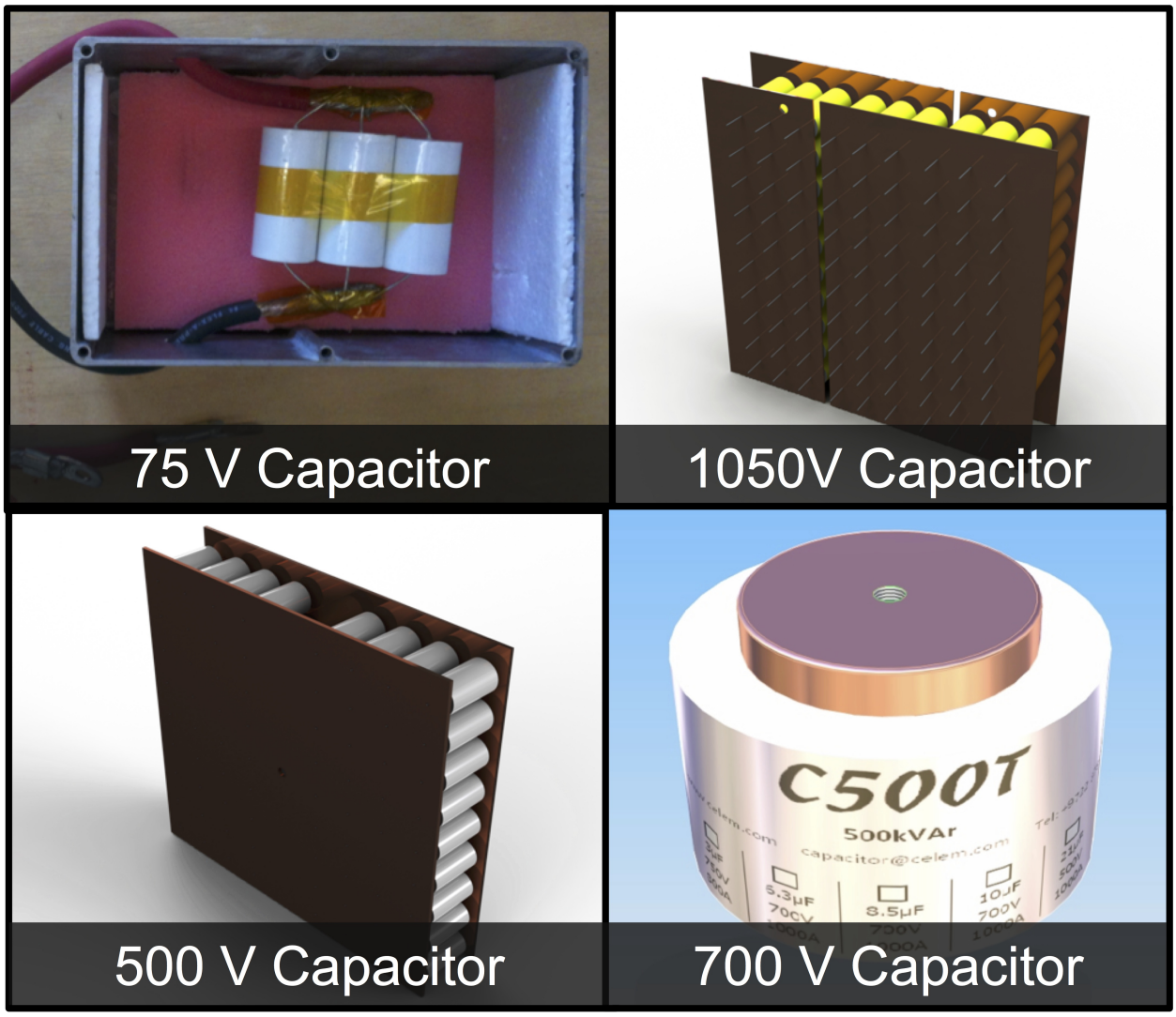

Figure 2.12: Capacitors tested for contributions to feedthrough interference, all with identical capacitance. The 500 V and 1050 V-rated capacitors were custom assembled for voltage/current derating.

(CDE940C, Cornell Dubilier, Liberty, SC), 500 V_{rms} (CDE942C, Cornell Dubilier), 700 V_{rms} (Celem, Jerusalem, Israel), and 1050 V_{rms} (105FPA, Illinois Capacitor, Chicago, IL). Feedthrough interference spectra from DC to the 4^{th} harmonic were obtained on the SR1 Audio Analyzer with a fixed resonant drive coil and capacitor voltage at 200 V_{rms}.

The total feedthrough harmonic interference in the system for various resonant capacitors is plotted in Figure 2.13. The fundamental feedthrough signal at f_0 remains constant for all capacitors tested. This suggests that the same AC drive field was generated in all cases as expected. However, our data shows that distortion interference drops significantly with

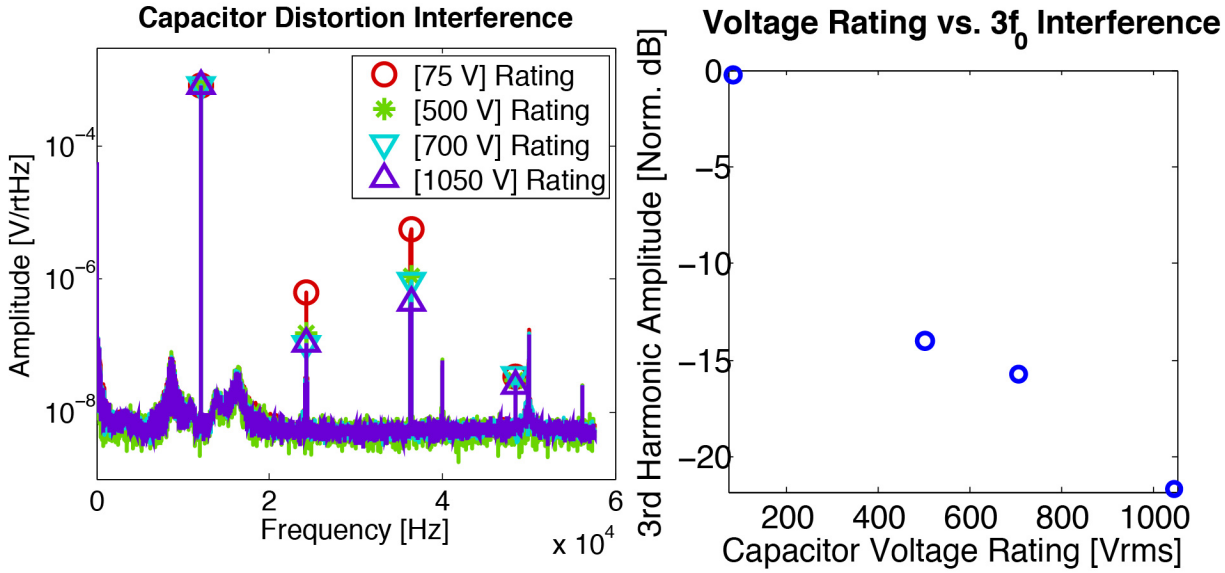

Figure 2.13: Drive field system resonant capacitors may introduce undesired harmonic feedthrough interference into the MPI detector chain. (Left) Feedthrough distortion interference spectra for the four capacitors under test from DC to 52 kHz, with f_0 at 12 kHz. Noise spikes at 40, 50, and 58 kHz are from the audio analyzer power supply and environmental interference. The total harmonic interference decreases monotonically with capacitor voltage rating. (Right) Feedthrough distortion interference amplitude (plotted in normalized dB) at $3f_0$ for various capacitor ratings.

increasing capacitor voltage rating. The 1050 V_{rms}-rated capacitors generated 15-fold less interference at $3f_0$ than 75 V_{rms}-rated capacitors. Fig. 2.13 shows that interference at $3f_0$ in dB decreases linearly ($R^2 = 0.95$) for varying capacitor voltage ratings. This preliminary data suggests voltage saturation or voltage-controlled capacitance changes could be a mechanism for capacitor distortion-induced harmonic interference in MPI.

Here we demonstrated experimentally that transmit capacitor distortion can be dramatically reduced by simply using over-rated capacitors. This is an important finding as it may translate to more than a 20 dB improvement in SNR and detection sensitivity in MPI. Our data is consistent with a nonlinear capacitor model where the capacitance value changes instantaneously with applied voltage [50].

2.2.4 Magnetic Distortion Feedthrough from Permanent Gradient Magnets in MPI

The third mechanism I investigated as a potential harmonic interference generator in MPI was the interaction between the AC MPI drive field and the DC magnetic field gradient

created using permanent magnets. Typical MPI static field gradients can be constructed using electromagnets or NdFeB permanent magnets. The use of NdFeB permanent magnets allows for high gradient amplitudes for small animal imaging and zero power dissipation. However, permanent gradient magnets potentially can contribute distortion interference in the system through 1) generating a force from interacting with current in the transmit coil, or 2) changing in magnetization in response to the applied excitation field. To test distortion interference levels due to gradient magnets, I measured the system feedthrough spectrum in the presence and absence of the permanent gradient magnets in the testbed MPI system.

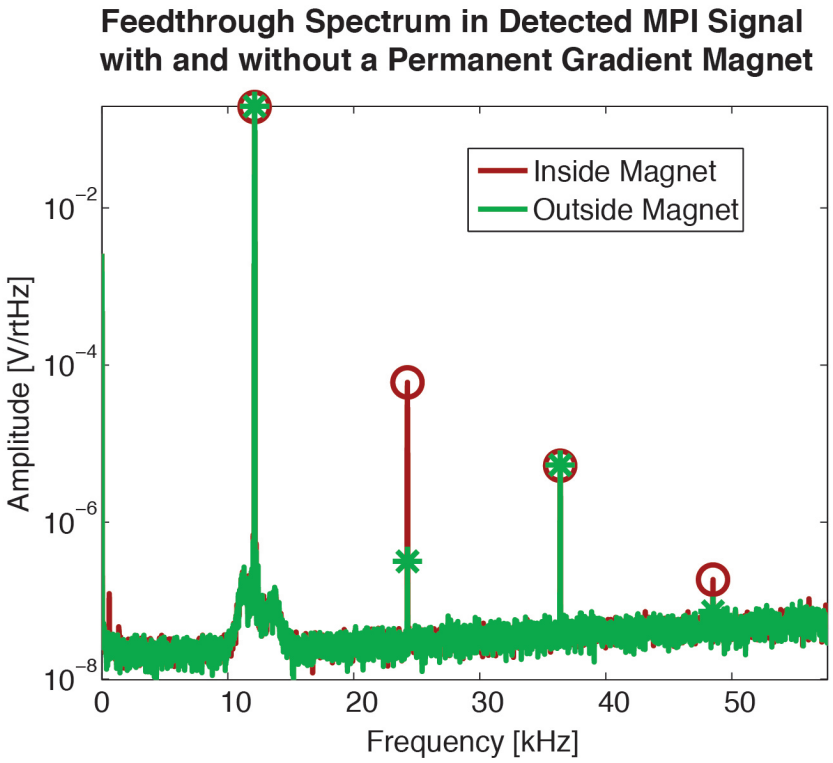

Figure 2.14: Permanent magnets used to generate the static MPI gradient field contributes to harmonic interference in MPI scanners. An acquired MPI feedthrough interference spectrum shows that the presence of permanent magnets in the MPI scanner can introduce substantial harmonic interference. Feedthrough interference at the 2^{nd} harmonic is 40 dB (100-fold) increased in the presence of a permanent gradient magnet.

The presence of the permanent gradient magnets contributes around 100x (40dB) more distortion interference at $2f_0$ compared to system feedthrough in the absence of the magnets (Fig. 2.14). A solution to this distortion interference source is highly promising to improving sensitivity in MPI. To determine if the distortion mechanism is due to the magnetization of the permanent magnets or the force between the magnets and the transmit coil, I also mechanically stiffened the transmit/receive coils in epoxy with the hypothesis that mechanical

forces on the transmit coil would be substantially dampened after the system is epoxied. However, this did not change the amount of feedthrough harmonic interference from the permanent magnets, suggesting that the harmonic interference mechanism is due to the drive field interacting with the nonlinear magnetization of the gradient magnets themselves. Hence, to resolve this interaction, we may potentially use a thicker conducting magnetic shield [51] or use electromagnetic gradients instead of permanent magnets.

2.3 Actively-controlled Cancellation of Harmonic Feedthrough Interference in MPI

In the previous section, we show that harmonic feedthrough interference in MPI can arise from multiple sources after the drive field power amplifiers and bandpass filters. To resolve each one of these harmonic distortion mechanisms, one potential solution is to engineer each interfering component to more stringent specifications. For example, it may be possible to further derate the resonant drive coil capacitors by another factor of two to four. However, such engineering approaches may incur diminishing returns as component costs become prohibitive at these specifications.

A potential alternative solution is to actively suppress drive field nonlinearities instead of only passively engineering system hardware components. An example of such an approach is the advent of "noise-cancellation" in the audio industry. Whereas techniques to improve passive noise cancellation focused on improving materials for impeding sound transmission, active approaches remove interfering sounds by sending out a sound wave with equal amplitude but opposite phase, such that the interfering sound is suppressed via destructive interference.

Feedthrough harmonic interference in MPI may well be suppressed using a similar active approach, whereby we suppress the introduced harmonics via a magnetic field equal in amplitude but opposite in phase to the interfering fields introduced by the system components at each interfering harmonic frequency. We note that this can be done using an automated control system, such that any time-varying drifts in harmonic interference signal patterns can be automatically compensated by the active cancellation circuit without the use of human calibration.

2.3.1 Active Cancellation Circuit Design and Implementation

As MPI distortion interference arises from various system sources, many of which remain uncharacterized, it becomes desirable to remove the interfering signals from the total received MPI signal actively by injecting a cancellation signal such that the net interfering magnetic fields at high frequencies are minimized. This approach is not unfamiliar to members of the magnetic resonance imaging community; an analogy can be made to the active shimming circuits used to boost the homogeneity of the main B_0 field in MRI.

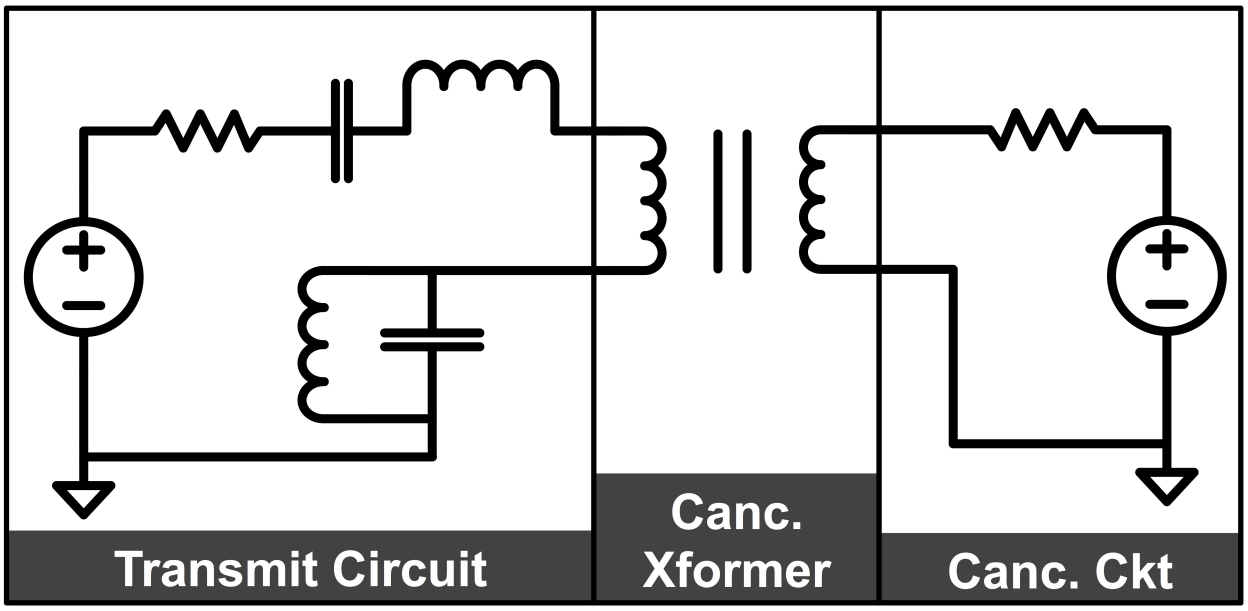

Figure 2.15: Implementation of active interference cancellation in MPI via transformer-coupling to the main drive field system. Left: Transmit signal source, filter, and resonant transmit coil. Middle: Cancellation transformer. Right: Cancellation signal source and protection resistor. Note: signal generators and amplifiers are lumped as voltage sources in this diagram.

The active cancellation signal can potentially be inserted into one of several nodes in the main drive field circuit (Fig. 2.1). One such insertion node is at the signal generator, where cancellation signals can be digitally added to the main transmit signal prior to digital-analog conversion and subsequent amplification. The main drawback to this method is that the bandpass filter in the transmit chain will substantially attenuate signals at frequencies other than f_0, making broadband active cancellation difficult for suppressing harmonic interference generated downstream of the drive field filters, such as that arising from the resonant drive field capacitors.

Alternatively, the active cancellation signal can be injected after the bandpass filter to avoid filtering higher-frequency cancellation signals. One potential actuation technique to realize this design is to transformer-couple a power signal into the main drive field circuit after the bandpass filter but before the drive coil. Such a design is illustrated in Fig. 2.15, where the cancellation signal is generated and amplified by separate hardware from the main transmit chain. A practical realization of this design should not substantially change the filtering or impedance matching of the main transmit chain, while allowing signal currents from the cancellation circuit to effectively generate interference-canceling magnetic fields.

To realize the cancellation circuit design, a solenoidal air-core transformer was custom-built on an 2.5 inch (OD) acrylic form using 10 AWG multi-strand wire (Fig. 2.16). While

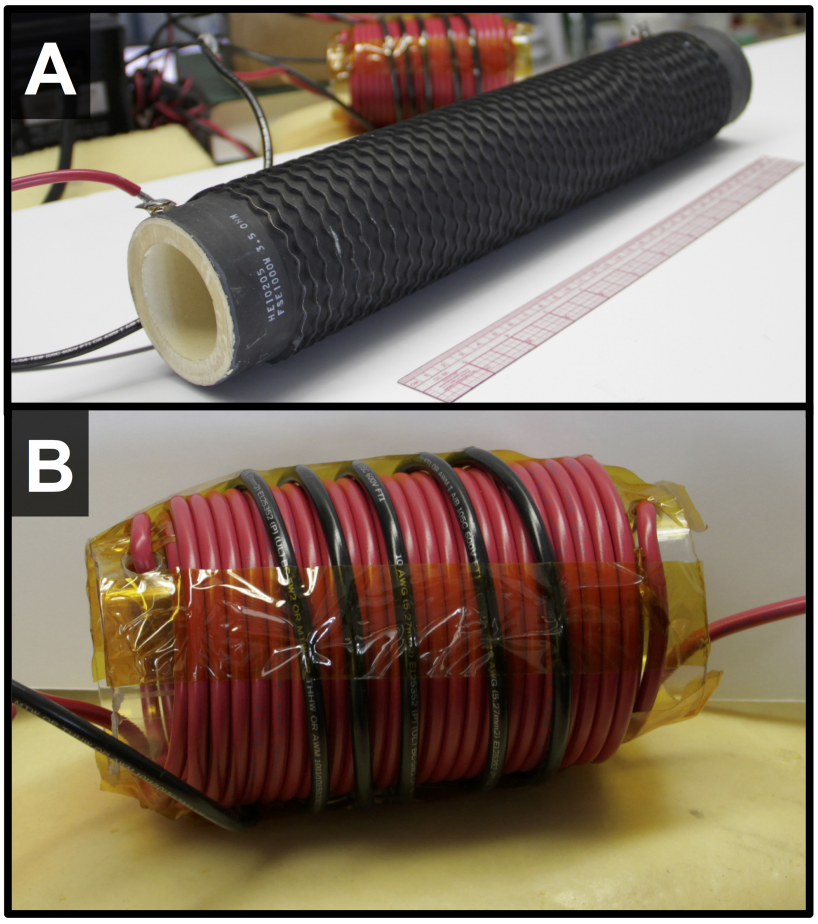

Figure 2.16: MPI active cancellation actuator circuit implementation. (A) High-power protection resistor serially connected to cancellation-side transformer to prevent short-circuiting DC currents in the cancellation amplifier. (B) Cancellation coupling transformer; red wire: cancellation (primary) side, black wire: main transmit (secondary) side.

other core materials with higher permeability may be considered due to their ability to store higher B-fields and coupling in the transformer, they are sensitive to other local magnetic field sources and can saturate, which can contribute to the total distortion interference in the system. In future iterations, the use of litz wire in the cancellation transformer design would decrease power loss in the copper conductors by 13-fold at 10 kHz.

To more effectively generate interference-canceling magnetic fields, cancellation signal currents in the cancellation winding (which we will refer to as the primary winding of the transformer) were amplified after coupling to the main drive field circuit (the secondary). In this transformer, the primary-to-secondary turns ratio is 50:5. Because $\frac{N_1}{N_2} = \frac{I_2}{I_1}$, where N_1 and N_2 are respectively the number of turns, and I_1 and I_2 are respectively the currents, in the primary and secondary, the transformer has a 10-fold current gain on the secondary winding.

The self-inductance of the primary and secondary windings are respectively 67 µH and 2 µH, which did not significantly change the filtering or impedance matching characteristics of the main drive field system.

To enable cancellation of the harmonic interference, a series of cancellation signals at harmonics of the fundamental drive field frequency were generated using Matlab, output using a NI-6259 analog output channel, amplified with one channel of a Crown CE2000A power amplifier, and transformer-coupled into the main transmit circuit immediately prior to the transmit coil. A 3.5 Ω, 1000 W high-power resistor (FSE1000-3.5, Huntington Electric, IN) was inserted serially with the transformer in the cancellation circuit to prevent a short circuit at DC between the amplifier output and ground, as well as to dissipate power coupled from the main transmit signal chain.

2.3.2 Active Cancellation Controller Design and Implementation

Here we describe the design and implementation of an automated control system for the active harmonic interference cancellation circuit for MPI systems (Figure 2.17). We first describe the active cancellation controller as a classic control loop, where the objective is to minimize the feedthrough interference at each interfering harmonic frequency. Therefore the feedthrough interference at each interfering frequency is detected via a dedicated sniffer coil. This feedback signal is subtracted from a desired control signal (which seeks to attenuate each interfering harmonic signal down to 0), and the error signal is input into a controller and into the cancellation system.

For the specific application of canceling narrowband interference at specific harmonic frequencies, we converged on the use of a classic single-input, single-output control loop design, but using Cartesian feedback and control of each interfering harmonic. Cartesian feedback schemes have been previously used for linearizing RF power amplifiers in similar applications [52, 53]. Briefly, in the Cartesian feedback design, a narrowband signal at a specific frequency is detected using a custom sniffer coil, preamplified (SR560), digitized (NI-6259, National Instruments), and demodulated into its in-phase and quadrature components in Matlab, and each component is controlled using its own control law. We perform this in software by multiplying the interfering harmonic signal with in-phase and quadrature carriers, followed by a simple low-pass filtering operation. The demodulated in-phase and quadrature signals are then subtracted from control signals, which are all 0 as the goal is to attenuate all harmonic interference, to generate error signals. These error signals are then input into a simple software PI controller, with manually tuned controller gains, before being upmodulated and summed. The control signals for all interfering harmonics are subsequently summed together and output as a analog voltage signal to be amplified by a power amplifier and transformer-coupled into the main drive field.

One major design consideration for Cartesian feedback controllers is proper knowledge of system phase accrual at each frequency to be controlled. Because each frequency is decomposed into its in-phase and quadrature components before control, it is important to demodulate the signal using the correct phase such that the control laws for the in-phase

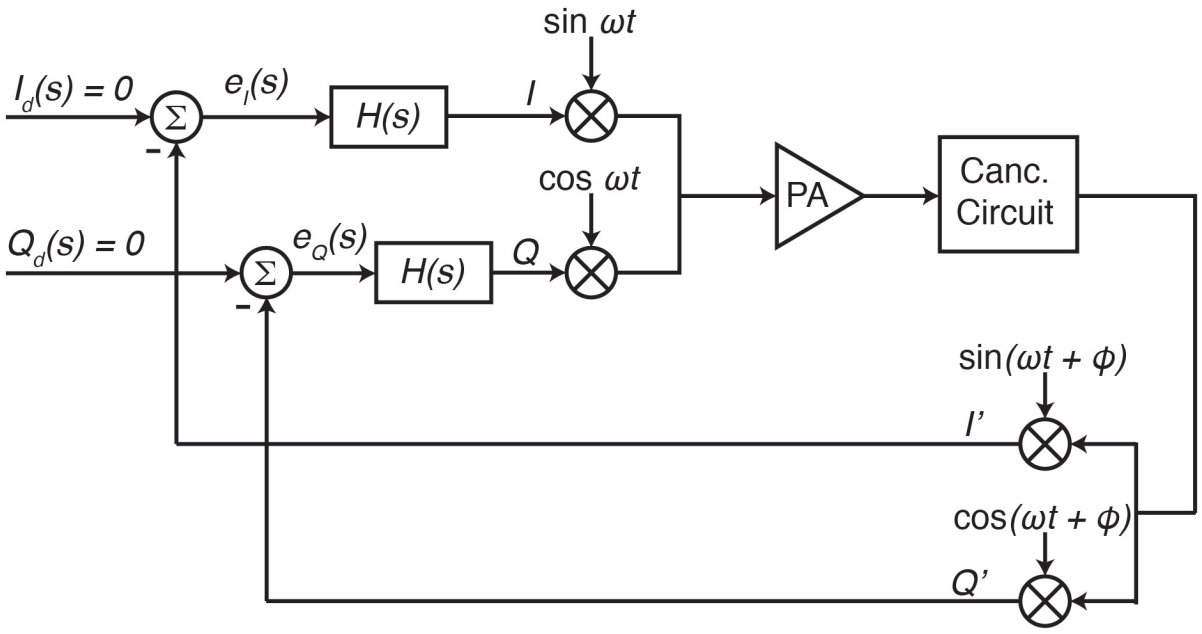

Figure 2.17: Block diagram for Cartesian feedback and PID control of MPI active interference cancellation system. Each interfering harmonic is separately demodulated, controlled, and upmodulated as a cancellation signal to be transformer-coupled into the main MPI drive field. At each harmonic frequency, the feedthrough interference signal is detected via a dedicated sniffer coil in series with the MPI detector coil and demodulated into in-phase (I) and quadrature (Q) components. The detected feedthrough interference error signal is input into a tuned PID controller (shown as $H\,(s)$, upmodulated, amplified, and coupled into the main MPI drive field. Acronyms: I_d and Q_d: desired in-phase and quadrature signals; e_I and e_Q: in-phase and quadrature error signals; H(s): controller implementation; PA: power amplifier; canc. circuit: cancellation signal to be transformer-coupled into main MPI drive field.

and quadrature components do not interact with each other. Hence, prior to MPI scanning, I implemented a software-driven system calibration sequence at each interfering harmonic to determine system phase accrual. Other approaches to phase calibration are also widely discussed in literature [52].

Additionally, because a narrowband signal can be precisely controlled using Cartesian feedback by demodulating the signal first down to baseband, the controller does not require excessively high control bandwidth, making it highly applicable for MPI applications. In our prototype controller setup, we were able to achieve 0.5 Hz control loop bandwidth, which is sufficient to account for the slow thermal drifts that can modulate MPI harmonic interference signals. Future designs using real-time programmable logic boards can incorporate the control system directly in hardware for improved speed.

2.3.3 Active Cancellation Suppresses MPI Feedthrough Interference to Below System Noise Floor

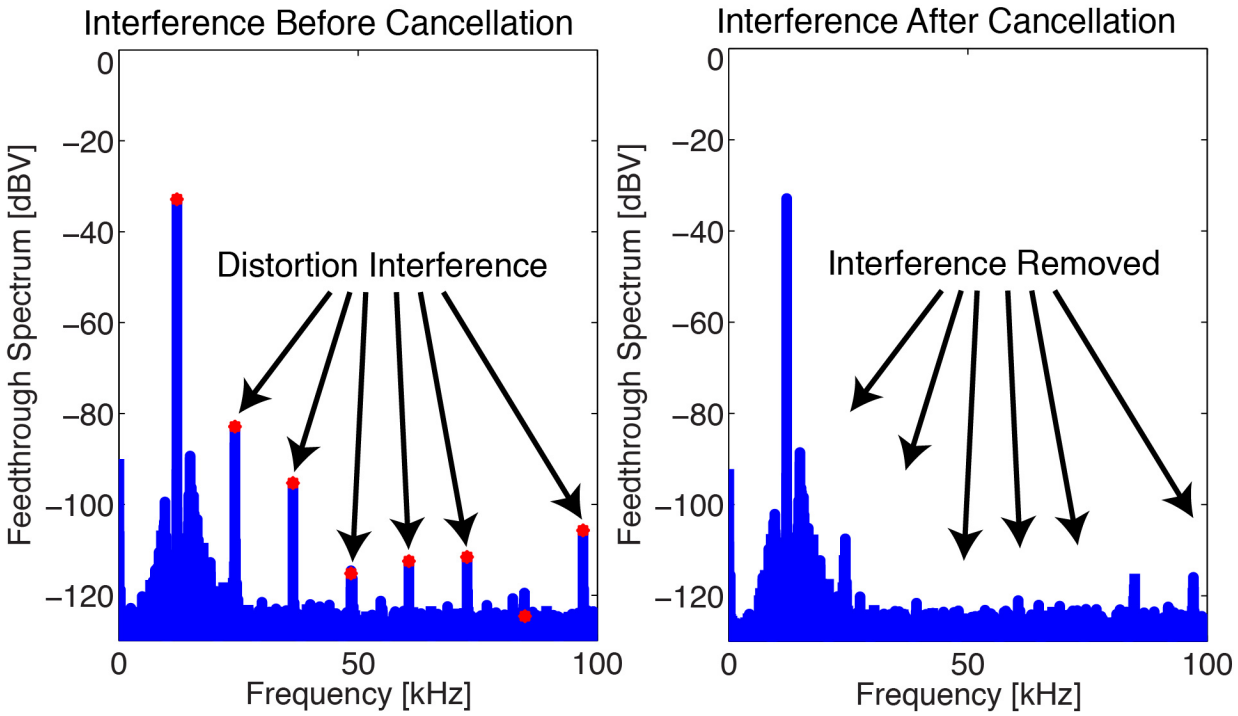

Figure 2.18: Active interference cancellation successfully suppresses 8 interfering harmonic signals to below system noise spectrum. Received signal spectrum before (left) and after (right) active cancellation of $2f_0$ to $9f_0$. Active harmonic interference cancellation circuit was able to suppress interfering signals to below system noise floor. Red dots: harmonics of fundamental drive field frequency.

Figure 2.18 shows the power spectra for the received MPI signal before and after active cancellation of distortion interference from $2f_0$ to $9f_0$. After active cancellation, interference at all frequencies was suppressed below the system noise floor. Interference at $2f_0$ decreased by as much as 45 dB. Interestingly, 60 Hz side lobes from intermodulation distortion products near the interfering frequencies was not attenuated with active cancellation, suggesting that intermodulation mixing with power line signals occurs before the active cancellation in the main transmit chain.

Figure 2.19 shows the dynamic response of harmonic interference at $2f_0$ and $3f_0$ after the Cartesian feedback control system for active interference cancellation is turned in in the MPI testbed. The time-varying control loop executes every 1 second. After 9 control loops, both interfering harmonic signals are suppressed by over 55 dB to below the system noise

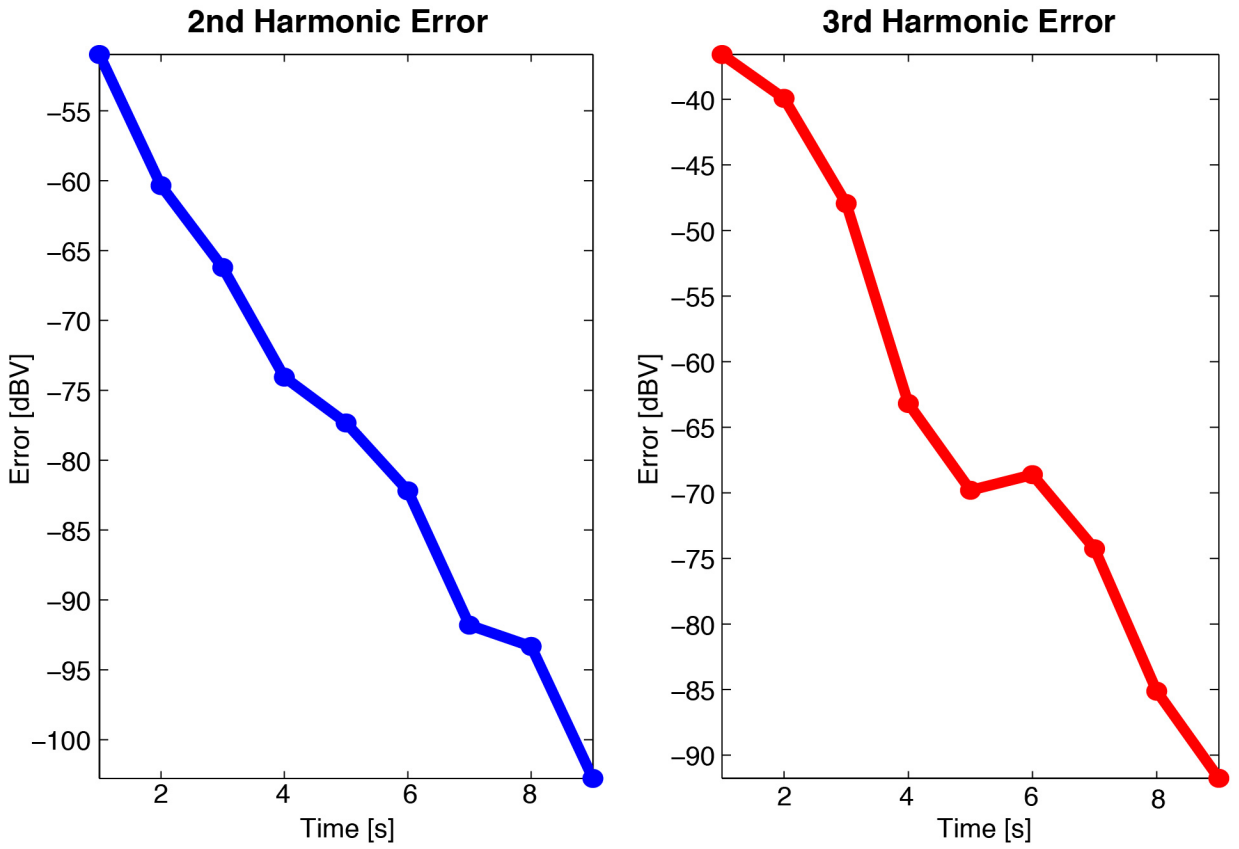

Figure 2.19: Cartesian-feedback PID controller for MPI active interference cancellation dynamically suppresses feedthrough interference. The error signal at the 2^{nd}(left) and 3^{rd}(right) harmonics of the fundamental drive field frequency are shown as a function of time after the active cancellation controller is turned on. After 9 control loops, both interfering harmonic signals are suppressed by over 55 dB.

floor. The controller can be expanded to further suppress interfering signals at all harmonics of the fundamental drive field frequency in MPI to below the system noise floor.

2.4 Discussion

In this chapter, we have shown that direct feedthrough interference in MPI may severely limit the detection sensitivity and SNR of MPI scanners. Although the fundamental drive field frequency interference is inevitable in current iterations of MPI systems, we have shown that filtering it from the detected signal spectrum results in a benign and robustly recoverable image artifact. However, higher-order harmonic interference in the MPI detector signal can directly interfere with SPIO particle signal and must be suppressed.

To investigate the source of harmonic distortion interference in the MPI drive field, we designed and constructed a non-imaging, modular MPI testbed system. Innovations to reduce harmonic interference in the MPI testbed system are directly translatable to existing MPI scanners. Using the testbed system, we have shown that resonant capacitors that generate the MPI drive field can contribute significant distortion interference. The mechanism underlying capacitor distortion may be modeled by changes in capacitance due to dielectric strain from capacitor plate forces. We predicted that capacitor distortion may continue to decrease with increasing capacitor voltage ratings. Using the MPI testbed system, we also investigated additional distortion interference mechanisms, including interactions between the generated AC magnetic field in the transmit coil and the magnetic gradient. Here, we discovered that the permanent magnet-generated field gradient in MPI can also contribute significant harmonic interference to the MPI detector signal, particularly at $2f_0$.

Based on these findings, we sought various methods to suppress the harmonic interference arising from these hardware systems. Here we have demonstrated a method to actively cancel distortion interference in the detected MPI signal using a transformer-coupled cancellation circuit. Furthermore, we demonstrated that this interference-cancellation system can be actively controlled in software using a Cartesian feedback controller for each interfering harmonic frequency. With this circuit, we have demonstrated a control loop bandwidth of 0.5 Hz and shown than up to 55 dB of interference suppression such that all actively cancelled interference can be attenuated to below the noise floor.

Chapter 3

Optimal Noise Matching in MPI

Magnetic Particle Imaging is a medical imaging technique that directly images superparamagnetic iron oxide nanoparticle tracers in the body and has the potential to be an extremely sensitive imaging technique. When the total injectable tracer dose is taken into consideration, MPI detection sensitivity may be comparable to nuclear medicine techniques like PET (Positron Emission Tomography) or SPECT (Single Photon Emission Computed Tomography) imaging [54, 6].

Like nuclear medicine techniques, biological tissues neither generate signal in MPI nor interfere with SPIO particle magnetization signals in MPI. Hence, it may be possible to visualize small quantities of SPIO tracer deep in the body to sensitively track therapeutic administrations of cell-based therapies or to better diagnose disease features such as tumors, vascular obstructions, or sites of inflammation. To enable these MPI applications in the clinic, it is important to investigate the physical limits of sensitivity and noise-generation mechanisms in MPI and to engineer methods to reach these physical detection limits.

In this work, we investigate the noise generation mechanisms in MPI and demonstrate a method to perform optimal noise matching to the detector coil of a 7 T/m preclinical MPI imager. We begin with a review of generalized noise theory for electronic systems. We then describe noise sources and noise matching for a MPI detector coil. Finally, we describe a custom preamplifier designs and noise-matching method that enables an optimized 3 dB noise figure for the MPI detector system in a 7 T/m 3D small-animal MPI scanner.

3.1 An introduction to noise in electronic measurement systems

The modeling of electronic noise in low-level voltage sensor-based detector systems has been previously studied and described in detail [55, 56, 57, 58, 59, 60, 61].

In these systems, a transducer converts a signal to be measured to a voltage, which then is amplified using a low-noise preamplifier before further signal conditioning steps. The use of a low-noise preamplifier step ensures that all electronics downstream of the sensor do not

add unnecessary noise to the detected signal and thereby degrade the signal-to-noise ratio (SNR) or detection sensitivity of the system.

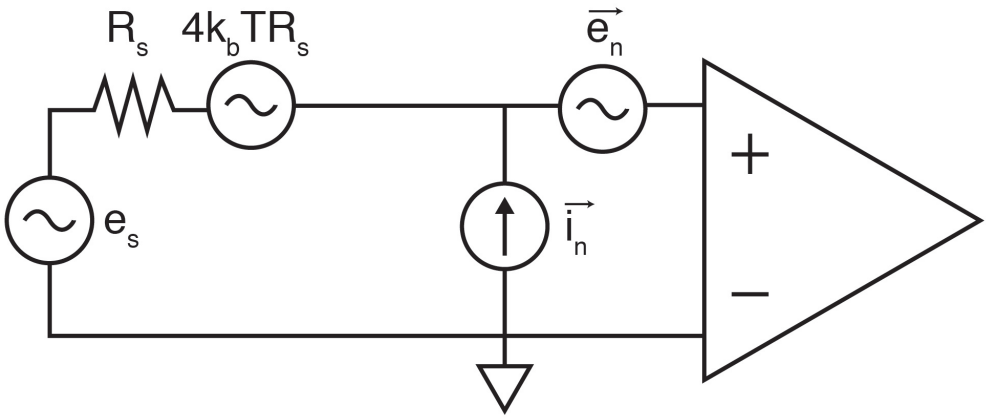

Figure 3.1: Generalized circuit noise model for voltage-based electronic measurement systems. The signal transducer model is shown as a Thevenin voltage source with signal e_s, where the sensor noise arises from the thermal noise of the source resistance (R_s). Electronic noise in the amplifier can be modeled using a serial voltage noise source with variance $\bar{e}_n^2$ and parallel current noise source with variance $\bar{i}_n^2$.

A noise model of this detector system is shown in Fig. 3.1, where the sensor is shown as a Thevenin equivalent voltage source [55, 57]. The sources of electronic noise in such a system can be encapsulated in the thermal noise in the detector arising from its Thevenin resistance and the voltage ($\bar{e}_n$) and current ($\bar{i}_n$) noise of the preamplifier. For the purpose of this work, we will assume that all noise sources are uncorrelated, which is a good assumption for most amplifier configurations [55, 60]. The total voltage noise variance of the system, in $\mathrm{V^2\,Hz^{-1}}$, can then be expressed:

$$4k_bTR_s + \bar{e}_n^2 + \bar{i}_n^2 {R_s}^2 \tag{3.1}$$

where k_b is Boltzmann's constant, T is the temperature of the detector in Kelvin, R_s is the detector Thevenin resistance, $\bar{e}_n$ is the amplifier voltage noise in $\mathrm{V}/\sqrt{\mathrm{Hz}}$, and $\bar{i}_n$ is the amplifier current noise in $\mathrm{A}/\sqrt{\mathrm{Hz}}$.

A standard method of characterizing the noise performance for a given detector-amplifier configuration is through the use of noise figure (NF), which is defined as the SNR of the amplifier output divided by the corresponding ratio at the input, expressed either as a ratio or in decibels. For the detector-amplifier systems described here, the NF is simply the relative ratio of the total input-referred noise in the system as compared to the detector noise alone. Notably, a NF below three 3 dB implies that the total noise is dominated by thermal noise from the detector resistance and that the system is therefore "noise-matched." We show the expression for NF:

$$\mathrm{NF} = 10 \cdot \log_{10} \frac{4k_bTR_s + \bar{e}_n^2 + \bar{i}_n^2 {R_s}^2}{4k_bTR_s} \tag{3.2}$$

A differentiation of Equation 3.2 shows that NF can be minimized for a specific detector resistance when $R_s = \bar{e}_n/\bar{i}_n$. At this detector resistance, the lowest achievable NF is:

$$\mathrm{NF} = 10 \cdot \log_{10} \left(1 + \frac{\bar{e}_n^2 + \bar{i}_n^2 \cdot \frac{\bar{e}_n^2}{\bar{i}_n^2}}{4k_bT \cdot \frac{\bar{e}_n}{\bar{i}_n}} \right) \tag{3.3}$$

$$= 10 \cdot \log_{10} \left(1 + \frac{\bar{e}_n \bar{i}_n}{2k_bT} \right) \tag{3.4}$$

which is governed only by the amplifier's voltage noise-current noise product and detector temperature. As a result, when choosing low-noise amplification devices, the product of $\bar{e}_n$ and $\bar{i}_n$, not their individual values, is the appropriate figure-of-merit to use for evaluating their lowest achievable noise performance.

A summary of $\bar{e}_n$, $\bar{i}_n$, input capacitance, and minimum achievable NF at room temperature for several common low-noise amplification devices at the audio frequency range is shown in Table 3.1. While all of these devices show a minimum NF below 3 dB that would enable detector-noise dominance, the JFET devices perform especially well due to their low current noise values. As will be shown later in this chapter, this low current-noise behavior of JFETs enables a broader bandwidth for noise-matching in MPI applications.

3.2 Noise in MPI detectors

Current MPI scanner designs use an induction coil-based sensor to detect SPIO magnetization signals [1, 46, 2, 44, 45]. This type of detector is not dissimilar to the detector coils used in MRI, albeit at much lower frequency and a relatively broader signal bandwidth. An equivalent noise circuit model for induction-based signal detection systems like MPI and MRI is shown in Figure 3.2, where $\mathrm{R_P}$ is the equivalent resistance from the patient's body that can generate coupled noise in the MPI signal, L is the inductance of the detector coil, and $\mathrm{R_L}$ is the detector coil resistance.

Patient-induced resistance scales linearly with the patient-coil filling factor and coil inductance, and quadratically with frequency with a power of 2 to 2.1 [62, 45]. At radiofrequencies in the 100 MHz range used in MRI, this patient-induced noise can exceed that of noise generated by the detector coil and forms the limiting basis for system noise [62]. As a result, when the detector system noise is dominated by the patient's body noise, the noise performance of such systems has reached their physical limits and cannot be significantly further improved.

However, at MPI frequencies in the very-low frequency (VLF) frequency regime, patient-induced coil resistance can be exceedingly small, potentially ranging from the 1 to 100

Device	Device Type	$\bar{e}_n$ (nV/$\sqrt{\text{Hz}}$)	$\bar{i}_n$ (fA/$\sqrt{\text{Hz}}$)	Cin (pF)	Optimal NF (dB)
InterFET IF3601	JFET	0.3	18	300	0.003
NXP Semiconductors BF862	JFET	0.8	18	10	0.007
Linear Systems LSK170	JFET	0.9	18	22	0.008
Analog Devices ADA4817	JFET OPA	4	3	1.3	0.005
Stanford Research Systems SR560	JFET Preamp	4	8	25	0.017
Texas Instruments OPA211	BJT OPA	1.1	1700	8	0.884
Exar CLC1002	BJT OPA	0.6	4200	2	1.154
Texas Instruments LME49990	BJT OPA	0.9	2800	-	1.154
ST Microelectronics TSH300	BJT OPA	0.65	3300	-	1.000

Table 3.1: Voltage noise, current noise, input capacitance, and lowest achievable noise figure at room temperature for several available low-noise amplification devices for use in the 1-100 kHz frequency range. JFET: junction field-effect transistor; BJT: bipolar junction transistor; OPA: operational amplifier.

mΩ range for human subjects [63, 45] and even lower for preclinical scanners. Hence, to reach patient-noise dominance in MPI requires highly sensitive, low-noise detector coils that potentially require cryogenic cooling. The current generation of MPI detector coil designs have not yet achieved patient noise dominance.

Preclinical MPI scanners developed at our group and others [44, 8, 45] demonstrate a coil resistance noise which far exceeds that arising from the animal subject. As a result, for the purpose of noise-matching in MPI in this chapter, we will only consider thermal noise arising from the resistance of the detector coil. Taking the reactance of the inductive sensor into the generalized noise figure expression in Eqn. 3.2, we arrive at the noise figure equation for inductive MPI receivers:

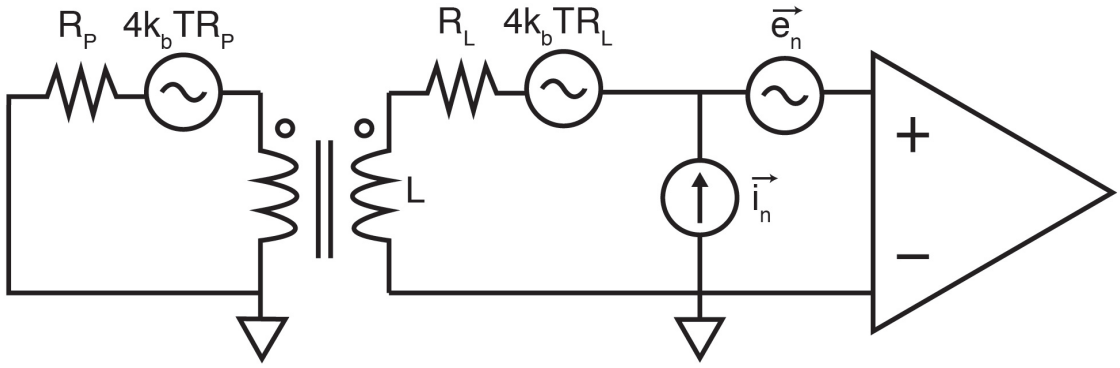

Figure 3.2: Circuit noise model for inductive sensor-based MPI detectors. In these transducer system, the source impedance is comprised of both the coil resistance R_L and coil inductance L. An additional source of noise in the system is the thermal noise from the patient, which can be modeled using a resistor (R_P) and can inductive couple into the MPI detector signal.

$$\mathrm{NF} = 10 \cdot \log_{10} \frac{4k_bTR_L + \bar{e}_n^2 + \bar{i}_n^2 {Z_L}^2}{4k_bTR_L} \tag{3.5}$$

$$= 10 \cdot \log_{10} \frac{4k_bTR_L + \bar{e}_n^2 + \bar{i}_n^2 \left(|\omega L|^2 + {R_L}^2\right)}{4k_bTR_L} \tag{3.6}$$

where $\omega/2\pi$ is the frequency in Hz and Z_L is the frequency-dependent impedance of the inductive detector coil. Typical resistance values for the MPI detector coil range from 0.1 to 10 Ω, which corresponds to a thermal noise voltage between 40 and 400 pV/$\sqrt{\text{Hz}}$ and is significantly smaller than the voltage noise of most amplifier devices (Table 3.1). As an example, when we use the excellent commercial Stanford Research Systems SR560 low-noise preamplifier and a 500 µH, 5 ohm MPI detector coil, the thermal noise from the detector coil is 290 pV/$\sqrt{\text{Hz}}$, while the voltage noise from the amplifier is 4 nV/$\sqrt{\text{Hz}}$. This combination results in a system noise figure of 23 dB. Thus it is clear that the relative noise contribution of the preamplifier voltage noise must be reduced via a noise-matching technique to lower the NF and improve the MPI signal-noise ratio.

We note that in Equation 3.6, the current noise term increases with frequency because the reactance of the detector coil scales linearly with frequency. As a result, it is not possible to optimally match the voltage and current noise of any amplifier system to the thermal noise of the reactive MPI detector coil over a wide bandwidth [64]. Assuming the AC reactance of the detector coil is significantly greater than its resistance, the frequency at which the current noise contribution begins to dominate the amplifier voltage noise can then be derived:

$$\bar{e}_n^2 = \bar{i}_n^2 \omega^2 L^2 \tag{3.7}$$

$$\omega = \frac{\bar{e}_n}{\bar{i}_n L} \tag{3.8}$$

Hence it can be seen that for a given voltage noise value $\bar{e}_n$, devices with extremely low $\bar{i}_n$, such FETs, are necessary to extend the optimally noise-matched bandwidth for reactive MPI detectors.

Further confounds that may limit the usable bandwidth of MPI detector systems include 1) the self-resonance of detector coils and 2) the undesirable LC resonance between detector coil inductance and input capacitance of preamplifier systems. In the first case, the parasitic self-capacitance of MPI detector coils begins to dominate coil inductance past the self-resonance frequency, such that the coil behavior is more capacitive than inductive and limits its use as a magnetic field transducer. Hence, when designing MPI detector coils, we must ensure that the self-resonant frequency of MPI detector coils occurs beyond the MPI signal bandwidth. Additionally, the detector inductance can also resonate with the input capacitance of the preamplifier, which would cause amplitude and phase shifts in the detected MPI signal. Although it is possible to precharacterize this resonance behavior for image reconstruction [45]. such techniques may be susceptible to system thermal drifts or patient loading in the detector. Therefore, we will define the usable MPI signal bandwidth to be the lower of these detector coil-associated resonant frequencies. In practice, the LC resonant frequency between the MPI detector coil and the preamplifier input capacitance is almost always lower than the self-resonant frequency of the detector coil. In this case, the signal bandwidth can be written as the resonant frequency of the detector coil inductance with the input capacitance of the preamplifier:

$$\omega = \frac{1}{\sqrt{L \cdot C_{in}}} \tag{3.9}$$

where C_{in} is the input capacitance of the preamplifier.

In the following subsections, we will explore three methods to noise-match to the inductive detector coil in MPI.

3.2.1 Noise-matching in MPI by changing the number of turns in the MPI detector coil

One method of performing optimal noise-matching in MPI is through increasing the number of turns in the detector coil such that the coil detects magnetization signals with more sensitivity [55]. Assuming that the geometry of the MPI detector coil is static over time, then according to the Principle of Reciprocity [65], the voltage signal generated in inductive sensors is:

$$\xi = -\mathbf{B_1} \cdot \frac{\mathrm{d}\mathbf{m}}{\mathrm{dt}} \tag{3.10}$$

where $\mathbf{B_1}$ is the sensitivity of the detector coil (or, equivalently, the field that is generated by the coil per unit current in T/A) and $\mathbf{m}$ is the detected magnetization signal.

The intrinsic SNR of the MPI detector system can then be expressed in relation to the coil sensitivity and the overall system noise:

$$\mathrm{SNR} \propto \frac{\mathbf{B_1}}{\sqrt{4k_bTR_L + \bar{e}_n^2 + \bar{i}_n^2 {Z_L}^2}} \tag{3.11}$$

To understand how the noise figure scales with the number of turns in the detector coil, we first show a simplified diagram of a MPI detector coil. In Figure 3.3, a solenoidal detector coil configuration is shown, where $\mathrm{L_c}$ and $\mathrm{W_c}$ are the length and thickness of the coil, $\mathrm{R_c}$ is the average coil radius, and $\mathrm{N_t}$ is the number of turns in the coil. We note that although a solenoidal coil configuration is shown, the following analyses are applicable to other detector coil geometries.

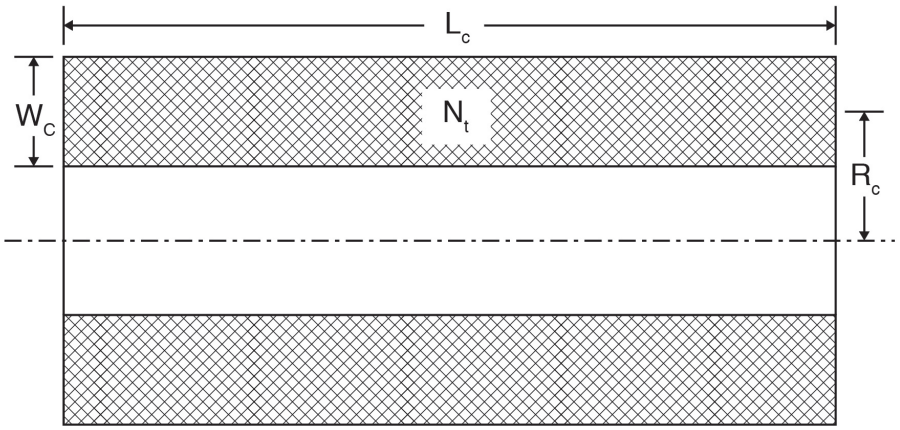

Figure 3.3: Generalized cross-section diagram of MPI detector coil geometry, showing a solenoidal coil configuration. $\mathrm{L_c}$ and $\mathrm{W_c}$ are the length and thickness of the coil, $\mathrm{R_c}$ is the average coil radius, and $\mathrm{N_t}$ is the number of turns in the coil.

To investigate the scaling of NF with the number of turns in the detector coil, we will vary $\mathrm{N_t}$ and fix $\mathrm{L_c}$, $\mathrm{W_c}$, and $\mathrm{R_c}$. In practice, this is equivalent to keeping the size of the detector coil constant to meet bore space constraints while changing the number of turns and cross-sectional area of the wire used for the coil windings. From Ampere's law, the magnetic field generated per unit current of such a coil, and therefore its $\mathbf{B_1}$ sensitivity, scales linearly with the number of turns, i.e.

$$\mathbf{B_1} \propto N_t \tag{3.12}$$

The inductance of the detector coil scales quadratically with the number of its turns [66], i.e.

$$L \propto N_t^2 \tag{3.13}$$

Finally, the resistance of detector coil windings can be expressed:

$$R = \frac{\rho L_w}{A_w} \tag{3.14}$$

$$\propto \frac{\rho \cdot 2\pi R_c \cdot N_t}{A/N_t} \tag{3.15}$$

$$\propto \frac{\rho \cdot 2\pi R_c \cdot N_t^2}{L_\mathrm{c} W_\mathrm{c}} \tag{3.16}$$

where L_w is the length of wire used in the coil, A_w is the cross-sectional area per turn, ρ is the resistivity of the coil, and A is the total coil cross-sectional area.

Hence, if we increase the number of turns in the detector coil by a factor of $\mathrm{N_t}$, then the SNR equation becomes:

$$\mathrm{SNR} \propto \frac{\mathbf{B_1} \cdot N_t}{\sqrt{4k_bTR_LN_t^2 + \bar{e}_n^2 + \bar{i}_n^2 \left(Z_L N_t^2\right)^2}} \tag{3.17}$$

$$\propto \frac{\mathbf{B_1}}{\sqrt{4k_bTR_L + \frac{\bar{e}_n^2}{N_t^2} + \bar{i}_n^2 {Z_L}^2 N_t^2}} \tag{3.18}$$

Equivalently, the MPI noise figure becomes:

$$\mathrm{NF} = 10 \cdot \log_{10} \frac{4k_bTR_L + \frac{\bar{e}_n^2}{N_t^2} + \bar{i}_n^2 \left(|\omega L|^2 + {R_L}^2\right) N_t^2}{4k_bTR_L} \tag{3.19}$$

These equations show that changing the number of turns in the MPI detector coil corresponds to a decrease in preamplifier voltage noise contribution and a corresponding increase in the current noise contribution to the total system noise. It is important to note that the preamplifier voltage noise has not decreased in reality, but rather that other voltages in the system have increased in comparison, i.e. from the increase in coil sensitivity to SPIO magnetization, thermal noise in the coil, and current noise through the coil reactance. However, the net result is that the apparent preamplifier voltage noise $\bar{e}_n$ has decreased by a factor of $\mathrm{N_t}$, while the apparent current noise $\bar{i}_n$ has increased by $\mathrm{N_t}$.

Increasing the number of turns in the detector coil also results in a decreased MPI signal bandwidth due to the real increase in coil inductance:

$$\omega = \frac{1}{\sqrt{N_t^2 L \cdot C_{in}}} \tag{3.20}$$

3.2.2 Noise-matching in MPI by paralleling preamplifier devices

Another method to improve the noise figure for MPI detector systems is to place multiple amplification devices in parallel [67, 61, 45, 56]. In this method, the output of the MPI detector coil is connected to the parallel-connected input of multiple preamplifiers. The voltage noise of this system is equivalent to the voltage noise of each amplifier added in parallel. Because noise variances add, the equivalent voltage noise of the system is then:

$$\frac{1}{\bar{e}_{n\_eq}^2} = \frac{1}{\bar{e}_{n\_1}^2} + \dots \frac{1}{\bar{e}_{n\_N_p}^2} \tag{3.21}$$

for N_p devices. If each device has equal voltage noise $\bar{e_n}$, then the equivalent voltage noise becomes:

$$\bar{e}_{n\_eq} = \frac{\bar{e}_n}{\sqrt{N_p}} \tag{3.22}$$

Similarly, the equivalent current noise is the parallel addition of the individual device current noise contributions:

$$\bar{i}_{n\_eq} = \sqrt{N_p} \cdot \bar{i}_n \tag{3.23}$$

The MPI SNR equation then becomes:

$$\text{SNR} \propto \frac{\mathbf{B_1}}{\sqrt{4k_bTR_L + \frac{\bar{e}_n^2}{N_p} + \bar{i}_n^2 {Z_L}^2 N_p}} \tag{3.24}$$

and the NF equation becomes:

$$\text{NF} = 10 \cdot \log_{10} \frac{4k_bTR_L + \frac{\bar{e}_n^2}{N_p} + \bar{i}_n^2 \left(|\omega L|^2 + {R_L}^2\right) N_p}{4k_bTR_L} \tag{3.25}$$

It can be seen therefore that paralleling multiple amplifier devices has the same net effect for tuning the voltage and current noise contributions to the overall noise figure as changing the number of turns on the detector coil. This is also true for the signal bandwidth, as the input capacitance of the parallel devices are also added, such that

$$\omega = \frac{1}{\sqrt{L \cdot N_p C_{in}}} \tag{3.26}$$

3.2.3 Noise-matching in MPI by the use of an input transformer

A third method for performing noise-matching in MPI detector systems is via the use of an input transformer between the detector coil and the preamplifier [60, 55, 56, 57, 59, 61]. In this method, a transfomer with primary to secondary turns ratio 1:N_x is placed in series with the amplifier input. The use of a transformer increases the detected SPIO magnetization voltage by a factor of N_x, as referred to the input of the amplifier. It also increases the detector impedance by a factor of N_x^2. Thus, when an input-matching transfomer is applied, the SNR equation becomes:

$$\text{SNR} \propto \frac{\mathbf{B_1} \cdot N_x}{\sqrt{4k_bTR_LN_x^2 + \bar{e}_n^2 + \bar{i}_n^2 \left(Z_LN_x^2\right)^2}} \tag{3.27}$$

$$\propto \frac{\mathbf{B_1}}{\sqrt{4k_bTR_L + \frac{\bar{e}_n^2}{N_x^2} + \bar{i}_n^2 {Z_L}^2 N_x^2}} \tag{3.28}$$

The change in SNR via the use of an input transformer is therefore equivalent to that caused by a change in the number of turns in the detector coil. The system noise figure and signal bandwidth also scale similarly between these two noise-matching techniques, such that:

$$\text{NF} = 10 \cdot \log_{10} \frac{4k_bTR_L + \frac{\bar{e}_n^2}{N_x^2} + \bar{i}_n^2 \left(|\omega L|^2 + {R_L}^2\right) N_x^2}{4k_bTR_L} \tag{3.29}$$

$$\omega = \frac{1}{\sqrt{N_x^2 L \cdot C_{in}}} \tag{3.30}$$

A diagram of all three noise-matching techniques is shown in Fig. 3.4. The three techniques presented have identical performance in reducing noise figure performance and signal bandwidth. Combining the the noise figure equations for each technique (Eqns. 3.19, 3.25, and 3.29) yields a generalized MPI noise-matching equation:

$$\text{NF} = 10 \cdot \log_{10} \frac{4k_bTR_L + \frac{\bar{e}_n^2}{N} + \bar{i}_n^2 \left(|\omega L|^2 + {R_L}^2\right) N}{4k_bTR_L} \tag{3.31}$$

where the equivalent noise-matching ratio $N = N_pN_x^2N_t^2$. The equivalent signal bandwidth at which the detector coil resonates with the amplifier input capacitance can also be rewritten from Eqns. 3.20, 3.26, and 3.30:

$$\omega = \frac{1}{\sqrt{N \cdot LC_{in}}} \tag{3.32}$$

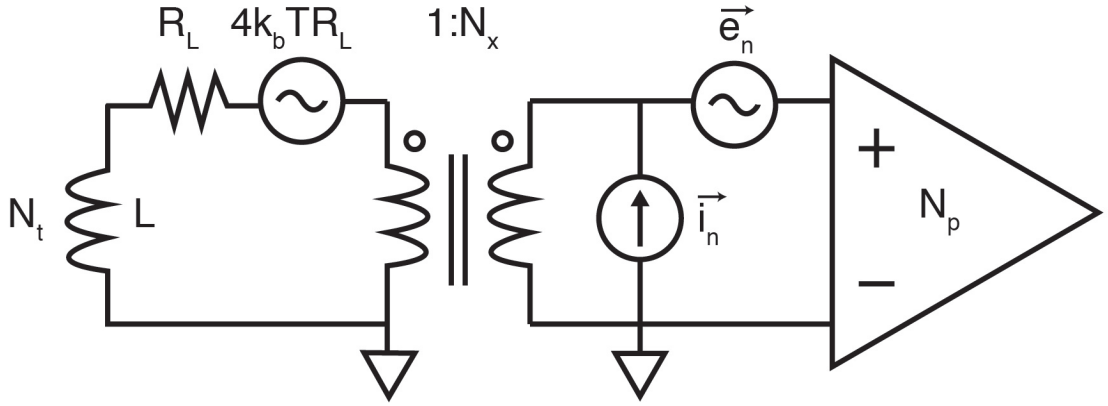

Figure 3.4: Summary of noise-matching techniques for MPI detector systems, ignoring thermal noise from the patient. To reduce the apparent voltage noise contribution from the preamplifier, it is possible to increase the number of turns in the MPI detector coil N_t, the number of parallel amplifier devices N_p, or through the addition of a 1: N_x input transformer. All three techniques have equivalent effects on system noise figure and bandwidth.

Additionally, a modification to Eqn. 3.16 yields that the frequency at which the current noise contribution begins to dominate voltage noise in the system noise figure is

$$\omega = \frac{\bar{e}_n}{N\bar{i}_n L} \tag{3.33}$$

As can be seen, overly aggressive noise-matching using large values of N can significantly reduce the bandwidth over which the MPI detector system is properly noise-matched, unless the current noise of the amplification device can be made exceptionally low. Therefore, for any given combination of MPI detector coils and amplifier devices, changing the noise-matching parameter N incurs a tradeoff between the lowest achievable system noise figure and the noise-matched bandwidth and detector coil LC resonant frequency. The amplification device chosen and the noise-matching factor N must then be carefully chosen to keep system NF low while maintaining an acceptable MPI bandwidth.

3.2.4 Maximum achievable 3 dB noise-matched bandwidth for MPI detector coil-preamplifier combinations

Building upon the previous sections on noise-matching in MPI, we now describe the process of choosing a suitable amplification device for MPI detectors. The MPI signal is inherently broadband, where SPIO magnetization signals can extend from 40 kHz to potentially over 1 MHz for a drive field frequency at 20 kHz. Therefore, a reasonable goal for the MPI preamplifier is to achieve the highest achievable bandwidth in the MPI signal spectrum

for which the detector coil is 3 dB noise-matched to the preamplifier. To determine this bandwidth for a given amplifier device, we can solve Eqn. 3.31 for optimal N when the noise figure is 3 dB (assuming that the coil Q-factor is large, or $|\omega L| \gg R_L$):

$$10 \cdot \log_{10} \frac{4k_bTR_L + \frac{\bar{e}_n^2}{N} + N\bar{i}_n^2\omega^2L^2}{4k_bTR_L} = 3 \tag{3.34}$$

$$\frac{\frac{\bar{e}_n^2}{N} + N\bar{i}_n^2\omega^2L^2}{4k_bTR_L} = 1 \tag{3.35}$$

$$\bar{i}_n^2\omega^2L^2N^2 - 4k_bTR_LN + \bar{e}_n^2 = 0 \tag{3.36}$$

Equation 3.36 is a simple polynomial function of N in the form $aN^2 + bN + c = 0$, where $a = \bar{i}_n^2\omega^2L^2$, $b = -4k_bTR_LN$, and $c = \bar{e}_n^2$. The roots of Eqn. 3.36 correspond to the noise-matching factor N necessary to achieve 3 dB noise-matching for the given set of coil and preamplifier parameters. Determining the maximum achievable 3 dB noise-matched frequency, ω_{max}, for which a real value for N can be found is equivalent to solving the quadratic formula for the maximum value of a under the condition that the roots remain real numbers. This can be determined when there is a single real root in the quadratic function, corresponding to the case where $\sqrt{b^2 - 4ac} = 0$ in the quadratic formula.

Setting $\sqrt{b^2 - 4ac} = 0$, we then find:

$$(4k_bTR_L)^2 - 4\bar{i}_n^2\bar{e}_n^2L^2\omega_{max}^2 = 0 \tag{3.37}$$

$$\omega_{max} = \frac{2k_bTR_L}{\bar{i}_n\bar{e}_nL} \tag{3.38}$$

Solving for the roots of N in Eqn. 3.36, we find that at ω_{max}, $N = \frac{\bar{e}_n^2}{2k_bTR_L}$. This value of N also intuitively makes sense, as the voltage noise and current noise contributions at this N are identical and equal to half the total noise from the coil resistance. Hence, for any given combination of MPI detector coils and preamplifiers, the maximum frequency at which the detector system is 3 dB noise-matched (if a noise figure of 3 dB is possible at all) is ω_{max} when the noise-matching factor $N = \frac{\bar{e}_n^2}{2k_bTR_L}$.

In summary, we have presented three methods for optimal noise matching in the MPI detector system, which include changing the number of turns in the detector coil, paralleling active devices in the preamplifier, and adding the use of an input matching transformer. All three techniques presented are theoretically identical in noise-matching performance.

However, these noise-matching techniques also incur the same penalties in limiting the MPI detector bandwidth and must be carefully applied to avoid excessive current noise or LC resonance effects. We have also shown that for any combination of MPI detector coils and preamplifiers, it is possible to calculate the maximum achievable 3 dB noise-matched frequency and its associated noise-matching factor N.

3.3 Design of a noise-matched MPI preamplifier

Having established a theoretical basis for optimal noise matching in MPI detector coils, we now describe the procedure for improving the noise figure for a 7 T/m preclinical FFP MPI scanner. The prototype solenoidal detector coil used in the preclinical MPI scanner has an inductance of approximately 500 µH and resistance of 5 Ω, which has a thermal noise voltage of 290 pV/$\sqrt{\text{Hz}}$.

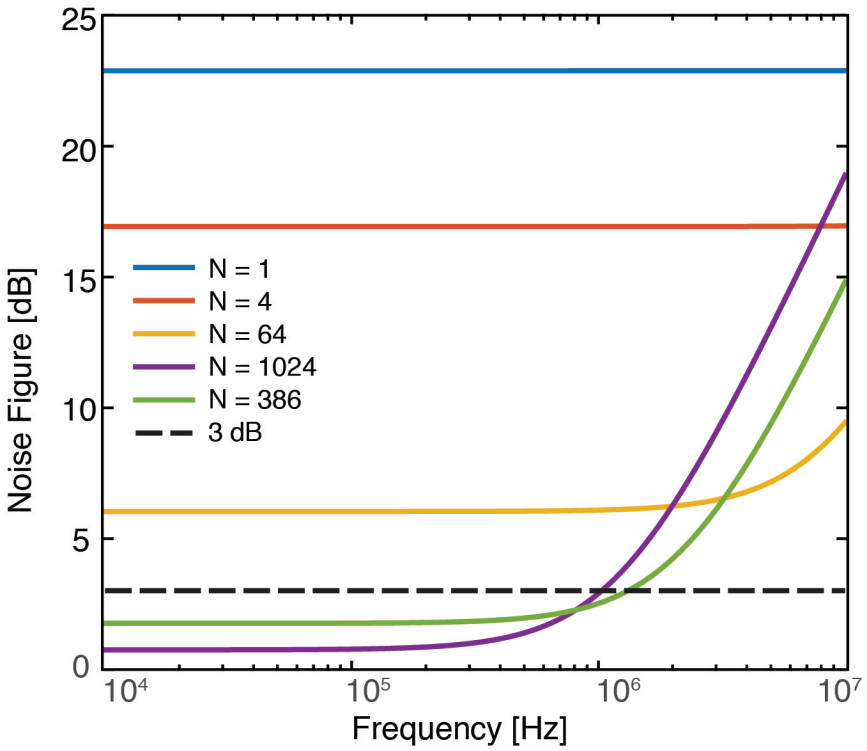

Figure 3.5: Calculated noise figure as a function of frequency and noise-matching factor N for the ADA4817 operational amplifier. The maximum achievable bandwidth over which the system has a noise figure less than 3 dB is 1.3 MHz, which occurs at N = 386. Note: JFET flicker noise is not shown here, but the input voltage noise for the ADA4817 is less than 5 nV/$\sqrt{\text{Hz}}$ from 10 kHz onward.

We begin by choosing a device with low input noise that can achieve high signal bandwidth. We used two figures of merit in selecting an appropriate preamplifier device. First, the product $\bar{e}_n \bar{i}_n$ gives an excellent metric for the lowest achievable NF (from Eqn. 3.4) and noise-matched bandwidth (from Eqn. 3.38). Second, the expression $\bar{e}_n^2 C_{in}$ is useful for evaluating the effect on the LC resonant frequency between the coil inductance and the preamplifier input capacitance due to noise-matching. A similar figure of merit for low-noise amplifiers is discussed in [61].

Based on these figures of merit, we chose the extremely low-noise JFET operational amplifier ADA4817 from Analog Devices (Table 3.1), which has $\bar{e}_n$ at 4 nV/$\sqrt{\text{Hz}}$, $\bar{i}_n$ at 2.5 fA/$\sqrt{\text{Hz}}$, and C_{in} at 1.3 pF. The flicker noise for this device occurs mainly at frequencies below 10 kHz. From 10 kHz onward the voltage noise is rated at less than 5 nV/$\sqrt{\text{Hz}}$; from 100 kHz onward it is below 4 nV/$\sqrt{\text{Hz}}$.

Solving Eqn. 3.38 for this amplifier and detector coil combination shows yields a maximum achievable 3 dB noise-matched bandwidth at 1.3 MHz for a noise-matching factor N of 386. Using this noise-matching factor, the resonant frequency between the detector coil and the noise-matched amplifier input is around 317 kHz (Eqn. 3.32) in the absence of any parasitic impedances. Figure 3.5 shows system noise figure scaling with other values of the noise-matching factor, N, for the ADA4817 amplifier.

3.3.1 MPI preamplifier circuit design

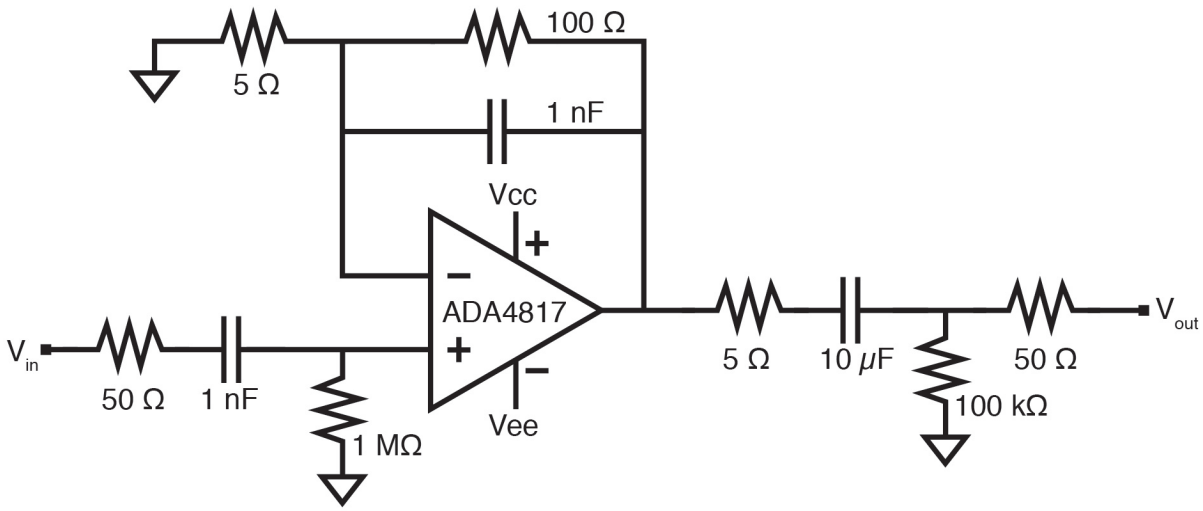

Figure 3.6: A noninverting amplifier configuration is used for the first stage of the MPI preamplifier. The serial input resistance of 50 Ω is used to keep the OPA stable when paralleled together with other devices.

To realize the noise-matched MPI detector system, we designed a two-stage preamplifier

circuit using the ADA4817 OPA. The first stage is comprised of 24 parallel noninverting-input amplifiers and the second stage is a summing amplifier that takes as input all of the output signals from the first stage.

A noninverting input amplifier configuration was chosen for the first stage because of its high input impedance, which provides proper loading to the detector coil inductance (unless, as previously mentioned, the detector coil resonates with the preamplifier input capacitance). The amplifier gain was designed to be 20, and the gain-setting resistors on the negative input terminal were chosen at low resistance values to minimize thermal noise contribution to each OPA circuit. A serial input resistance was used to keep the OPA circuit stable and avoid crosstalk with other parallel amplifier devices. This 50 Ω serial input resistor has approximately 0.9 nV/$\sqrt{\text{Hz}}$ voltage noise, which increases the effective $\bar{e}_n$ of each OPA circuit by 0.1 nV/$\sqrt{\text{Hz}}$.

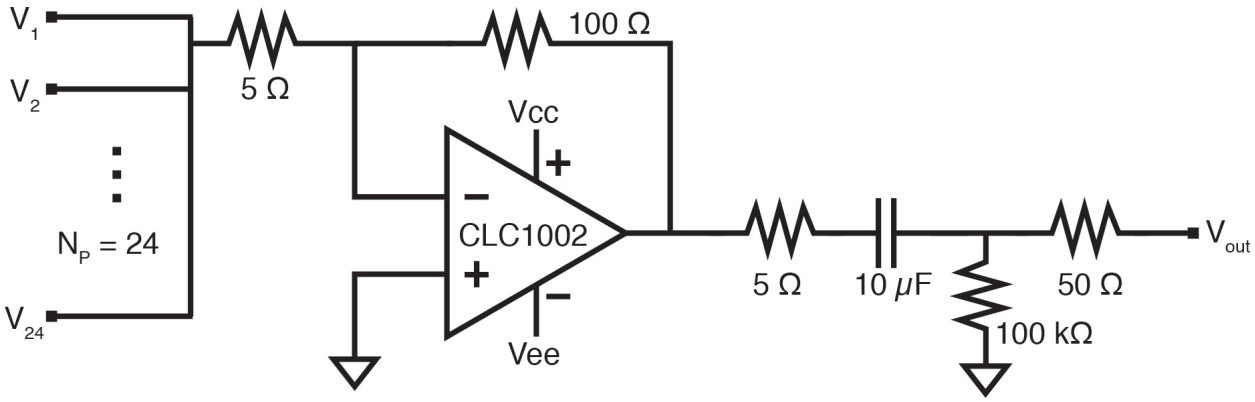

Figure 3.7: Inverting summing amplifier configuration for the second stage of the MPI preamplifier.

The outputs of the 24 OPA amplifier circuits from the first stage were summed in parallel using a summing amplifier circuit with a second gain stage. For this summing amplifier, we chose the exceptionally-low $\bar{e}_n$ CLC1002 BJT operational amplifier (Exar Corp., Fremont, CA), at 0.6 nV/$\sqrt{\text{Hz}}$. The gain of the second amplifier stage also depends on the output impedance of the first stage and can be calculated as $100\Omega/\left(5\Omega + 55\Omega/24\right) = 13.7$. Hence the total gain of the MPI preamplifier device is calculated to be 274.

Accounting for noise in the serial input resistors and the gain-setting resistors, the overall input-referred voltage noise of this preamplifier is calculated to be 0.84 nV/$\sqrt{\text{Hz}}$.

3.3.2 MPI preamplifier printed circuit board layout

We implemented the MPI preamplifier circuit design as a custom printed circuit board and designed the board layout schematic using Diptrace software (Novarm Ltd.). The board design uses five layers: the top and bottom layers are respectively used for input and out

signals and the middle layers are used as a ground plane and power planes. A schematic of the signal planes and ground plane is shown in Figure 3.8.

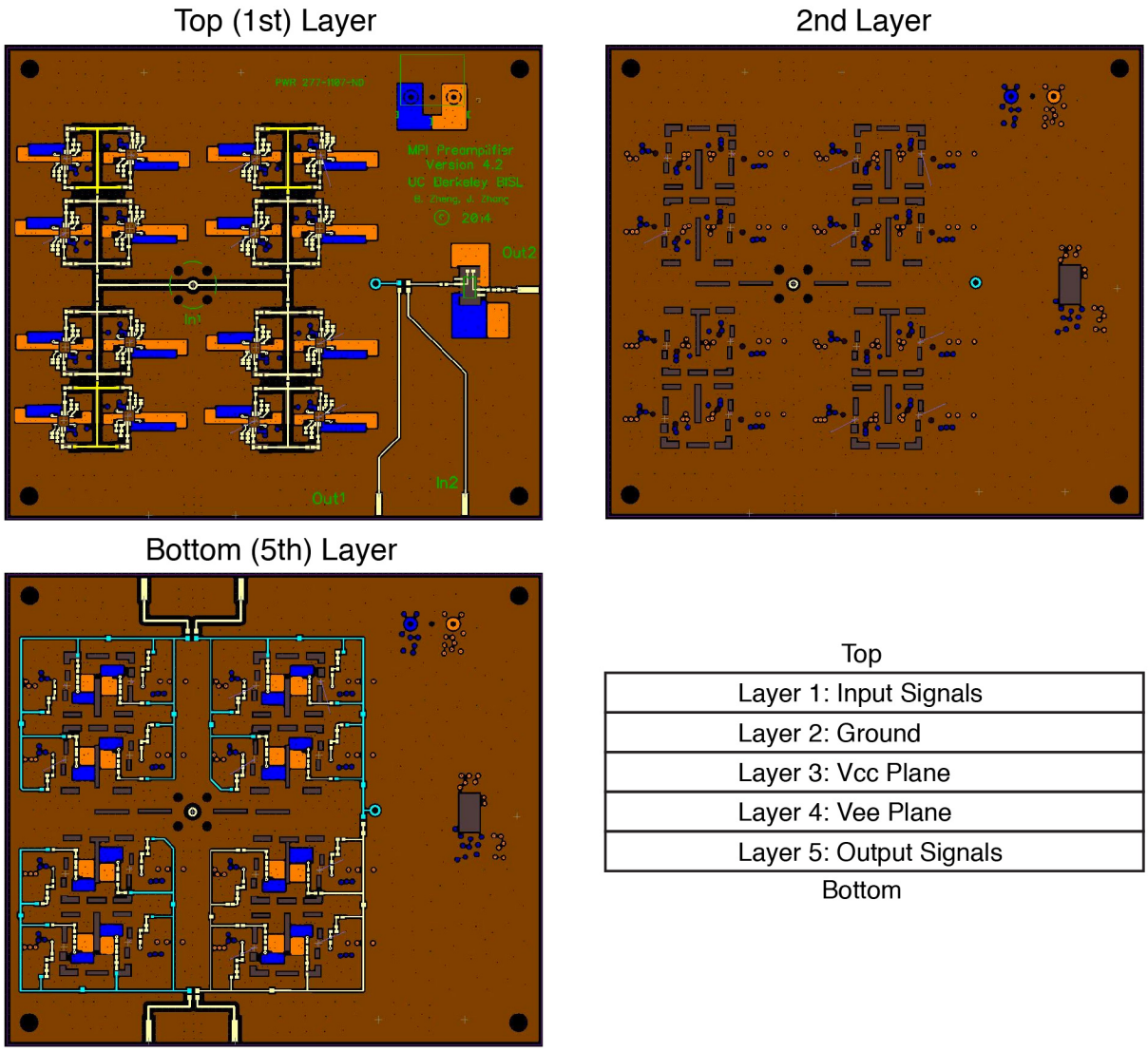

Figure 3.8: Printed circuit board layout design for the MPI preamplifier. The preamplifier circuit board uses five layers, with the top and bottom layers being used for input and output signals, respectively. The input to the PC board is a BNC coaxial connector from the detector coil. In this schematic, ground planes are colored brown, Vcc nodes are orange, and Vee nodes are blue.

One goal in the layout of the preamplifier circuit board is to reduce circuit input capacitance that can arise from parasitic stray board capacitance. To minimize input trace capacitance to the board, we sought to remove copper planes from the ground and power planes underneath the input traces while maintaining circuit stability [68].

To power the MPI preamplifier, we created a custom power supply board for Vcc and Vee using low-dropout voltage regulators from Texas Instruments (LM1085 and LM7905) to reduce power supply noise. The power supply board maintained rail voltages at ±5 V. Bypass capacitors with capacitance values 0.1, 1, and 10 µF were used to decouple noise at the positive and negative supply pins at each OPA device.

To facilitate preamplifier circuit board debugging, the first amplifier gain stage is grouped into four sections that can be tested for gain, noise, and distortion independently using dedicated debugging output connectors.

3.3.3 MPI preamplifier input-matching transformer

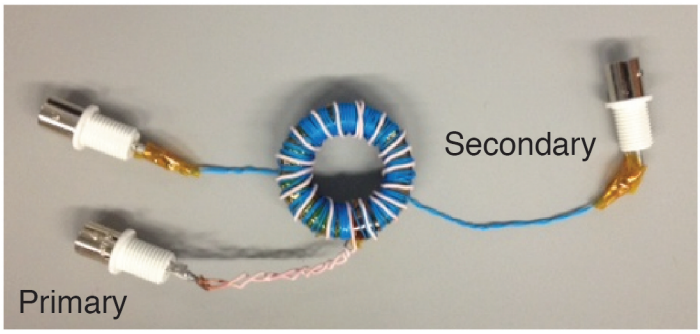

Figure 3.9: A 1:4.3 turns ratio input transformer used for noise matching with the MPI preamplifier.

To enable further noise matching to the detector coil resistance in the preclinical MPI scanner, we constructed a custom input transformer that can be connected serially to the input of the preamplifier. The matching transformer is constructed using a toroidal core using Type 75 material from Fair-rite Products Corp, (Wallkill, NY), which has a high permeability with μ_r of 5000. The primary and secondary windings are constructed using 30 AWG wire using a turns ratio of 4:3, with respective inductances of 2.5 mH and 40 mH. The use of this 1:4.3 transfomer with the 24 parallel-connected ADA4817 amplifiers gives an effective noise-matching factor N of 444, which is close to the calculated optimal value of 386.

The primary winding resistance in the transformer was 0.5 Ω, which has $\bar{e}_n$ of 90 pV/$\sqrt{\text{Hz}}$ and thus does not significantly degrade noise figure in the detector system. The design of noise-matching transformers is well characterized [60] and the transformer presented here can be further optimized by using different winding designs and thicker windings.

3.4 MPI Preamplifier Results

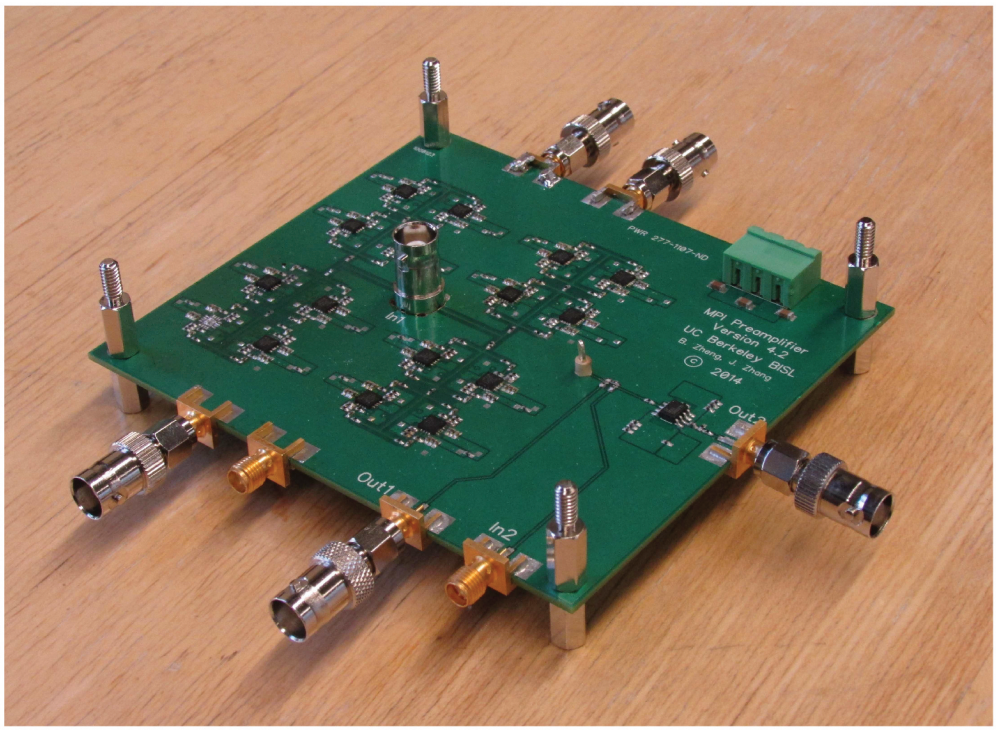

Figure 3.10: Constructed MPI preamplifier circuit board. The MPI preamplifier uses 24 parallel ADA4817 amplifiers in the first stage and a summing amplifier constructed using a CLC1002 OPA in the second stage. The amplifier achieves a gain of 265 and input-referred voltage noise of 1.06 $\mathrm{nV}/\sqrt{\mathrm{Hz}}$.

The MPI preamplifier circuit board was manufactured by Bay Area Circuits, Inc. (Fremont, CA) and is 4 by 4 inches in size. A photograph of the constructed preamplifier is shown in Figure 3.10. In the following sections, we discuss the noise performance of the custom MPI preamplifier and demonstrate its use and imaging performance in the preclinical MPI scanner.

3.4.1 MPI preamplifier noise specifications

Calculated and measured noise and input impedance characteristics for the MPI preamplifier are shown in Table 3.2. Gain and input-referred voltage noise for the preamplifier match well with expected values at 265 and 1.06 $\mathrm{nV}/\sqrt{\mathrm{Hz}}$, respectively. We note that not all operational amplifier circuits on the constructed board performed as expected, which we attribute to occasional device breakdown during soldering. We also measured second and third-order

	Preamp		Preamp and Transformer	
	Calculated	Measured	Calculated	Measured
Gain	274	265	1178	1150
$\bar{e}_n$ (nV/$\sqrt{\text{Hz}}$)	0.84	1.06	0.25	0.28
HD2 (dB)	-	79	-	>60
HD3 (dB)	-	>90	-	>90
Cin (pF)	31.2	63.2	577	1300

Table 3.2: Calculated and measured specifications for MPI preamplifier with and without the use of an input-matching transformer. 2nd and 3rd order distortion was measured using an input sinusoid with 1 mV_{rms} amplitude and 40 kHz frequency.

harmonic distortion of a 1 mV_{rms}, 40 kHz sinusoid signal. HD2 and HD3 were found to be around 80 dB, which is comparable to that achieved by the commercial SR560 preamplifier and is satisfactory for MPI applications. However, the total input capacitance was found to be around twice the expected input capacitance of 24 parallel ADA4817 devices alone, suggesting that parasitic capacitance in the circuit board amounted to around 32 pF. This undesirable board capacitance will reduce the expected resonant frequency of the detector coil by a factor of $\sqrt{2}$.

The addition of a 1:4.3 input transformer in the detector system increases the total signal gain to 1150, which matches the expected gain. The transformer also reduces the effective amplifier voltage noise down to around 280 pV/$\sqrt{\text{Hz}}$, which is equivalent to the thermal noise in a 5 Ω resistor. Distortion levels in the system remain acceptable for MPI use at 60 and 90 dB for HD2 and HD3, provided that an aggressive notch filter at the fundamental drive field frequency (Chapter 2) is needed to attenuate direct feedthrough interference to compress the system dynamic range. Finally, the input capacitance of the transformer-coupled preamplifier system is increased by a factor of 4.3^2 to 1.3 nF, as expected. Using a 500 µH detector coil, the coil resonance frequency is then around 200 kHz.

To test the noise figure of the custom MPI preamplifier system, we used the system to measure the thermal noise in resistors ranging from 0.1 Ω to 1 kΩ. In these experiments, a resistor was connected in series with the preamplifier and the total system voltage noise density from 1 to 100 kHz was directly measured using a commercial audio analyzer (SR1, Stanford Research Systems). The measurement results for the preamplifier and the transformer-coupled preamplifier are shown in Figure 3.11. In the plot, we show the theoretical voltage noise contributions from resistor thermal noise, amplifier voltage noise, and the total theoretical voltage noise from both. Our experimental voltage noise measurements match well with theoretical predictions, and the total noise voltage is dominated by preamplifier $\bar{e}_n$ at low source resistances and by resistive noise for high source resistance values. For the MPI preamplifier alone, the apparent crossover point between amplifier noise and resistor noise occurs at around 70-80Ω. For the transformer-coupled preamplifier, this transition point

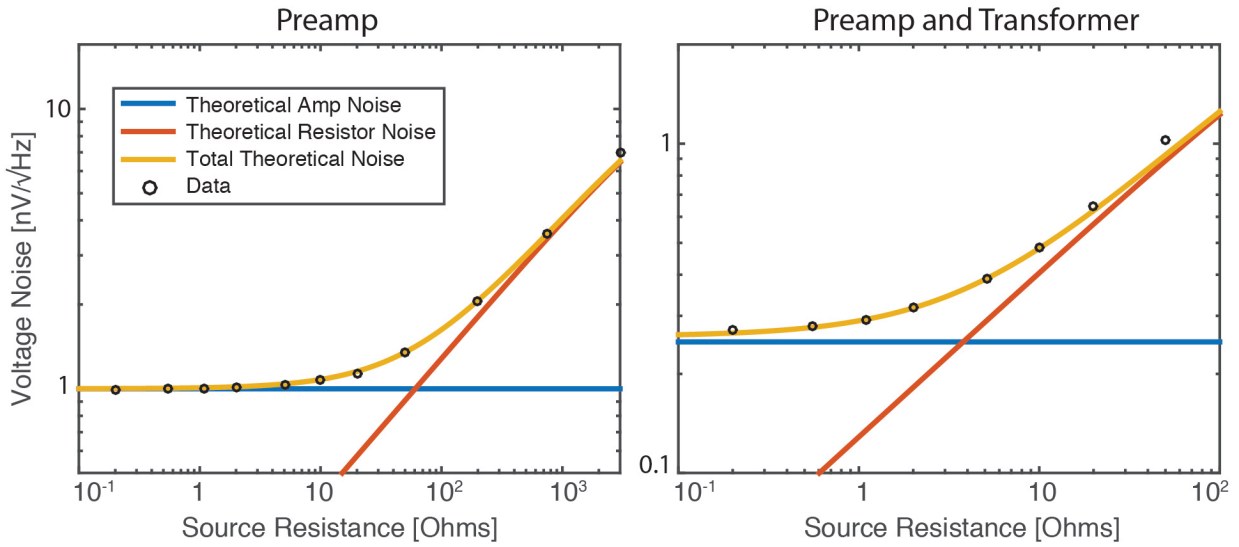

Figure 3.11: MPI preamplifier measurements of thermal noise in resistors. Theoretical resistor noise, amplifier voltage noise, and total input-referred noise are shown for varying source resistances for the custom MPI preamplifier alone and the preamplifier with transformer coupling. Total input-referred noise measurements for varying resistor values match closely with theoretical predictions.

occurs at around 4-5 Ω, which would enable 3 dB noise matching to the preclinical MPI detector coil as expected.

3.4.2 Phantom MPI imaging comparison between custom MPI preamplifier and SR560

To test the imaging performance of the custom preamplifier, we performed MPI imaging in a preclinical MPI scanner using a custom-built sensitivity imaging phantom (Fig. 3.12). The imaging phantom was machined from an extruded acrylic rod with 3.5 cm diameter. Six holes with 2 mm diameter and 7 mm depth were drilled into the phantom and arranged equidistantly in a ring configuration. 10 µL of diluted SPIO tracer (Nanomag-MIP, Micromod, Rostock, Germany) with iron content ranging from 2.1 to 12.7 µg was pipetted into the phantom and sealed before MPI imaging.

The MPI scanner used was a custom 7 T/m gradient, field-free point small-animal MPI scanner [8] operating at 20.05 kHz drive field frequency and 40 mTpp drive field amplitude. The MPI scanner detector coil had an inductance of 470 µH and resistance of 5 Ω and was wound in a gradiometer configuration to suppress direct feedthrough from the drive field coil. A 4-stage LC notch filter at 20.05 kHz was connected in series with the detector coil to further reduce direct feedthrough interference at the fundamental drive field frequency.

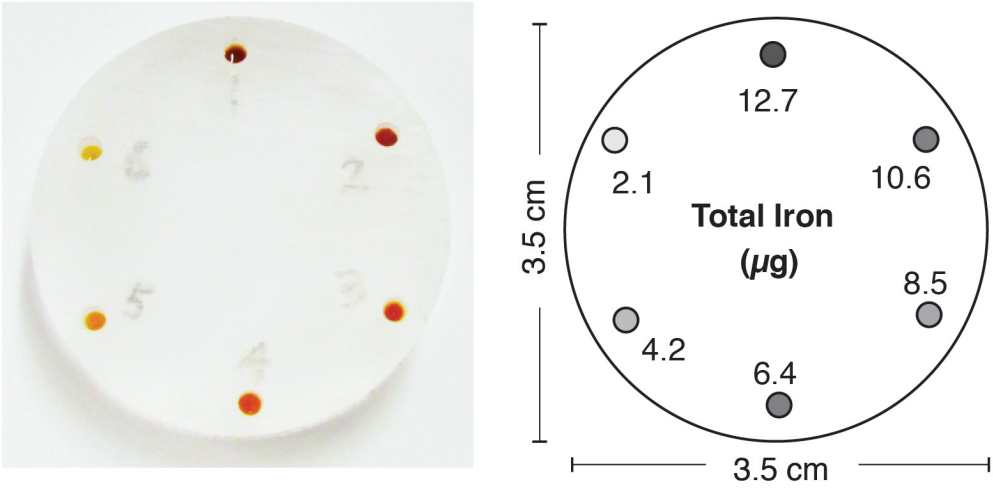

Figure 3.12: A ring-shaped MPI imaging phantom containing increasing amounts of SPIO tracer used for testing preamplifier performance. The phantom, which is 3.5 cm in diameter, was machined from extruded acrylic. 10 µL of diluted SPIO tracer with iron content ranging from 2.1 to 12.7 µg was pipetted into six holes with 2 mm diameter and 7 mm depth, arranged in a ring configuration around the phantom.

MPI imaging acquisitions used an imaging field-of-view of 5 cm × 3.75 cm × 5 cm and a total scan time of 5 minutes. All MPI images were reconstructed using an x-space imaging reconstruction algorithm [2, 39] and were not postprocessed after image reconstruction.

We used two preamplifiers for MPI imaging. The first preamplifier used is a SR560 commercial preamplifier from Stanford Research Systems with a gain of 200. At this gain, the preamplifier has an equivalent input noise voltage of 4 nV/$\sqrt{\text{Hz}}$. The second preamplifier used is the custom tranformer-coupled MPI preamplifier described in this Chapter, with gain of 1150 and equivalent input noise voltage of 0.28 nV/$\sqrt{\text{Hz}}$.

MPI imaging results of the sensitivity imaging phantom are shown in Fig. 3.13 for the custom MPI preamplifier and the SR560. Images acquired using the custom MPI preamplifier show high signal-noise ratio and are able to visualize all samples in the imaging volume. In contrast, the images acquired using the SR560 preamplifier show high image noise, especially at 40% of full image scale. Only 4-5 tracer samples are visually detectable in MPI images acquired using the SR560 preamplifier.

Image noise statistics from the MPI image acquisitions using the custom MPI preamplifier and the SR560 are shown in Fig. 3.14. To determine image noise, pixel values in the reconstructed MPI images were determined using regions of interest that contain no SPIO tracer. These image noise signals are then divided by the total detector system gain and normalized by the MPI bandwidth to determine equivalent input voltage noise density in nV/$\sqrt{\text{Hz}}$. Using

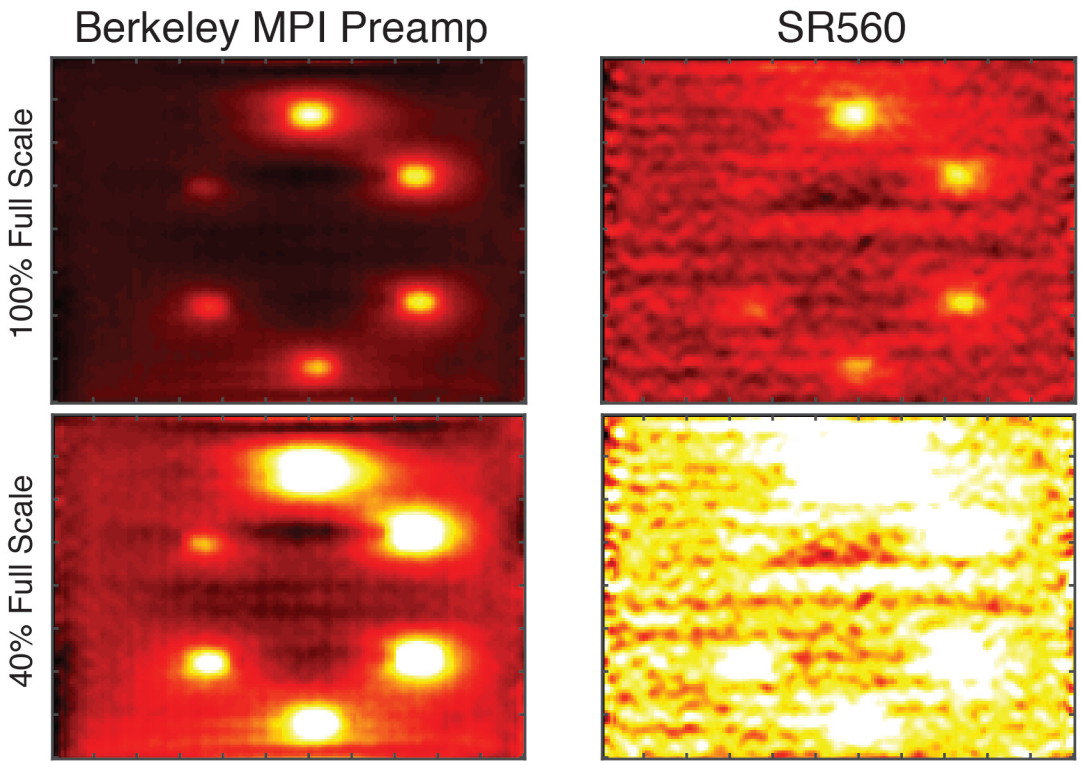

Figure 3.13: Comparison of MPI imaging performance using the custom transformer-coupled MPI preamplifier and a commercial SR560 preamplifier. Images show the ability of the custom transformer-coupled MPI preamplifier to quantitatively detect all samples in the imaging phantom with high SNR. MPI images acquired in the same acquisition time using the SR560 preamplifier show lower SNR, with the detection sensitivity limit around 4.2 µg of iron. MPI imaging parameters: 5 cm × 3.75 cm × 5 cm imaging FOV, 5 minute scan time each.

this method, we determined that the input-referred noise for the transformer-coupled MPI preamplifier to be 0.41 nV/$\sqrt{\text{Hz}}$ and 4.4 nV/$\sqrt{\text{Hz}}$ for the SR560. Hence, the use of a custom noise-matched preamplifier enabled an 11-fold improvement in the SNR of MPI images.

The measured noise value for the custom MPI preamplifer matches well with theory, which predicts that, as the detector bandwidth is below the voltage noise-current noise transition frequency (Eqn. 3.38), the total input-referred noise for the custom transformer-coupled MPI preamplifier is $\sqrt{(0.28 \times 10^{-9})^2 + 4k_bTR}$, which is 0.40 nV/$\sqrt{\text{Hz}}$. Notably, because the thermal noise in a 5 Ω detector coil is 0.29 nV/$\sqrt{\text{Hz}}$, this detector system has therefore been noise-matched to below 3 dB.

Finally, we calculated the sensitivity limit of the FFP MPI scanner using these preamplifiers from the acquired MPI images. To do this, we divided the MPI image signal for the highest-concentration sample over the standard deviation of the image noise. These re-

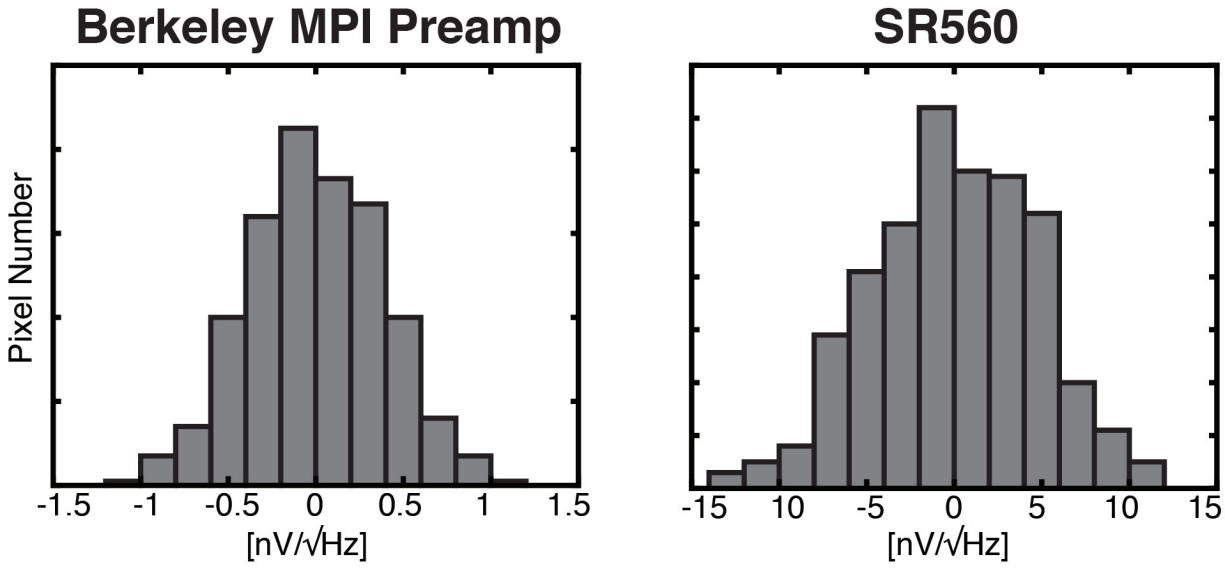

Figure 3.14: Image noise statistics from MPI data acquired using the custom MPI preamplifier and SR560. To calculate image noise, pixel values in MPI images were determined using regions of interest (ROIs) that contain no SPIO tracer. The MPI image-derived noise standard deviation for the custom transformer-coupled MPI preamplifier was determined to be 0.41 nV/$\sqrt{\text{Hz}}$. Image noise for the SR560 preamplifier was determined to be 4.4 nV/$\sqrt{\text{Hz}}$.

sults showed that the expected sensitivity limit, where the image SNR is equal to 1, for the SR560 is around 450 ng of iron tracer in a voxel. For the custom transformer-coupled MPI preamplifier, the sensitivity limit in this MPI scanner is found to be as low as 50 ng of iron tracer.

3.5 Discussion

In this Chapter, we investigated the sources of electronic noise generation in Magnetic Particle Imaging scanners, discussed three options for optimal MPI noise-matching and their tradeoffs with system bandwidth, and designed, constructed, and tested a custom transformer-coupled preamplifier. Using this custom preamplifier, we demonstrated 3 dB noise matching to the MPI detector coil and an 11-fold improvement in SNR performance for MPI imaging over a commercial SR560 preamplifier.

Our results here suggest that the detection sensitivity for the field-free point preclinical MPI scanner is as low as 50 ng Fe. This sensitivity limit can be further improved significantly by the use of field-free line, projection-format MPI scanners [44]. An existing FFL MPI imager already demonstrated higher sensitivity at 5 ng detection limit in a voxel (see Chapter 4) due to the more sensitive projection imaging format of FFL scanners. Hence,

high gradient-strength FFL scanners may be most appropriate to further improve detection sensitivity, imaging speed, and spatial resolution.

To enable the highest sensitivity for MPI scanners in the clinic, it remains important to investigate methods of further reducing electronic noise in the detector coil and preamplifiers, such that the dominant noise source in the system arises from patient thermal noise. In this work, we have only address methods of matching voltage and current noise in the preamplifier to the detector coil, but have not addressed methods to reduce thermal noise in the detector coil itself. We currently foresee two potential methods of improving the detector thermal noise. First, the use of cryogenically cooled detector coils would decrease the thermal noise variance of the detector coil linearly with temperature. As an example, a liquid nitrogen-cooled detector coil would reduce the thermal detector noise variance by approximately a factor of 4, for a potential SNR improvement of 2. Second, the amount of total copper used in the construction of the detector coil can be increased to reduce the coil resistance. As an example, keeping the same number of turns in a detector coil but increasing the coil thickness by a factor of 4 results in a decrease in coil resistance, and thereby the coil noise variance, also by roughly a factor of 4. However, this method may be ultimately limited by tradeoffs in the total bore space available in the MPI scanner. Ultimately, as MPI scanner designs become more sophisticated, a combination of these and other approaches may be needed to enable patient-noise dominance for clinical MPI scanners.

Chapter 4

Magnetic Particle Imaging tracks the long-term fate of *in vivo* neural cell implants with high image contrast

4.1 Introduction

In Chapters 2 and 3, we described our efforts to improve the detection sensitivity of Magnetic Particle Imaging scanners by using engineering methods to attenuate the SNR-quenching drive field feedthrough interference and by designing an optimally noise-matched MPI detector preamplifier. These efforts have resulted in significantly improved detection sensitivity and image SNR in our preclinical scanners. In the following two Chapters, I describe the first use of these MPI scanners for preclinical cell tracking applications. I first describe in Chapter 4 an application to quantitatively track the *in vivo* fate of neural progenitor cells in rodent models, showing the ability to detect SPIO labeled stem cells for more than 87 days in the rodent brain. This experiment was the result of a fruitful collaboration with Professor David Schaffer's research group at UC Berkeley. In this study, I designed the experiments along with the principal investigators, conducted MPI scanner operation and imaging studies, prepared the figures, and wrote a manuscript for publication.

Magnetic Particle Imaging [1, 42] directly images the intense magnetization of SPIOs with high image sensitivity and quantitativeness, making it an ideal modality for imaging tagged cells administered *in vivo*. The voltage signals generated in MPI are linearly proportional to the number of SPIOs at the instantaneous FFL location, enabling quantification of SPIO number [39]. The MPI induction signal is detectable with even a miniscule mass of tracer (5 ng Fe/voxel in our projection MPI scanner) because the SPIO magnetization saturates to 600 mT. By comparison, the nuclear paramagnetism of water in a 7 T MRI scanner is only 27 nT. That is, MPI images a magnetization that is 22 million times more intense than we image routinely in high-field MRI. Moreover, biological tissue does not generate or attenuate the low-frequency magnetic fields used in MPI (10 kHz to 1 MHz) [69], giving the technique

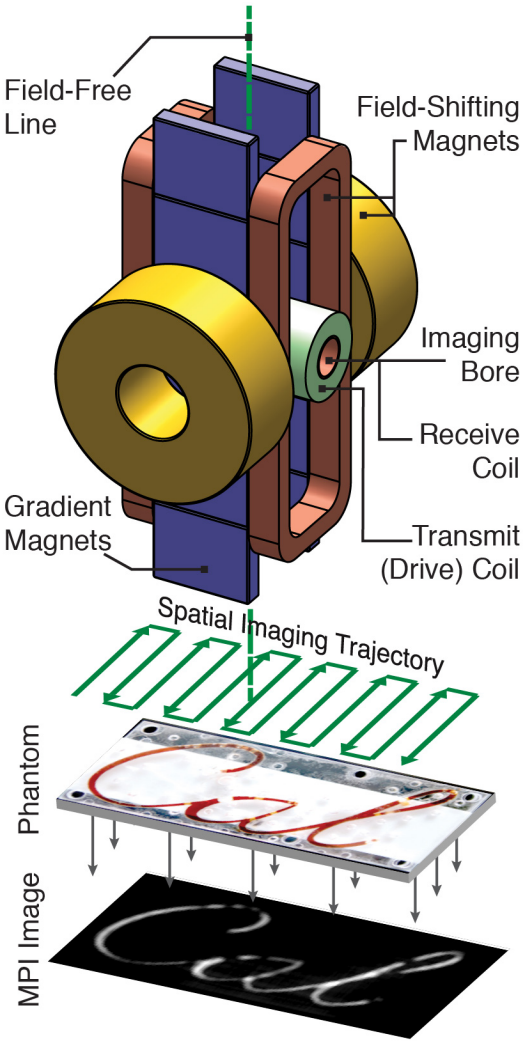

Figure 4.1: Diagram and characteristics of a small-animal projection MPI scanner. Three superposed magnets (field-shifting magnets, gradient magnets, and drive coil) produce and translate a magnetic field-free line (FFL) across an imaging volume. As the FFL is rastered across a distribution of superparamagnetic iron oxide (SPIO) particles using a spatial imaging trajectory, the particle ensemble magnetization changes in magnitude and orientation in response. The changing particle magnetization is detected via a detector coil and reconstructed to form a MPI image.

ideal contrast independent of source depth. The combination of these characteristics enables MPI to be uniquely suitable for high-contrast, radiation-free cell tracking *in vivo* [70]. A comparison of imaging characteristics of MPI and existing technologies is shown in Table 4.1.

Imaging Modality	Spatial Resolution	Acquisition Time	Detection Limit: Cells	Labeling Strategy	Notes
Bioluminescence and Fluorescent Imaging	2-20 mm depending on depth	seconds	$\sim 10^3$	reporter gene	small animals only, low resolution, not quantitative
Nuclear Medicine: SPECT and PET	1-2 mm (preclinical), 4-12 mm (clinical)	minutes	10^4 - 10^5	reporter gene, incubation with radiotracer	radioactive tracer required, quantitative
Magnetic Resonance Imaging	100-500 µm (preclinical), 0.5-5 mm (clinical)	minutes to hours	$\sim 10^4$	direct labeling with nanoparticles	expensive and complicated, not quantitative
Magnetic Particle Imaging	100-500 µm (preclinical expected)	seconds - minutes	10^1 - 10^2	direct labeling with nanoparticles	quantitative

Table 4.1: Comparison of imaging technologies for cell therapy tracking. Adapted from [25].

To test MPI for tracking cells *in vivo*, we built two small animal MPI scanners, the construction of which are previously described and analyzed [71, 72, 8]. These include a projection-format FFL scanner with 2.35 × 2.35 T/m gradient, which achieves roughly 4 mm × 8 mm resolution along and orthogonal to the axis of the imaging bore, respectively, using undiluted Resovist tracer [72]. The FFL scanners projection-mode image acquisition enables fast scanning times on the order of seconds for a small animal-sized imaging volume. We also report the use of a field-free point (FFP) MPI scanner with a 7 × 3.5 × 3.5 T/m gradient, which enables roughly 2 mm × 4 mm × 2 mm resolution using Resovist and higher resolution using MPI-tailored SPIOs [8]. An example MPI image of labeled cells scanned using the FFP scanner is shown in Fig. 4.2. Both scanners use our groups recent advances in MPI reconstruction that are necessary and sufficient for linear quantification [39]. We also note that the experimental detection sensitivity of the FFL scanner is, at roughly 5 ng Fe / voxel, 15-fold better than the FFP scanner, as expected due to a larger voxel volume. Based on the high sensitivity and faster scan times of the FFL scanner, we conducted all

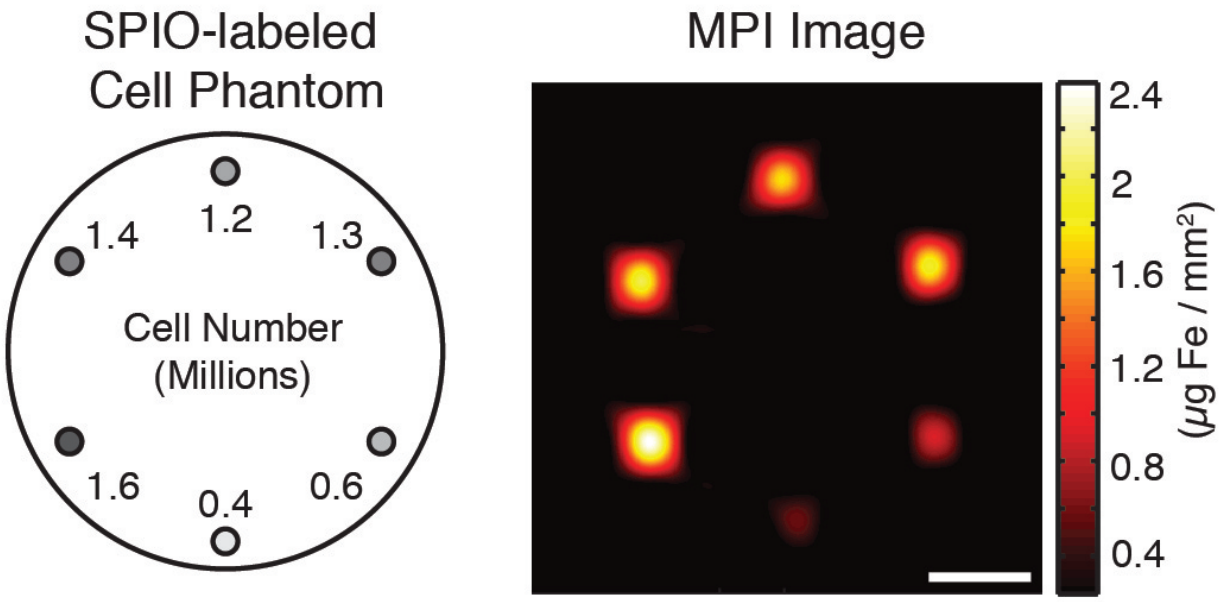

Figure 4.2: FFP imaging of an acrylic phantom filled with six populations of SPIO-labeled cells. The MPI signal from cell populations (ranging from 4×10^5 to 1.6×10^6 in number) corresponds linearly to iron oxide tracer concentration, enabling quantitative imaging. Imaging parameters: 3.5 min acquisition on a 7 T/m 3D MPI scanner, 5 cm $\times$ 4.5 cm $\times$ 3 cm FOV. Scale bar: 1 cm.

MPI imaging in this study, with the exception of the image shown in Fig. 4.2, using the FFL scanner.

4.2 Methods

4.2.1 Magnetic labeling of differentiated human embryonic stem cells (hESCs) and determination of labeling efficiency

H1 hESCs (WiCell, Madison, WI) were cultured on Matrigel-coated cell culture plates (BD, Franklin Lakes, NJ) in X-Vivo medium (Lonza, Norwalk, CT) supplemented with 80 ng/mL FGF-2 (PeproTech, Rocky Hill, NJ) and 0.5 ng/mL TGF-β1 (R&D Systems, Minneapolis, MN), as described previously [73].

For embryoid body (EB) mediated differentiation, H1 colonies were enzymatically isolated from Matrigel-coated plates by 5-minute treatment with 1 mg/mL collagenase type IV (Worthington Biochemical Corporation, Lakewood, NJ) and partially dissociated by gentle pipetting. The resulting cell clusters were resuspended in hESC culture medium, X-Vivo without FGF-2 and TGF-β1, and transferred to ultra-low-attachment plates (Corning In-

corporated, NY) for cell aggregation for 4 days. The generated embryoid bodies were then seeded on Matrigel-coated plates and allowed to differentiate for an additional 10-12 days in adherent conditions in X-Vivo medium.

For cell labeling, Resovist superparamagnetic iron oxide particles (Bayer Schering Pharma AG, Leverkusen, Germany; 0.5 mmol Fe/mL) at a concentration of 200 µg Fe/mL were incubated with 6 µg/mL protamine sulfate (American Pharmaceuticals Partner, Schaumburg, IL) in serum free X-Vivo medium (Lonza, Walkersville, MD) and allowed to form complexes on a shaker for 6 hr. The solution containing Fe-Pro complexes was added to differentiating hESCs in adherent culture condition. The cultures were incubated with Fe-Pro complexes overnight. Cultures after labeling were washed with 10 U/mL heparin (Sigma) in PBS three times to dissolve remaining surface-bound Fe-Pro complexes.

For assessment of labeling efficiency, Prussian blue cellular staining was performed by incubating cells, fixed with 4% paraformaldehyde, in a mixture of 4% potassium ferrocyanide and 3.7% HCl (Iron Stain Kit, Sigma) for 20 minutes to visualize intracellular iron particles. Cells were counted manually under a microscope to determine average cell labeling efficiency. Labeling efficiency was found to be 71% ± 8%. A hemocytometer was used to determine all cell numbers.

4.2.2 MPI image acquisition

Two custom-built MPI systems were used in this study: 1) a projection MPI scanner with 2.35 T/m/μ_0 field gradient [72], and 2) a 3D MPI scanner with 7 T/m/μ_0 [8]. Both systems used a drive field frequency of 20.05 kHz and excitation strength of 40 mTpp/μ_0, with 30 second total scan time for projection MPI scanner and 3 minute scan time for 3D MPI scanner unless otherwise specified. MPI images were reconstructed using an x-space MPI reconstruction [2, 42, 39], followed by light Wiener deconvolution using a measured point-spread function. All MPI images were windowed at 10% full scale. All data acquisition, control, and data processing were performed with MATLAB (Mathworks). All MPI imaging was conducted using the projection FFL scanner with the exception of the cell phantom imaging study shown in Figure 4.2.

4.2.3 Determination of linearity of MPI signal with cell number

To investigate the linearity of the MPI signal with imaged cell number, we imaged 9 populations of Resovist-labeled hESC-derived cell pellets containing 10×10^3, 25×10^3, 50×10^3, 100×10^3, 200×10^3, 400×10^3, 600×10^3, 800×10^3, and $1,000 \times 10^3$ cells using a projection-format MPI scanner as described above. Following image reconstruction, the maximum signal intensity for each MPI image was determined and the Pearson correlation coefficient was determined between normalized MPI signal and imaged cell number. Subsequent linear regression on the data and 95% confidence intervals for the slope of the regression line were determined.

4.2.4 Intracellular Iron Measurement

Average intracellular iron was determined using induction-coupled plasma optical emission spectroscopy (Optima 5300 DV, PerkinElmer, Waltham, MA) at the UC Berkeley Induction-Coupled Plasma Spectroscopy Facility on a population of 1×10^6 SPIO-labeled hESC-derived cells. Prior to measurement, cells suspended in 0.2 mL PBS solution were digested using a 1.8 mL mixture of 70% nitric acid and 30% hydrogen peroxide and diluted to 60 mL using deionized water. ICP analysis was performed in triplicate to determine intracellular iron as mean ± SD in picograms of iron per cell. Intracellular iron was also measured using MPI. A calibration curve for volume MPI signal per picogram iron was first generated using 0, 0.3, and 1.0 µL Resovist tracer. Subsequently, we performed MPI imaging of 1×10^6 labeled cells (n = 4 each) and determined intracellular iron using the calibration curve as mean ± SD in picograms of iron per cell. To evaluate the similarity between MPI and ICP intracellular iron measurements, we performed an unpaired two-sample T-test for mean intracellular iron, with significance level set to 0.05.

4.2.5 *In vivo* stem cell implantation and MPI imaging

All animal procedures were conducted according to the National Research Councils Guide for the Care and Use of Laboratory Animals and approved by UC Berkeleys Animal Care and Use Committee. Immunocompetent 8-week old female Fischer 344 rats weighing 145 g were used for *in vivo* imaging. All animals were fed on an ad libitum diet of Teklad Rodent Diet 2018 (Harlan, Indianapolis, IL).

For *in vivo* MPI cell tracking experiments, hESCs were differentiated to neural progenitor cell by dual inhibition of SMAD signaling [74] using SB431542 (10 µM) and LDN-193189 (1 µM) in adherent conditions for 12 days. The generated NPCs were labeled with Resovist SPIO particles as previously described here. The cell suspension contained approximately 100×10^3 viable cells/µL.

Animals were anesthetized with an intraperitoneal injection of ketamine (100 mg/kg rat weight) and xylazine (7.5 mg/kg), positioned into a stereotactic frame. For two animals, a total of 500×10^3 SPIO-labeled cells in 5 µL were injected at the following stereotaxic coordinates: 1.0 mm AP (relative to Bregma), 2.0 mm lateral, 2.5 mm ventral (from dura) over 10 min using a Hamilton syringe at a rate of 0.5 µL/min. For Animal 3, the coordinates were adjusted to 1.0 mm AP (relative to Bregma), 1.5 mm lateral, and 3.5 mm ventral (from dura) to facilitate graft translocation through the lateral brain ventricle. A control animal was injected using 0.15 µL of Resovist tracer diluted in 4.85 µL PBS using the same stereotactic coordinates as Animals 1-2. The needle was left in place for 3 min after injection and slowly removed. Animals were allowed to recover from surgery for up to ten days before MPI imaging, with 7 daily injections of cyclosporine-A starting 1 day prior to implantation at a dose of 15 mg/kg body weight.

Animals were imaged using MPI at days 10, 24, 35, 45, 59, and 87 post-implantation. Animal 4 was imaged at days 4 and 14 instead of days 10 and 24 with all other time points

remaining the same. During *in vivo* MPI imaging, animals were induced into anesthesia using 2.5-3.0% isoflurane and maintained at 1.5% isoflurane at 2 L/min and placed in a custom-built animal bed in the MPI scanner. *In vivo* MPI scans were conducted on the projection MPI scanner using a 9.3 cm by 6 cm FOV with 30 second scan time.

For determination of *in vivo* SPIO clearance rates measured by MPI, a linear regression was performed on the logarithm of the time-varying volumetric MPI signal for each animal.

4.2.6 Postmortem MRI

Following sacrifice, intact brains were harvested and imaged on a 7T Bruker PharmaScan MRI scanner using a zero echo time pulse sequence. MR scans had total acquisition times of 20 minutes with 256^3 voxels and 100 µm^3 voxel size at 2.9 degree flip angles and 4 ms T_R. Anatomical MRI images were acquired with postmortem age-matched animals using a TurboRare pulse sequence with 10 minute acquisition and 384^2 voxels, with field of view at 7.5 cm by 4 cm and 2.5 second T_R.

4.2.7 Stereology and Immunohistological Analysis

Ex vivo brains were fixed in 4% paraformaldehyde overnight, then cryopreserved in 20% sucrose, frozen in dry ice, and cut in 40 µm coronal sections using a microtome. For immunohistochemistry, the following primary antibodies were used: mouse anti-nestin (1:500, R&D system), SC121 (1:400, Stem Cells Inc.), mouse anti-CD68 (1:100, Abcam). Sections were then incubated with fluorescent-labeled secondary antibodies Alexa 488 (green) or Alexa 568 (red)-labeled goat IgG; 1:1000, Life Technologies for 2 hr at room temperature and then mounted on glass slides. Brain slides were counter-stained with DAPI and imaged using a Zeiss Axio Observer A1 inverted microscope or a confocal microscope (LSM 710, Zeiss).

4.3 Results

4.3.1 Linear and Absolute Quantification

We first asked whether our MPI scanners could quantify SPIO-labeled cells *in vitro*. We modified an established MRI labeling protocol to label hESC-derived cells with Resovist SPIO tracer using a protamine sulfate transfection agent [29]. Both Resovist and protamine sulfate are approved for clinical use in the European Union and have no significant effect on cell proliferation, viability, and differentiation [29, 30, 31]. Using the projection-mode FFL MPI imager, we imaged nine labeled hESC-derived cell populations ranging from 1×10^4 to 1×10^6 cells. The normalized MPI signal was linear to the number of cells imaged ($R^2 > 0.994$, Fig. 4.3). In equivalent control cell populations without iron oxide labeling, no MPI signal was detected.

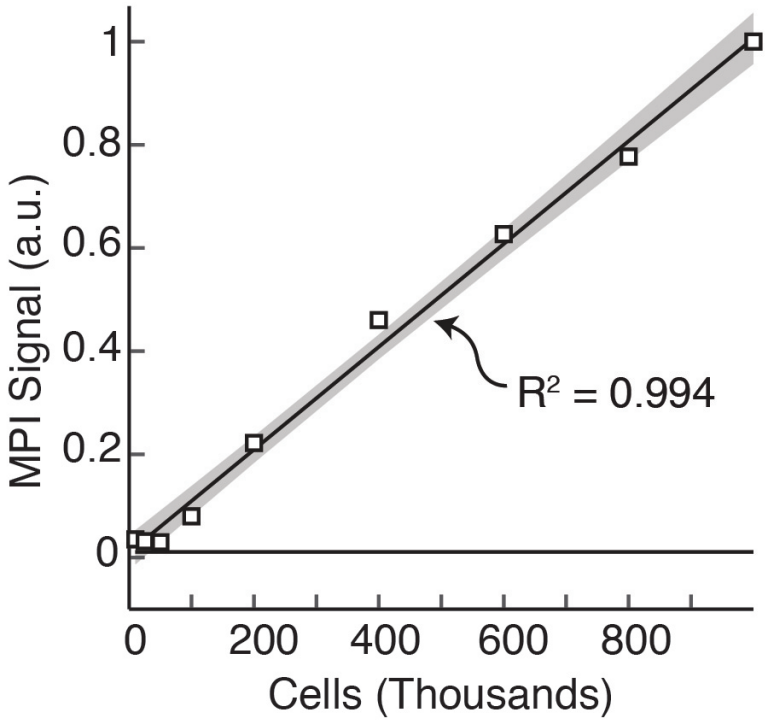

Figure 4.3: MPI images are highly linear with imaged cell number. Here we show a plot of MPI signal from 9 SPIO-labeled cell populations ranging from 1×10^4 to 1×10^6 cells, shown with MPI system noise floor. SPIO signal in MPI is linear with cell number ($R^2 = 0.994$, linear fit and 95% confidence bounds for fitted slope shown).

We further asked if MPI allows absolute quantification of iron oxide tracer. To determine this, we created a calibration curve using the MPI signal from measured volumes at 0, 0.3, and 1 µL of Resovist SPIO tracer. We then used the calibration curve to estimate average cellular SPIO content in MPI images of 1×10^6 labeled cells. These MPI cellular iron estimates, at 27.0±3.3 pg/cell, were within 99% agreement ($p = 0.923$) with standard but destructive Inductively Coupled Plasma (ICP) measurements at 26.8±0.3 pg Fe/cell (Fig. 4.4).

4.3.2 Sensitivity

We next investigated the sensitivity threshold of the prototype FFL MPI scanner for imaging labeled cells. We imaged 1×10^3 *in vitro* tagged cells in a pellet using a 20 second projection MPI scan and reconstructed the final MPI image using only the second and third harmonics of the drive field frequency. The reconstructed image showed a signal-noise ratio (SNR) greater than 5, corresponding to a 200-cell (5.4 ng Fe) detection limit (Fig. 4.5). This detection limit corresponds to 130 nM sensitivity for a measured voxel volume of 750 µL.

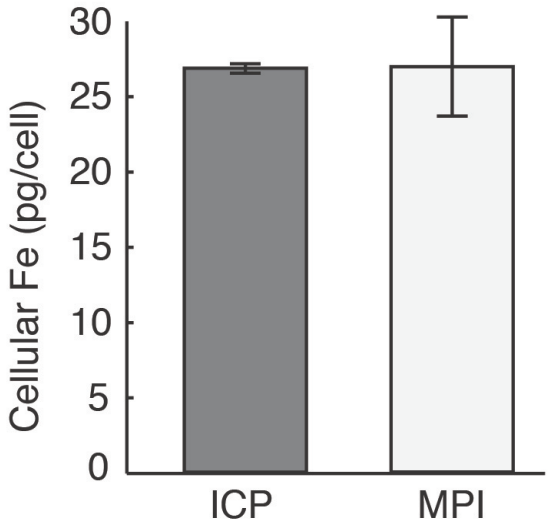

Figure 4.4: MPI estimates for average cellular iron content (27.0±3.3 pg/cell) correspond with ICP analysis (26.8±0.3 pg/cell), making MPI useful for nondestructive iron quantification. n=3 for ICP and n=4 for MPI; results are mean ± SD.

4.3.3 Resolution

To assess the effect of SPIO cell labeling on MPI resolution, we acquired and compared a MPI line scan of two point sources: (a) 8×10^6 labeled hESC-derived cells and (b) 20 µL of 10-fold diluted Resovist tracer (Fig. 4.6). The point sources were placed 3.5 cm apart on a 3D printed sample holder. The point sources were small (1.3 mm width) compared to the native resolution of the FFL system. The axial dimension of the point sources did not affect resolution analysis because the axis of each vial was placed parallel to the FFL during imaging. After a native MPI image was acquired, a line profile was generated across the center of the sample image to assess image blurring (Fig. 4.6, bottom panel). A comparison of the MPI signal widths of the two samples showed that the full-width-at-half-maximum (FWHM) resolution of diluted Resovist particles in solution was 5 mm, approximately 1.5-fold better than that of the labeled cells at 7.7 mm. The measured native resolution for Resovist at 5 mm matches well with theory [2], and approaches for improving the resolution are explored in Discussion.

4.3.4 Longitudinal Cell Tracking

Last, we tested MPI for tracking neural progenitor cells (NPCs) in vivo, which have previously shown promise as treatments for Parkinsons Disease, Huntingtons disease, epilepsy and ischemia [75]. It is known that NPCs survive, migrate, and show reconstructive properties when implanted in rodent models of forebrain ischemia [76, 77]. The high specificity of

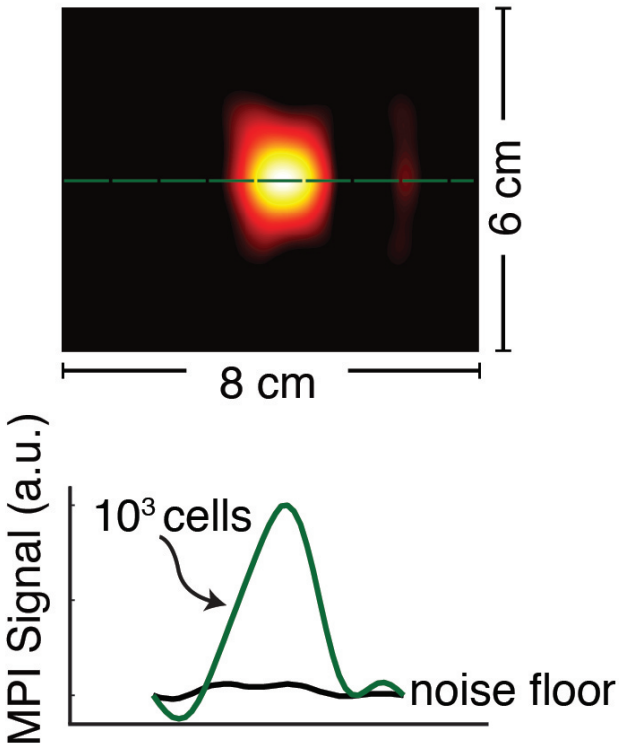

Figure 4.5: Detection threshold for MPI cell tracking in FFL scanner. Approximately 1,000 SPIO-labeled hESC-derived cells in a 100 µL *in vitro* suspension were imaged using MPI and compared to an empty scan. The signal-noise ratio of the image is estimated at above 5, giving a detection limit of approximately 200 cells. This represents the current detection sensitivity limit of our FFL MPI scanner, but the theoretical detection limit may be as low as a single cell. FOV: 6 cm × 8 cm. 20 second MPI acquisition.

MPI for SPIO imaging would facilitate quantification of cell delivery and retention, leading to better understanding of dynamic events such as graft movement in such brain disease models.

To evaluate MPI for long-term tracking of neural implants, we stereotactically implanted 5×10^5 SPIO-tagged hESC-derived NPCs in 5 µL PBS solution in the forebrain of two immunosuppressed rats, representing a standard therapeutic dose for neural cell implants [76, 77, 78]. To assess MPI monitoring of cell graft mobility and clearance *in vivo*, we also implanted an equivalent number of labeled NPCs near the lateral ventricle of a third animal to facilitate translocation and potential clearance of the graft. 0.15 µL Resovist tracer diluted in 4.85 µL PBS was administered to the forebrain of a fourth animal as a control. Due to institutional policy, we began longitudinal imaging of the animals post-recovery at day 10 for animals 1-3 and day 4 for animal 4. We then monitored the graft signals using MPI imaging

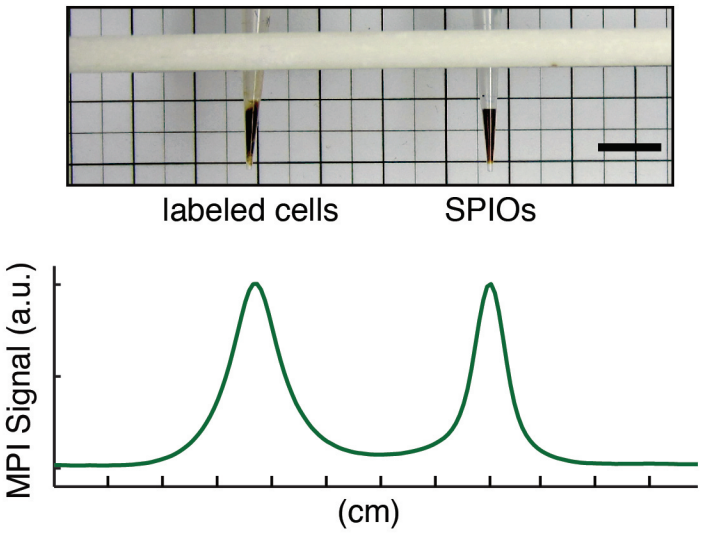

Figure 4.6: MPI 1D line profile of Resovist-labeled cells and Resovist point sources. The FWHM resolution of the MPI signal is approximately 1.5-fold better for Resovist SPIO particles alone, at 5 mm, than for SPIO particles transfected into cells, at 7.7 mm. Scale bar: 1 cm.

for a period of 87 days post-administration. Serial MPI images of cell grafts show high signal contrast with no detectable signal from surrounding anatomy (Fig. 4.7). Figure 4.8 shows total MPI iron signal from the cell graft in animals 1-2 had non-significant decay over time. In contrast, the cell graft in animal 3 exhibited the presence of iron caudal/posterior to the implant site and significant iron clearance compared to animals 1-2, suggesting movement and clearance of NPCs throughout the ventricle. The control animal receiving SPIO tracer alone showed no long-term detectable MPI signal.

4.3.5 Histological and MRI Validation

We then compared MPI cell tracking data to postmortem Prussian blue (PB) staining and MRI (Fig. 4.9). Animals 1 and 2 (Fig. 4.9) showed the presence of SPIOs only at the injection site. In Animal 3, PB staining and MRI also revealed the presence of SPIOs adjacent to the lateral ventricle (Fig. 4.11), which confirmed the MPI observation that tagged cells had migrated posteriorly throughout the ventricle. Additional postmortem PB staining did not show any residual iron in the brain of the animal that received tracer alone, indicating rapid tracer clearance seen in MPI images. Immunohistochemical staining against neural progenitor markers nestin, and human-specific neural cell adhesion molecule (NCAM), and human cytoplasmic marker SC121 confirmed the presence of human SPIO-labeled cells at the administration site (Fig. 4.10). Expression of the macrophage/microglial marker CD68

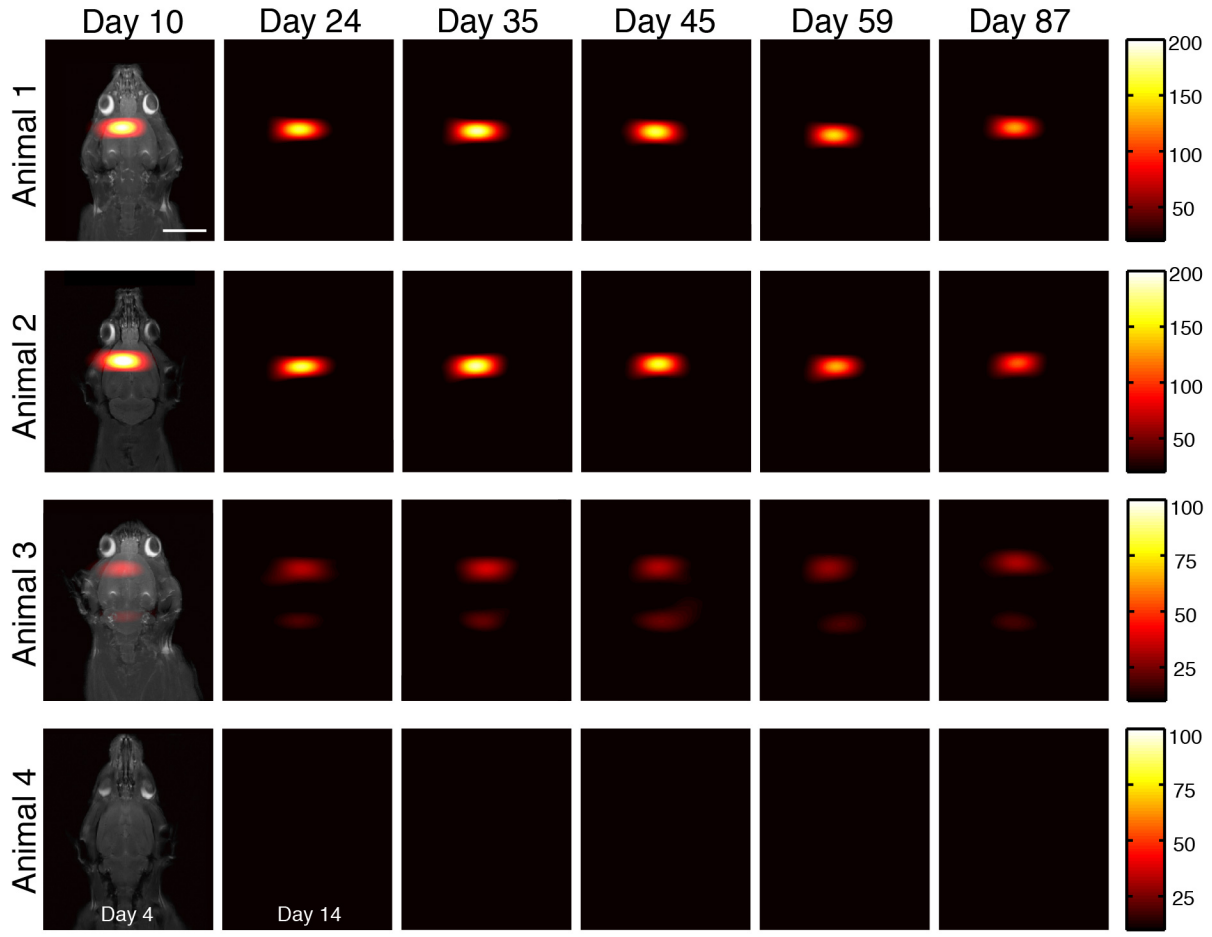

Figure 4.7: MPI quantitatively tracks NPC neural implants in rats over 87 days. (a) Longitudinal MPI imaging of 5×10^5 SPIO-labeled human NPCs implanted in the forebrain cortex (Animals 1-2), near lateral ventricle (Animal 3), and equivalent SPIO-only tracer in the forebrain cortex as control (Animal 4). MPI imaging quantifies graft clearance and movement over time, with rapid total clearance of SPIO-only injection (MPI: 30 sec acquisitions, 9.3 cm $\times$ 6 cm FOV, color intensity in ng/mm^2, MRI reference: 10 min acquisitions, 7.5 cm $\times$ 4 cm, 384 $\times$ 384 matrix). All images are equally scaled; scale bar: 1 cm.

showed some immune cell infiltration within the grafts. CD68 staining also indicated the presence of iron-containing immune cells along the lateral ventricle in Animal 3, indicating immunogenicity as a mechanism of graft clearance.

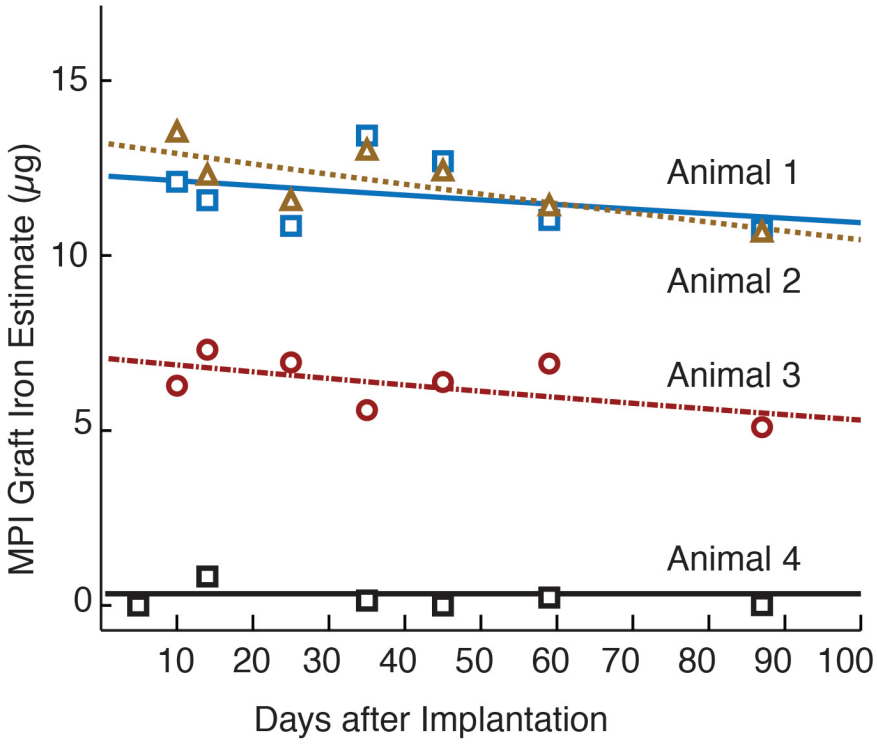

Figure 4.8: Total iron MPI estimates for *in vivo* cell grafts are plotted as a function of time with exponential fit. *In vivo* iron in Animal 1 and 2 do not show significant decrease over time, while iron signal was significantly decreased in Animal 3 starting Day 10. Animal 4 showed no long-term persistent MPI signal.

4.4 Discussion

In this study, we describe the use of longitudinal *in vivo* MPI to track and quantify implanted neural cell grafts over three months. We also demonstrate that the MPI signal is linear and can be used to quantify cell number *in vivo*, and that our projection format MPI scanner has a detection sensitivity of as few as 200 cells *in vitro*. As a comparison, MRI, SPECT, PET, and fluorescent imaging are reported to have robust detection limits greater than 10^4 cells, with only bioluminescent imaging able to detect 10^3 cells superficially implanted in small animals [25]. We note that in the described prototype MPI scanners, noise in the detector coil preamplifier, at around 1 nV/$\sqrt{Hz}$, had not yet been optimized and can be further improved by 1-2 orders of magnitude. This preamplifier noise exceeds unwanted harmonic interference and is currently the dominant noise source in our MPI systems. Thus, with further instrumentation development, the true physical limit of *in vivo* detection for MPI may range between 1-10 cells at scanning times between seconds to minutes.

An area of promising research in MPI is improving the spatial resolution, now roughly

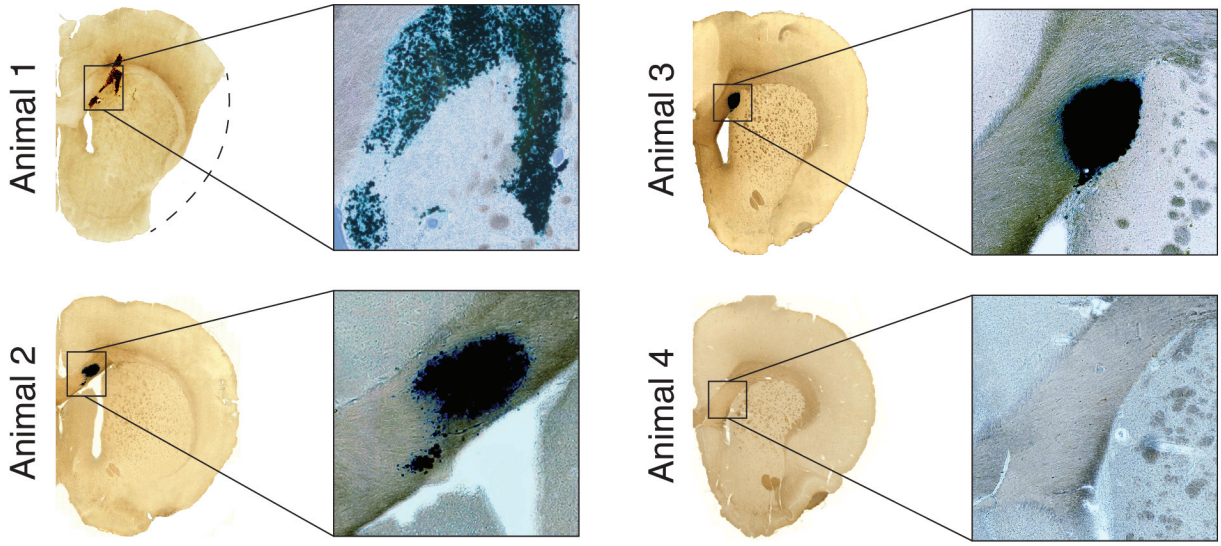

Figure 4.9: Histological, validation of iron location and quantification. Histological analysis of NPC grafts. Postmortem Prussian blue (PB) staining confirms presence of iron-labeled cells at administration site but not for SPIO-only control (Animal 4).

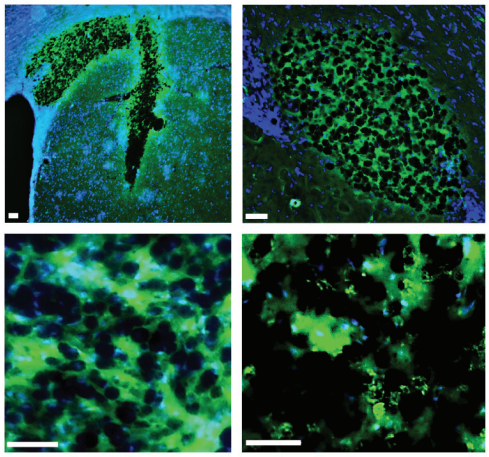

Figure 4.10: Representative immunohistochemical slices (top right panels) are shown for NPC marker nestin (top left, Animal 1), neural cell adhesion molecule (top right, Animal 3), and human-specific cytoplasmic marker SC121 (bottom left, Animal 2), which indicate iron label within NPC grafts. CD68 staining (bottom right, Animal 3) also indicates immune cells at administration site, suggesting immune-based graft clearance. Scale bars: 100 µm.

1 mm with a 7 T/m magnetic gradient. Here, we employed 2.35 T/m gradients for a FFL scanner, which yielded approximately 7 mm spatial resolution when imaging cells labeled

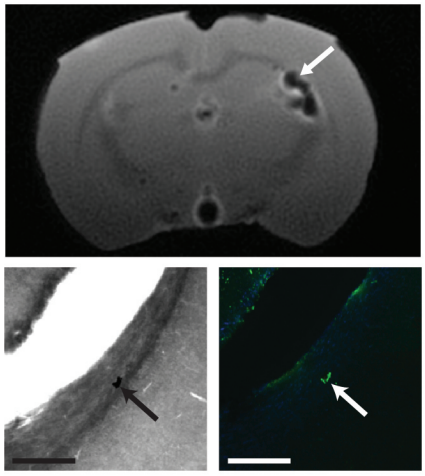

Figure 4.11: Postmortem axial MRI indicates iron in lateral ventricle in Animal 3 (arrow). PB and CD68 staining of lateral ventricle in Animal 3 shows SPIO uptake by immune cells. MRI: 20 min acquisition, 2.56 cm isotropic FOV, 256^3 pixel matrix. Scale bars: 1 mm.

with Resovist tracer. Spatial resolution in MPI is predicted to increase linearly with the gradient field strength and cubically with improved nanoparticles [2]. For example, previously published 22 nm particles enable double the image resolution of Resovist [79], which behaves similar to a solid core 17 nm particle [72]. Many groups continue to develop MPI-optimized contrast agents for improved MPI resolution [80, 81, 82, 83, 84].

We routinely observed an intriguing change in MPI spatial resolution between Resovist tracer alone and Resovist-labeled cells, an effect also noted in previous studies on the MPI signal of SPIO-labeled red-blood cells [85, 86]. Possible mechanisms for this resolution change could include size-selective endocytosis of transfection agent-Fe complexes [29, 87], increased MPI relaxation effects due to increased intracellular viscosity [88, 89], and transfection agent- mediated nanoparticle aggregation that may cause changes to the bulk particle magnetization and relaxation properties [90, 36, 91]. A better understanding of the mechanism underlying this phenomenon would not only enable tailored nanoparticles for MPI cell tracking, but could also potentially be exploited to generate image contrast based on nanoparticle relaxation or clustering. For example, changes in particle relaxation due to changes in pH or viscosity may be used to differentiate between different physiological conditions in live and dead cell populations, detect cell apoptosis, or image *in vivo* uptake of SPIOs by immune cells.

It is clear that the direct detection of SPIO labels in MPI can enable studies that require longitudinal monitoring of cells in anatomy previously inaccessible to optical, MRI, and nuclear techniques, such as the GI tract, pulmonary vasculature, and near bone. MPIs high image specificity for SPIOs enables visualizing systemic cell retention, migration, and biodistribution post-administration [25]. These systemic monitoring applications could include non-invasive probing of the immune system, such as the monitoring of labeled macrophages

migrating to sites of inflammation [25, 92, 93] and monitoring the fate of labeled T-cells used in immunotherapies. Finally, the SPIO labels and magnetic fields used in MPI have been shown to be human-safe [8], enabling a clear path to clinical MPI translation.

Chapter 5

MPI quantitatively monitors the transplantation, dynamic biodistribution, and clearance of intravenous mesenchymal stem cell implants *in vivo*

5.1 Introduction

In Chapter 5, I describe the first *in vivo* use of MPI to systemically track intravenous administrations of therapeutic mesenchymal stem cells over 12 days. This study was also the result of a collaboration with the Schaffer research group at UC Berkeley and a visiting researcher from Hamburg Technical University. In this work, I prepared the experimental design, performed longitudinal *in vivo* MPI imaging and postmortem CT imaging, performed tissue biodistribution studies, and composed the manuscript and figures toward publication. In the following section, I begin by motivating the need for preclinical and clinical tracking of mesenchymal cell-based therapies.

Mesenchymal stem cells (MSCs), which are multipotent and are found in many tissue types, are of particular therapeutic interest as cell therapies because they can control inflammation and modify the proliferation and cytokine production of immune cells [94]. MSC-based therapies have shown promise for treating diseases such as stroke, graft versus host disease, myocardial infarction, traumatic brain injury, and cancer [94, 95, 96]. Intravenous injection is a common route for the delivery of MSCs in applications ranging from traumatic brain injury to myocardial infarction in both animal models and clinical trials [96, 97]. However, recent studies have suggested that more than 80% of MSCs are entrapped in pulmonary vasculature following intravenous injection, leading to low delivery efficiency to target organs [94, 98, 99, 100, 101]. Moreover, it remains difficult to noninvasively monitor

the delivery and biodistribution of administered cells into target organs quantitatively and longitudinally without relying on behavioral endpoints or tissue histology [96, 98, 100].

In MPI, a static magnetic gradient field, with a central field-free region (such as a field-free point, or FFP), is applied to the imaging field-of-view (FOV). This gradient field saturates the nonlinear magnetization of all SPIO particles within the FOV except those at the field free point. To form an MPI image, the FFP is rastered across the 3D FOV using a combination of electromagnets. MPI signals are generated when the FFP traverses a location containing SPIOs, causing the SPIO magnetization at that location to change in magnitude and orientation in response [38]. This change in SPIO magnetization can be detected via a receiver coil and assigned to the instantaneous FFP location to form the final MPI image. We note that MPI is a linear and shift-invariant imaging system, with a well-characterized point spread function that is simply the derivative of the SPIO magnetization curve [2, 42, 39]. Because of the linearity and shift-invariance of the MPI image intensity with respect to SPIO tracer concentrations, MPI images can be used to quantify SPIOs or labeled cells within the imaging FOV.

Moreover, because biological tissues neither generate image contrast in MPI nor interfere with the low-frequency magnetization signals generated by SPIO tracers, MPI images exhibit extremely high image contrast, similar to PET or SPECT nuclear medicine scans. Figure 5.1A-B show a MPI and an fluorescent scan of SPIO tracers in glass capillary tubes embedded at increasing depths in a tissue phantom. As is well characterized in literature [102, 103], the fluorescent signal shows exponential signal loss with tissue depth. However, the MPI signal shows no significant dependence on surrounding tissue and hence may be clinically translatable for applications in molecular imaging.

In this study, we investigated whether MPI can be used to quantitatively track SPIO-labeled hMSCs *in vivo*. We intravenously administered SPIO-labeled hMSCs in rat and monitored the injections and the dynamic *in vivo* distribution of the hMSCs using MPI over a period of 12 days. We also used the longitudinal MPI signal to quantify SPIO tracer clearance from the body after injection. Finally, SPIO biodistribution in lung, liver, heart, and spleen were determined postmortem via MPI imaging and compared to induction-coupled plasma spectrometry as a reference standard.

5.2 Methods

5.2.1 Comparison of MPI, fluorescent, and MRI tracer imaging in postmortem mouse

A 12-week old CD-1 female mouse was sacrificed via CO_2 inhalation and cervical dislocation. Post-sacrifice, sealed polyethylene tubes containing a 2 µL mixture of 120 pmol Angiosense 680 EX fluorescent tracer (PerkinElmer, Waltham, MA) and 20 nmol Nanomag-MIP SPIOs (MicroMod, Rostock, Germany) were implanted 1.0 mm and 2.8 mm below the dorsal skin surface for imaging. Fluorescent imaging was performed on IVIS Spectrum (PerkinElmer)

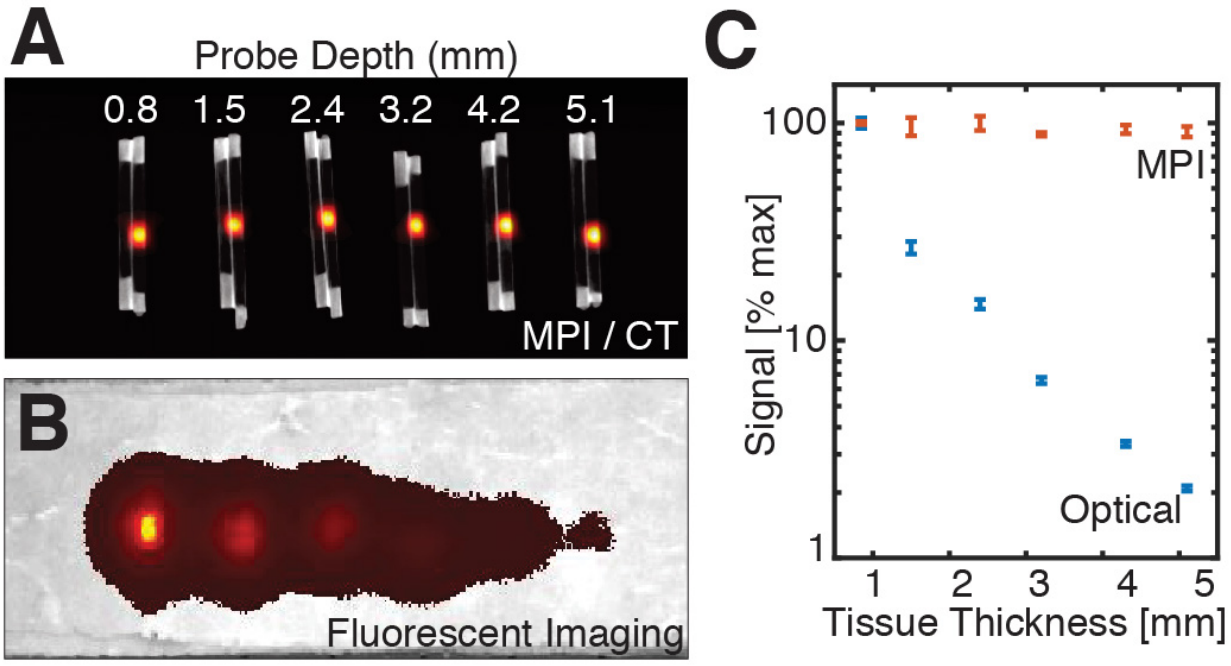

Figure 5.1: Quantitative comparison of MPI and fluorescent signal with tissue depth. Six equivalent SPIO and fluorescent probes in sealed capillary tubes were placed at various depths in a sectioned porcine muscle phantom. (A-B) Maximum intensity projection MPI/CT images show constant SPIO signal at various depths in tissue, but equivalently placed fluorescent probes show significant signal reduction with tissue depth. (C) Log plot of image signal with tissue depth for MPI and fluorescent imaging shows no significant dependence of MPI signal on tissue depth, but exponential decrease of optical signal with increasing tissue depth. MPI imaging (n = 3): 4 cm × 3.75 cm × 8 cm FOV, 5.3 min scan. Fluorescent imaging (n = 5): 2 second exposure, F/2, 675 and 720 nm excitation/emission filters. CT imaging: 25 min acquisition, 184 µm isotropic resolution.

using 5 second scan time, F/2, and excitation/emission filters at 675 and 720 nm, respectively. CT imaging was performed on a RS9-80 Micro CT scanner (General Electric) with 15 min scan time and 184 µm isotropic resolution. MR imaging was performed on a Bruker PharmaScan 7T scanner using a multi-slice multi-echo sequence with 4 × 8 cm FOV and 384 µm in-plane resolution, 10 slices total with 0.5 mm slice thickness, and 17 minute scan time. MPI imaging was performed using a custom 7 T/m MPI scanner with 30 mTpp drive field, 5 × 3.75 × 10 cm FOV, and 6.8 min acquisition.

5.2.2 MPI and fluorescent imaging of a porcine tissue phantom

All MPI studies in this work are performed on a 3D MPI scanner with a 7 T/m magnetic field gradient and a drive field at 40 mTpp amplitude and 20.05 kHz drive frequency [8]. MPI images were reconstructed using an x-space MPI reconstruction algorithm [2, 42, 39] and windowed at 10% full scale. All data acquisition, control, and data processing were performed with MATLAB (Mathworks, Natick, MA).

To quantitatively assess MPI performance in deep tissue imaging, we designed a custom phantom comprised of stacked fresh porcine muscle sections. 6 pairs of MPI and fluorescent probes in sealed glass capillary tubes were placed adjacently within the tissue phantom at depths of 0.8 mm, 1.5 mm, 2.4 mm, 3.2 mm, 4.2 mm, and 5.1 mm from the phantom surface, spaced approximately 1 cm apart laterally. MPI probes were comprised of 2 µL undiluted Nanomag-MIP SPIOs. Fluorescent probes were 160 pmol reconstituted Angiosense 680EX in 2 µL deionized water solution. MPI imaging was performed in triplicate in a 5.3 min scan with 4 cm × 3.75 cm × 8 cm FOV. Fluorescent imaging was performed (n = 5) on IVIS Spectrum with 2 second exposure, F/2, and excitation/emission filters at 675 and 720 nm. For probe localization, a reference CT scan was performed (GE RS9-80 CT, 25 min acquisition, 184 µm isotropic resolution).

5.2.3 Resovist labeling of hMSCs

Bone marrow-derived human mesenchymal stem cells (ATCC PCS-500-012) were seeded at initial density of 5000 cells per cm^2 in 5 mL of complete growth medium (ATCC PCS-500-041). The seeded culture flasks were incubated at 37 degrees Celsius with 5% CO_2. At 70%-90% confluence, cell cultures were passaged into new culture flasks using 0.05%-trypsin-EDTA to detach cell monolayer from flask surface, trypsin neutralizing solution to stop the trypsin digestion of cells, and Dulbecco Phosphate Buffered Saline (PBS) to maintain media pH value between 7.2 to 7.4. Dissociated cells are centrifuged for 3 minutes at 1500 rpm for collection, counted using a hemocytometer, and reseeded at initial growth conditions. All cell counting was performed using a hemocytometer and averaged (n=5).

Resovist superparamagnetic iron oxide particles (Bayer Schering Pharma AG Leverkusen, Germany; 0.5 mmol Fe/mL) were used for cell labeling using methodology similar to previous studies [35, 36]. Resovist is a MRI contrast agent intended for the detecting and characterizing of small liver lesions [33]. Resovist particles were added to growth medium in culturing

flasks containing adherent cells with a confluency of 50% to 80% to achieve desired Fe concentration. Cells were incubated with the Resovist solution for 24 hours. After labeling, cultures were washed twice with PBS to remove remaining free and surface-bound Resovist particles. Cells were trypsinized, centrifuged, resuspended in PBS and kept on ice no longer than 2 hours until injection.

5.2.4 Determination of hMSC iron labeling efficiency, loading content, and viability

To determine SPIO labeling efficiency, cells were cultured in a 24-well-plate containing 6 samples each for the following four Fe labeling concentrations: 0 µg Fe/mL, 20 µg Fe/mL, 30 µg Fe/mL and 40 µg Fe/mL. Iron-labeled cells were visualized using a Prussian blue cell staining kit (Ocean NanoTech, Springdale, AR, USA). Prussian blue-labeled cells were counted manually using a microscope to determine average cell labeling efficiency.

hMSC iron loading was determined by induction-coupled plasma optical emission spectrometry (Optima 5300 DV, PerkinElmer, Waltham, MA). Cells were cultured and labeled with Resovist as above with Fe concentrations of 20 µg Fe/mL, 30 µg Fe/mL and 40 µg Fe/mL in the incubation media. Prior to measurement, 3 hMSC samples at each labeling concentration, containing respectively $121 \times 10^3 \pm 19 \times 10^3$ cells/sample, $121 \times 10^3 \pm 13 \times 10^3$ cells/sample, and $135 \times 10^3 \pm 52 \times 10^3$ cells/sample, and 3 samples of 1 µL undiluted Resovist in 100 µL PBS solution were digested using a mixture of 1 mL 70% nitric acid (Fisher A509P500) and 300 µL 30% hydrogen peroxide (Ricca 3821.7-16) overnight at room temperature and subsequently diluted to 30 mL using deionized water. A linear regression line is created with Fe standard solutions at concentrations of 0, 10, 100, 1000 ng Fe/mL. ICP analysis was performed in triplicate to determine cellular iron as mean *pm* SD in picograms of iron per cell.

For assessment of cell viability after SPIO labeling, cells labeled using 0 µg Fe/mL, 20 µg Fe/mL, 30 µg Fe/mL and 40 µg Fe/mL Resovist were harvested and resuspended in a solution of 93.5% basal media and 6.5% FBS and pipetted into a 96-well-plate for assessment. A blank group contained only the basal media / FBS solution with no cells. For each group, three samples were separately cultured, labeled, resuspended and transferred into the 96-well-plate.

An MTT-based *in vitro* Toxicology Assay Kit (Sigma Aldrich, Saint Louis, MO, USA) was applied to the five different groups with three samples each. One vial of MTT powder was dissolved in 3 mL of basal media / FBS. Reconstituted MTT in an amount equal to 10% of the culture medium volume was added. Cultures were returned to the incubator for 4 hours. After incubation, the resulting formazan crystals were dissolved by adding an amount of MTT solubilization solution equal to the original culture medium volume of 150 µL per well and shaken gently. After about 30 minutes, the probes were transferred to a multiplate reader. The absorbance of the colored solution was measured at wavelengths 570 nm and 650 nm after 15 and after 30 minutes. Comparisons in viability between groups were per-

formed using analysis of variance and Bonferroni Post-Hoc test for multi-pair comparisons. Differences were considered significant at $p < 0.05$.

5.2.5 Animal Procedures

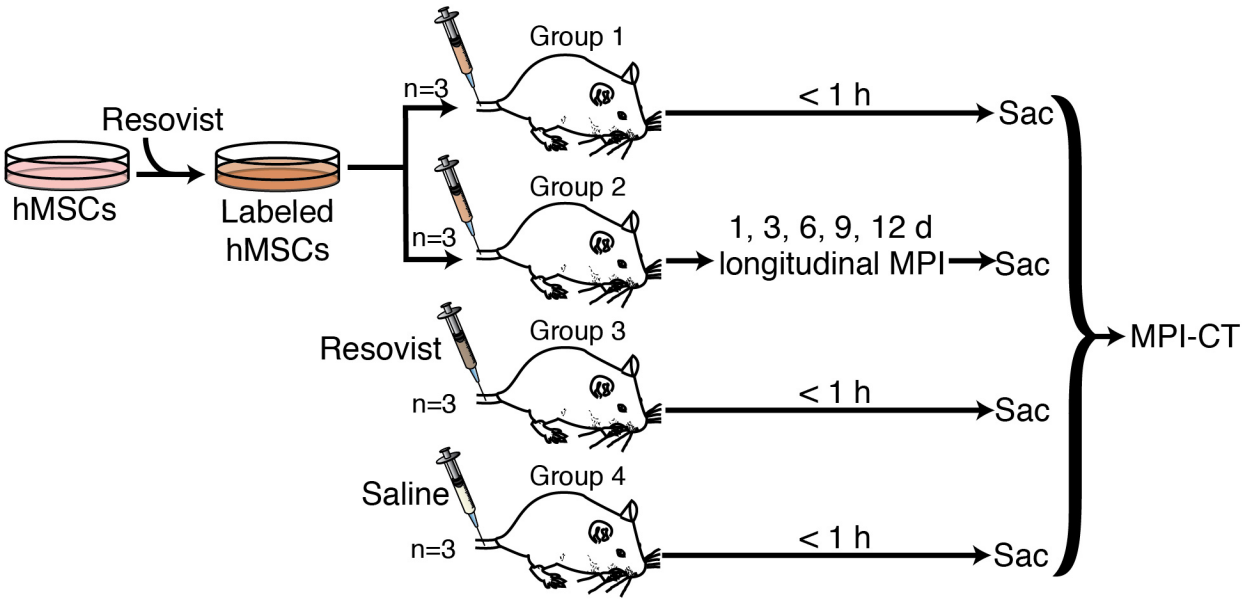

Figure 5.2: *In vivo* intravenous MSC administration experiments in rat. 4 groups of 3 animals each were used in this study. Groups 1 and 2 received tail vein injections of 5×10^6 to 8×10^6 Resovist-labeled mesenchymal stem cells. Group 3 received an equivalent tail vein injection of Resovist alone, and Group 4 received a tail vein injection of isotonic saline. Groups 1, 3, and 4 were sacrificed within one hour of injection and imaged using MPI and CT, while Group 2 was imaged *in vivo* using MPI over 12 days after injection, followed by sacrifice and MPI-CT imaging. Post-sacrifice, all animals were dissected and the liver, lungs, heart, and spleen were harvested for MPI imaging and iron distribution analysis.

All animal procedures were approved by the Animal Care and Use Committee at UC Berkeley and conducted according to the National Research Councils Guide for the Care and Use of Laboratory Animals. Immunocompetent 7-week old female Fischer 344 rats weighing approximately 130 g and a 12-week old CD-1 female mouse weighing approximately 40 g were used for MPI imaging. Animals were fed on a diet of Teklad Rodent Diet 2018 (Harlan, Indianapolis, IL) *ad libitum*.

Briefly, four groups of rats (Fig. 5.2) anesthetized under isoflurane (4% for induction and 2% for maintenance, 1.5 L/min flow) received tail vein injections of 5×10^6 to 8×10^6 Resovist-labeled hMSCs in 1 mL PBS (n=3, Groups 1 and 2) [98, 101], 100 µL Resovist diluted to 1 mL in PBS (n=3, Group 3), or 1 mL isotonic saline solution (n=3, Group 4).

hMSCs used for animal injections were labeled with 40 µg Fe /mL of Resovist in cell culture solution. Animals in Group 1, 3, and 4 were sacrificed via isoflurane overdose within one hour of injection for postmortem MPI and CT imaging. Animals in Group 2 were monitored and imaged *in vivo* using MPI at 1, 3, 6, and 9 days post-injection, and sacrificed via isoflurane overdose for MPI and CT imaging 12 days post-injection.

5.2.6 Animal MPI Imaging

For *in vivo* small animal MPI imaging, animals were placed in a 7 T/m FFP MPI scanner under isoflurane anesthesia (2%, 1.5 L/min) using a custom animal bed. *in vivo* and post-mortem MPI scans were conducted using a $4 \times 3.75 \times 10$ cm FOV in a 9 minute acquisition. All animal MPI imaging was performed in quadruplicate. Anatomic CT reference images were also acquired (RS9-80 CT, 25 min acquisition, 184 µm isotropic resolution), and MPI-CT 3D images were co-registered with Osirix Imaging Software (Pixmeo SARL, Switzerland) using SPIO-glass fiducial markers.

To estimate SPIO tracer quantity from MPI images, a standard curve of iron quantity to volumetric MPI signal was created using MPI scans of 1, 2, 3, and 100 µL Resovist tracer. To determine iron clearance half-life from hMSC injections in Group 2, an exponential regression fit was applied to the total *in vivo* longitudinal MPI signal, and the line-of-best-fit and 95% confidence intervals were determined.

5.2.7 MPI biodistribution studies

For assessment of SPIO biodistribution using MPI, all animals from all groups were dissected post-sacrifice and the liver, spleen, heart, and lungs were harvested. The organs were imaged in quadruplicate using MPI, with $4 \times 3.75 \times 10$ cm FOV and 9 minute acquisition time as before. SPIO biodistribution was determined in µg as mean $\pm$ s.d. using a calibration curve and the volumetric MPI signal in each organ.

5.2.8 ICP biodistribution studies

For validation of MPI biodistribution results, an induction-coupled plasma (ICP) optical emission spectroscopic analysis on the excised organs was carried out by Analytical Resources Incorporated (Tukwila, WA) using sample preparation method 3050B and analysis method 6010C to determine iron content as mg/kg multiplied by organ mass. To compensate for physiologic background iron in ICP analyses, ICP-measured iron for each organ was subtracted by mean physiologic iron content from organs of age-matched, saline-injected animals in Group 4. A linear correlation, 95% confidence intervals, and correlation coefficient were determined for ICP- and MPI-measured iron for all harvested organs.

5.3 Results

5.3.1 hMSC labeling efficiency, SPIO uptake, and cytotoxicity

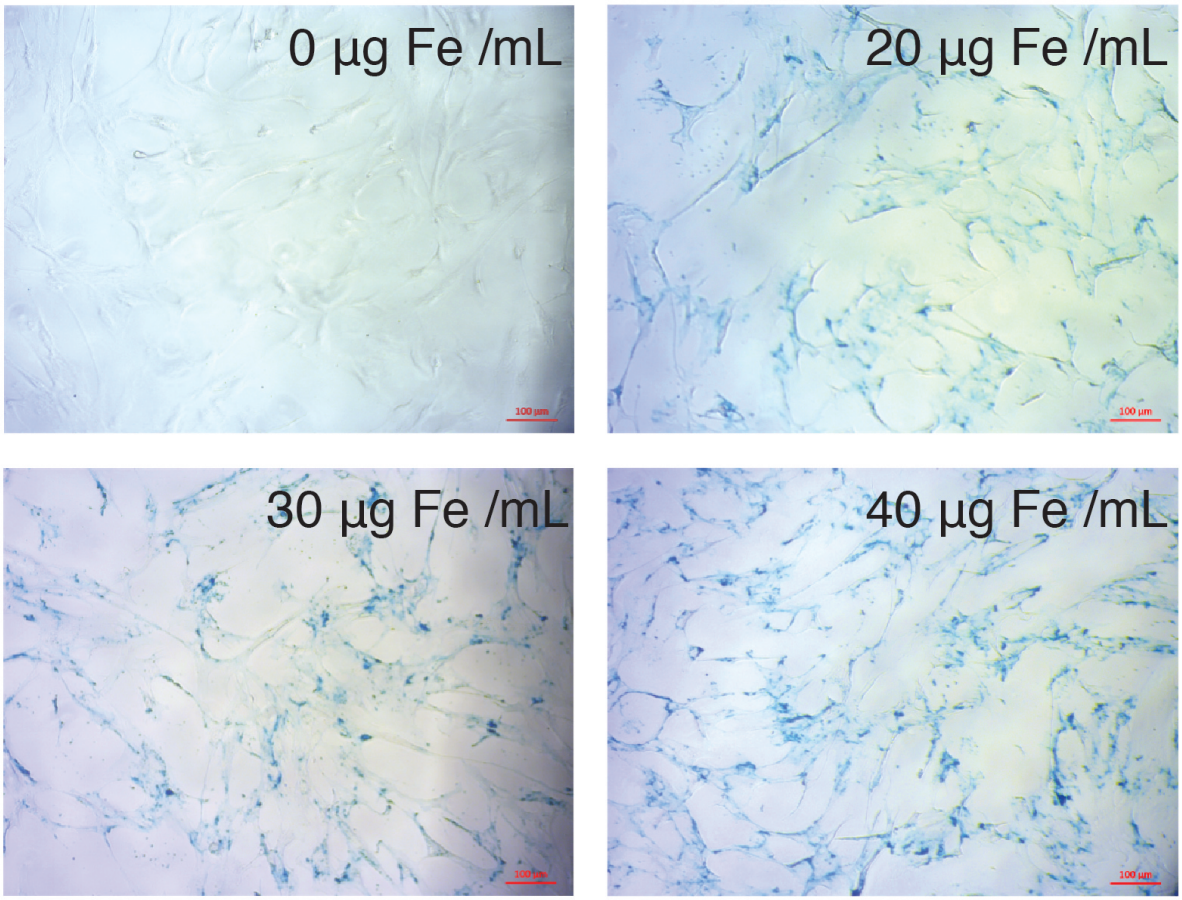

Figure 5.3: hMSC labeling using Resovist SPIO tracer. (A) Prussian blue staining of hMSCs labeled with four Resovist labeling concentrations ranging from 0 to 40 µg Fe / mL. Cells labeled with 40 µg Fe / mL Resovist show around 90-95% labeling efficiency with no differences in cell morphology. Scale bars: 100 µm.

We generated SPIO-labeled hMSCs using a modified standard protocol for MSC labeling [34, 35, 36]. Figure 5.3 shows Prussian blue-stained hMSC cell cultures labeled with 0, 20, 30, and 40 µg Fe/mL Resovist labeling concentration. A control group labeled using 0 µg Fe/ml indicates little to no visible PB staining. Between 90-95% cells were labeled at 20 µg Fe/mL labeling concentration, while 95-100% cells were labeled at 30 and 40 µg Fe/mL labeling concentrations.

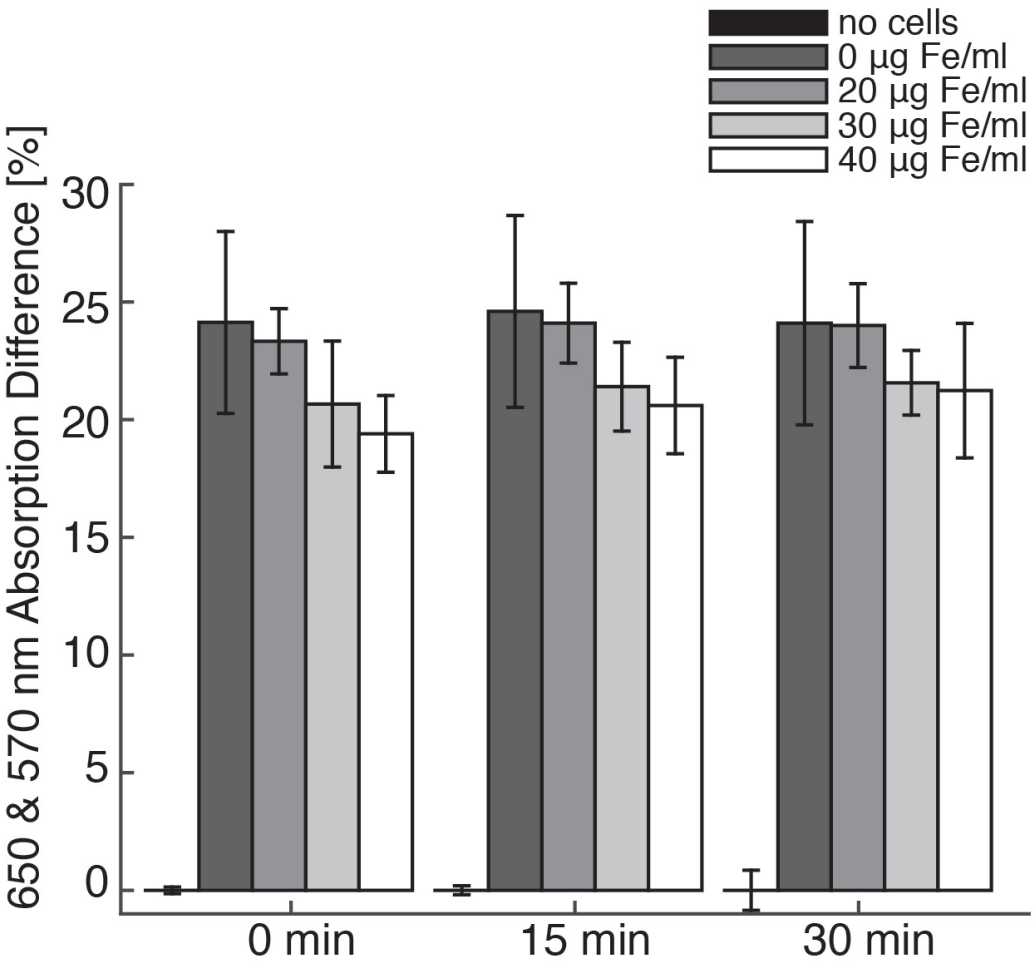

Figure 5.4: MTT viability test of SPIO-labeled hMSCs. (B) An MTT-based cell viability assay shows no significant differences in cell viability between unlabeled and labeled hMSC populations.

We then performed ICP-OES to determine intracellular iron uptake in labeled hMSCs. ICP analysis indicated iron uptake of 44.2 ± 11.1, 53.9 ± 11.8, and 77.8 ± 23.3 pg Fe/cell incubated with 20, 30, and 40 µg Fe/mL Resovist labeling concentration respectively (n=3 each). These intracellular iron uptake values are in agreement with published data for Resovist labeling of MSCs [34, 35, 36, 104, 105]. An MTT viability assay showed no significant difference in cell viability between unlabeled and labeled hMSC populations (Fig. 5.4).

5.3.2 *In vivo* and postmortem MPI studies

We next asked if MPI can be used to visualize the fate of intravascular hMSC injections *in vivo*. Previous studies on intravenous delivery of MSCs have shown that the majority of injected MSCs become entrapped in pulmonary vasculature during first passage, followed by clearance to liver within 1-2 days [94, 101, 106, 107]. To visualize the dynamics and biodistribution of intravascular hMSC injections using MPI, four groups (n=3 each) of Fischer 344 rats were injected with 5×10^6 to 8×10^6 Resovist-labeled hMSCs (Groups 1 and 2), 100 µL Resovist (Group 3), or 1 mL isotonic saline solution (Group 4) via the tail vein. Groups 1, 3, and 4 were imaged within 1 hour of injection, while longitudinal *in vivo* MPI imaging was performed on Group 2 up to 12 days post-injection.

Figures 5.5-5.8 show representative MPI-CT images after intravenous injection. MPI images of animals receiving labeled hMSC injections showed high SPIO content in the lungs immediately after injection (Fig. 5.5). In those animals, we measured up to 930 µM iron concentration in the lungs, corresponding to approximately 52 ng Fe/mm^3 in lung tissue. At 12 days post-injection (Fig. 5.6), MPI imaging indicates a significant decrease in total iron content, along with the localization of the majority of SPIOs to liver. Animals receiving Resovist-only injections showed immediate uptake of SPIOs in liver tissue (Fig. 5.7). There was no detectable MPI signal in animals receiving saline-only injections (Fig. 5.8).

To monitor the *in vivo* distribution and clearance of Resovist-labeled hMSCs, we imaged anesthetized hMSC-injected animals using MPI at 1, 3, 6, and 9 days post-injection. Quantitative MPI images (Fig. 5.9 and 5.10) show redistribution of hMSCs to the liver as early as 24 hours after injection. Our observation of the rapid trafficking of intravascularly injected MSCs to the liver agrees with previous dynamic imaging studies of *in vivo* MSC injections [99, 107]. Moreover, *in vivo* MPI showed a gradual decay in SPIO signal over time, with a clearance half-life of 4.6 days and 95% confidence intervals at 3.7 and 6.0 days. We note that the longitudinal liver MPI imaging was performed here in the absence of respiratory and cardiac gating, leading to benign image undulation artifacts due to physiologic respiration, which can be seen most prominently in MPI images at 3 and 9 days post-injection in Fig. 5.9. We also note these image artifacts do not appear in postmortem imaging and that the respiration-gated MPI may be implemented, similar to gating in nuclear medicine [108].

5.3.3 MPI biodistribution studies

To investigate the ability of MPI to assess tracer biodistribution, we performed *ex vivo* MPI imaging of excised liver, spleen, heart, and lungs. Representative MPI biodistribution images from each experimental group are shown in Figure 5.11. Fig. 5.11A shows that hMSC injections overwhelmingly localize to lung tissue upon injection, but are mostly cleared into liver over time (Fig. 5.11B). In contrast, injected Resovist was immediately taken up by liver and partially in the spleen (Fig. 5.11C). No MPI signal was detected for saline-only injections (Fig. 5.11D).

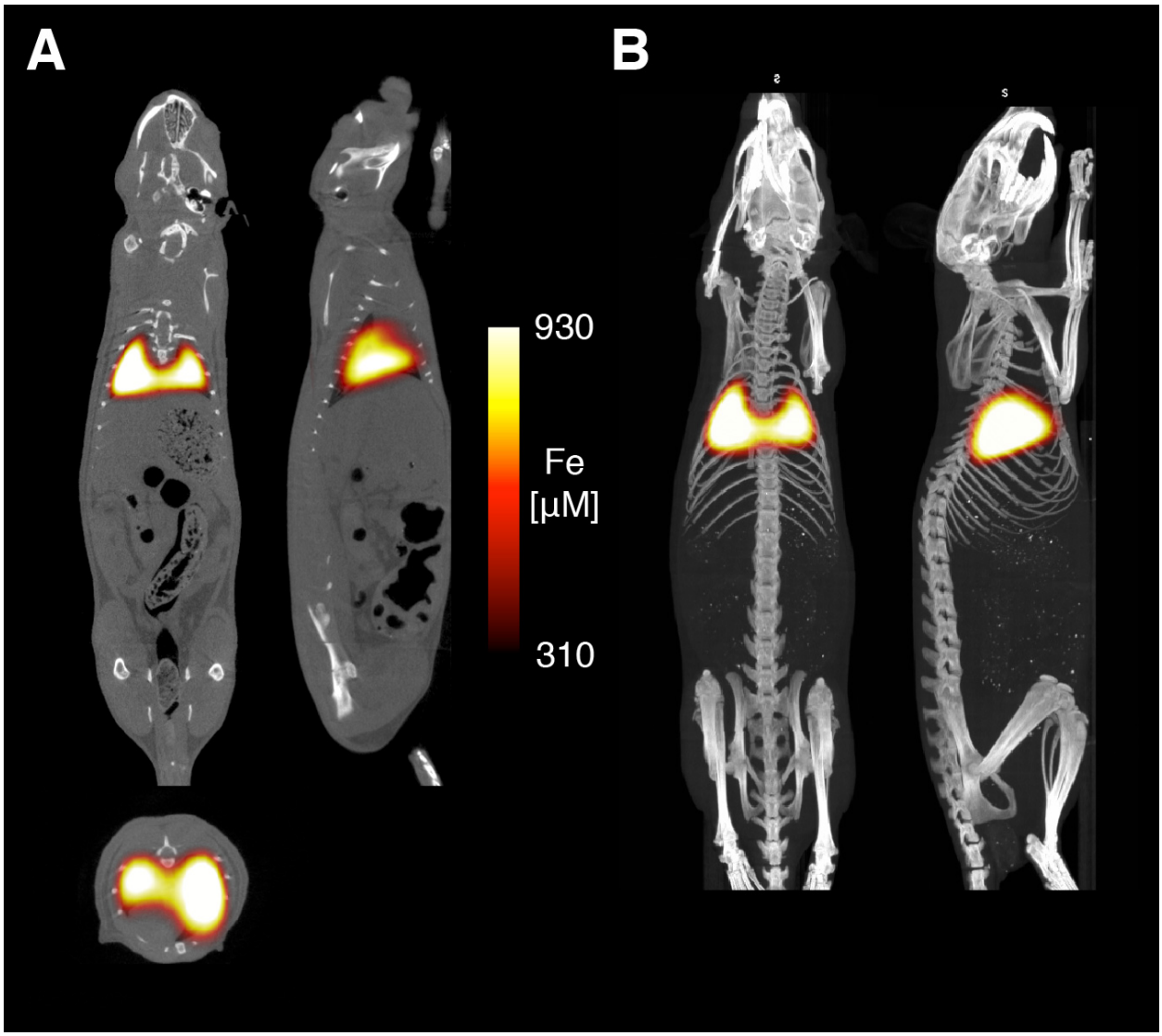

Figure 5.5: MPI-CT imaging of intravenously injected hMSCs at 0 days after injection with representative coronal, sagittal, and axial slices shown from full 3D MPI datasets. (A) MPI imaging of hMSC tail vein injections at less than one hour post-injection shows substantial hMSC localization to lung. (B) Maximum intensity projections of hMSCs lodged in lung vasculature. MPI imaging (n = 4 for each animal): 4 × 3.75 × 10 cm FOV, 9 minute acquisition. CT imaging: 25 minute acquisition, 184 µm isotropic resolution.

To validate MPI measurements of SPIO biodistribution, we performed ICP analysis for iron content in excised organs. The biodistribution of SPIOs after injection for each experimental group, as measured from MPI imaging, is shown in Fig. 5.12. For ICP iron measurements, we noted remarkable variation in measured SPIO content in the liver and

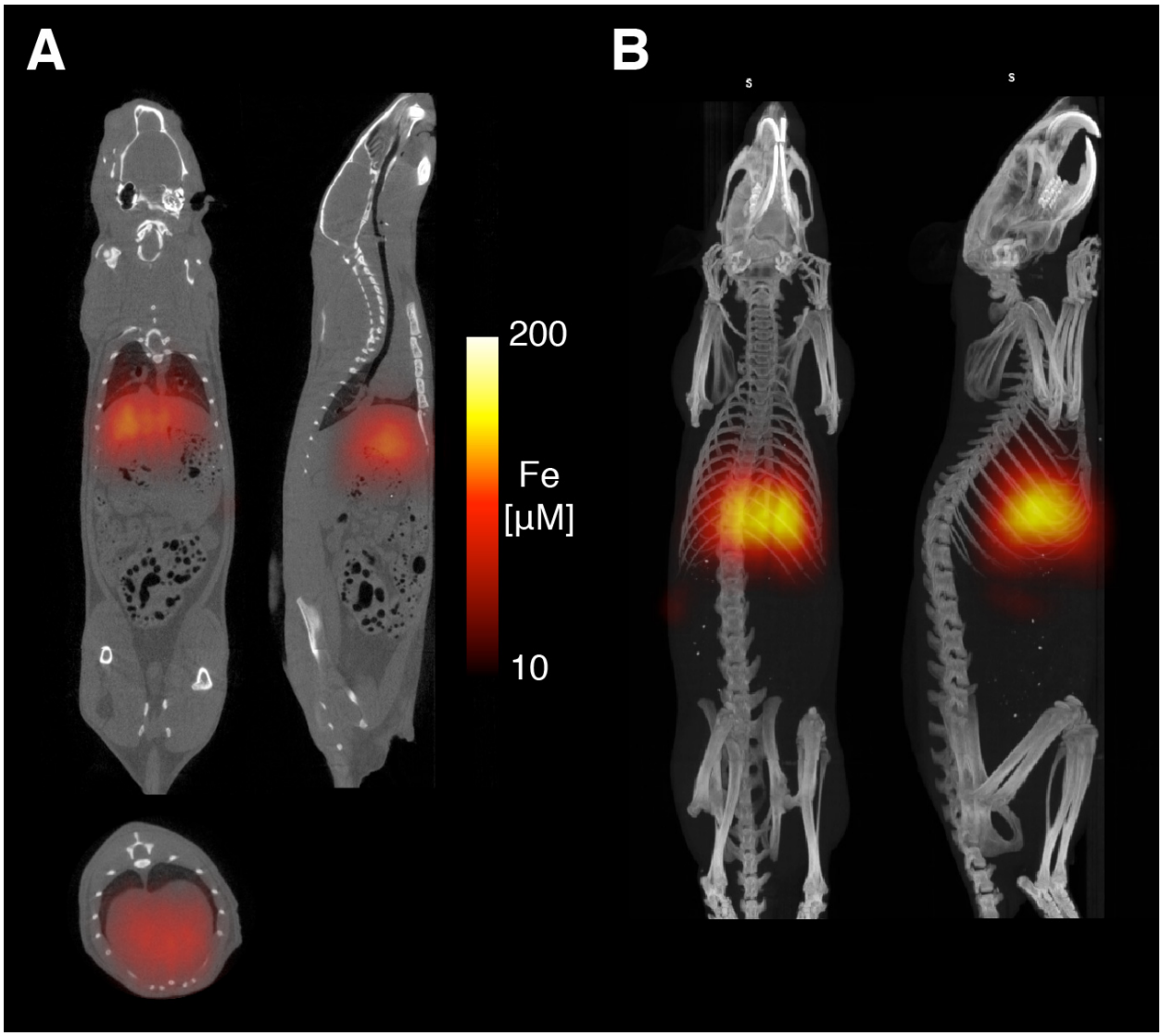

Figure 5.6: MPI-CT imaging of intravenously injected hMSCs at 12 days after injection with representative coronal, sagittal, and axial slices shown from full 3D MPI datasets. (A) At 12 days post-injection, hMSC tail vein injections show significant total clearance and liver migration. (B) Maximum intensity projections of hMSCs clearing out to liver at 12 days post-injection. MPI imaging (n = 4 for each animal): 4 × 3.75 × 10 cm FOV, 9 minute acquisition. CT imaging: 25 minute acquisition, 184 µm isotropic resolution.

spleen, presumably due to the variability of physiologic background iron content in those tissues. Nonetheless, a linear regression of ICP and MPI-measured iron content in excised organs (Fig. 5.13) shows excellent agreement ($R^2 = 0.943$, 95% confidence intervals shown for linear regression).

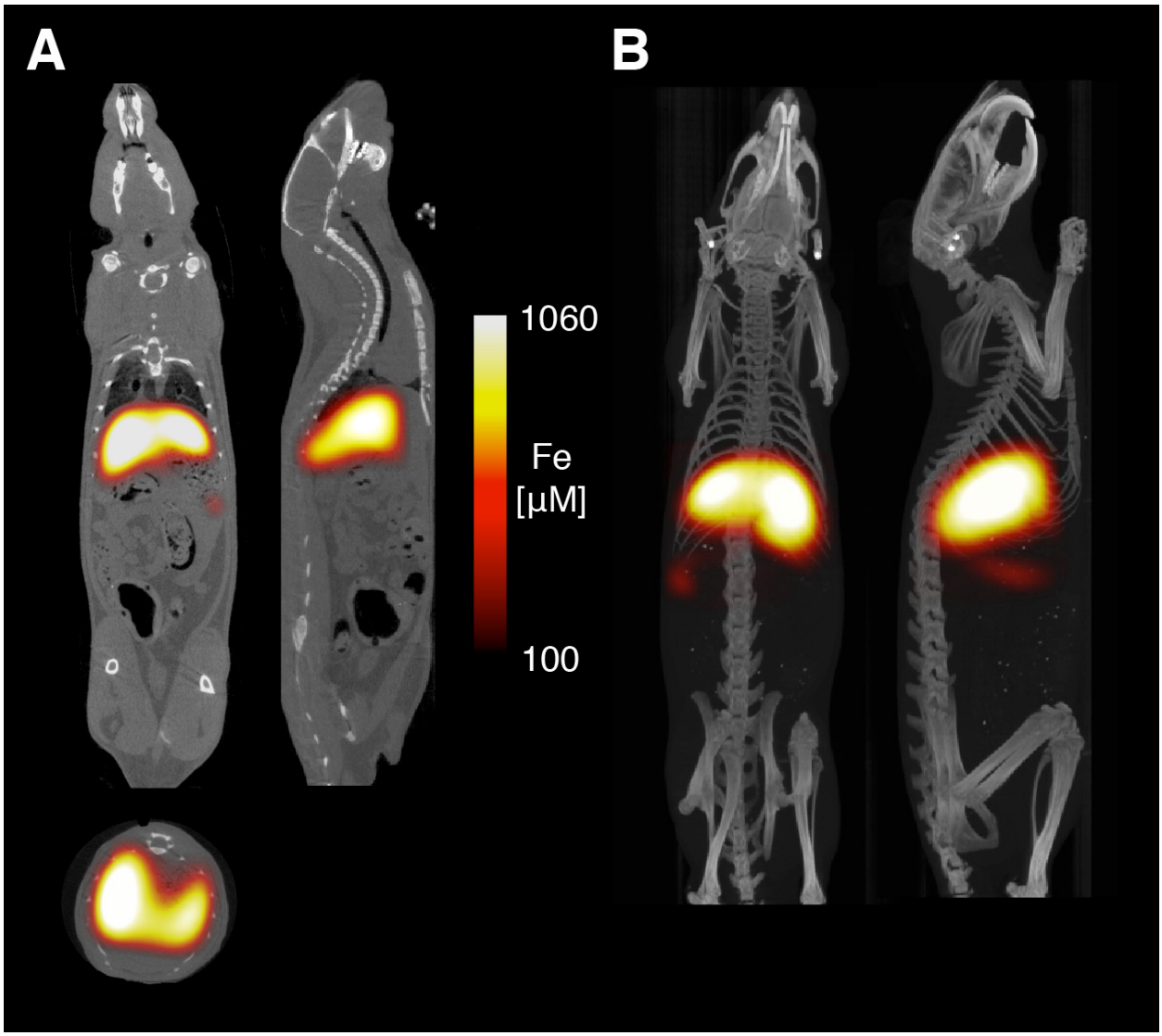

Figure 5.7: MPI-CT imaging of intravenously injected Resovist with representative coronal, sagittal, and axial slices shown from full 3D MPI datasets. (A) MPI imaging of Resovist-only tail vein injections at less than one hour post-injection shows immediate SPIO uptake in liver and spleen. (B) Maximum intensity projection images of Resovist injections in rat at less than one our post-injection. MPI imaging (n = 4 for each animal): 4 × 3.75 × 10 cm FOV, 9 minute acquisition. CT imaging: 25 minute acquisition, 184 µm isotropic resolution.

5.4 Discussion

In this study, we demonstrated the first use of Magnetic Particle Imaging to track and quantify intravenous administrations of human mesenchymal stem cells and SPIO tracer in

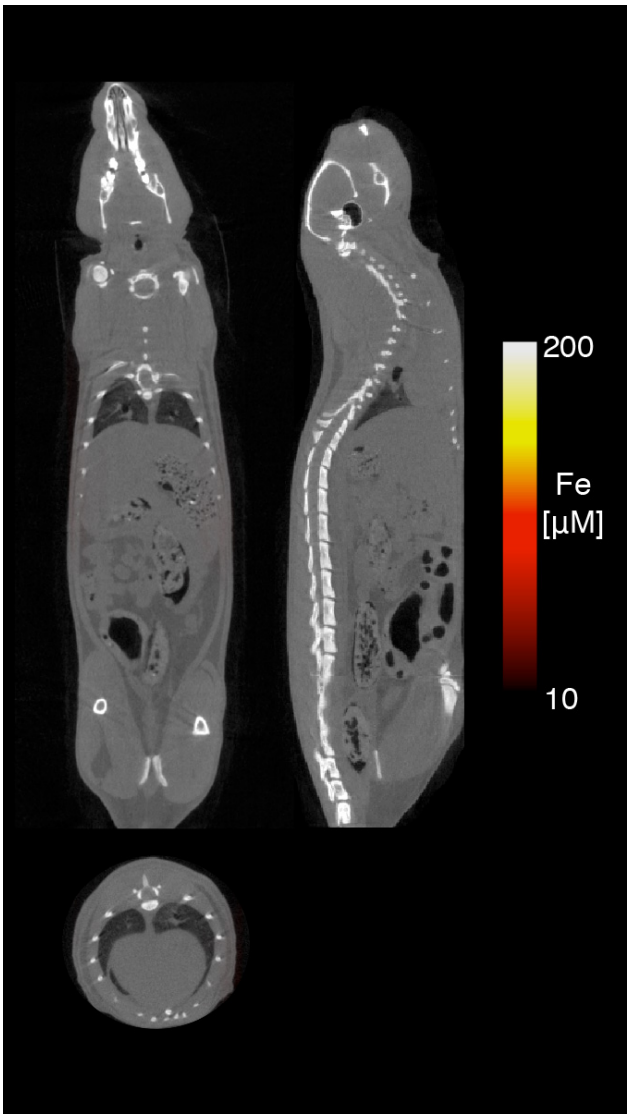

Figure 5.8: MPI-CT imaging of intravenously injected saline control with representative coronal, sagittal, and axial slices shown from full 3D MPI datasets. Control injections of isotonic saline show no detectable MPI signal. MPI imaging (n = 4 for each animal): 4 × 3.75 × 10 cm FOV, 9 minute acquisition. CT imaging: 25 minute acquisition, 184 µm isotropic resolution.

rats. MPI imaging visualized the *in vivo* dynamic biodistribution of the SPIO tracer with excellent contrast and sensitivity, noninvasively confirming that injected MSCs are rapidly entrapped in lung microvasculature and are mostly cleared to the liver within one day [94, 98, 100, 106]. MPIs linear quantitation and ability to image SPIOs longitudinally also enabled a noninvasive measurement of tracer clearance from the body. Here we measured a 4.6-day

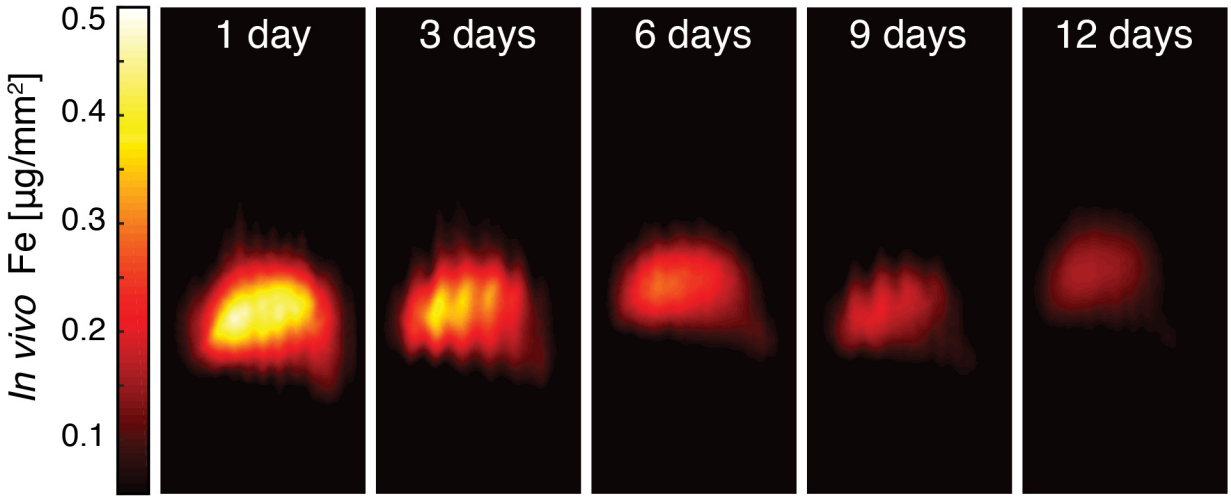

Figure 5.9: MPI imaging of *in vivo* SPIO liver clearance from hMSC injections. *In vivo* MPI monitoring of intravenous hMSC injections (shown here as coronal summed intensity projections) shows gradual clearance from liver tissue from 1 day post-injection to 12 days post-injection. *In vivo* MPI imaging also shows benign respiratory motion artifacts (seen most prominently at 3 and 9 days post-injection), which do not affect MPI quantification and can be removed via the use of respiratory gating. MPI imaging (N = 3 animals, 2 MPI scans per time-point per animal): $4 \times 3.75 \times 10$ cm FOV, 9 minute acquisition.

clearance half life for the SPIO label by the liver after intravenous injection, which is similar to previous findings [109]. Because the majority of MSCs cleared from the lung after infusion are not viable [94], our findings suggest that a better approach would be to administer MSCs arterially or directly in target tissue to improve targeted delivery of MSC-based therapies into organs of interest. However, for acute lung injury, the entrapment of intravenous MSC administrations in lung may trigger production of reparative growth factors and have an anti-inflammatory therapeutic effect [110, 111]. In all cases, It is important to noninvasively monitor the location and clearance of the cell injection to gain a better understanding of the dynamic response of MSC therapies.

Magnetic Particle Imaging can uniquely monitor the delivery and migration of cell therapies for weeks with high quantitative accuracy and image contrast. Although the MPI signal is generated by the nonlinear Langevin magnetization of SPIOs, it is linear and shift invariant with respect to the number and location of SPIOs. Importantly, no biological tissue exhibits similar superparamagnetic behavior that can produce interfering MPI signals. As a result, the image contrast and sensitivity in MPI can be extremely high - comparable to those of nuclear medicine but without the use of ionizing radiation.

As with other cell tracking techniques that directly label cells using SPIOs or other

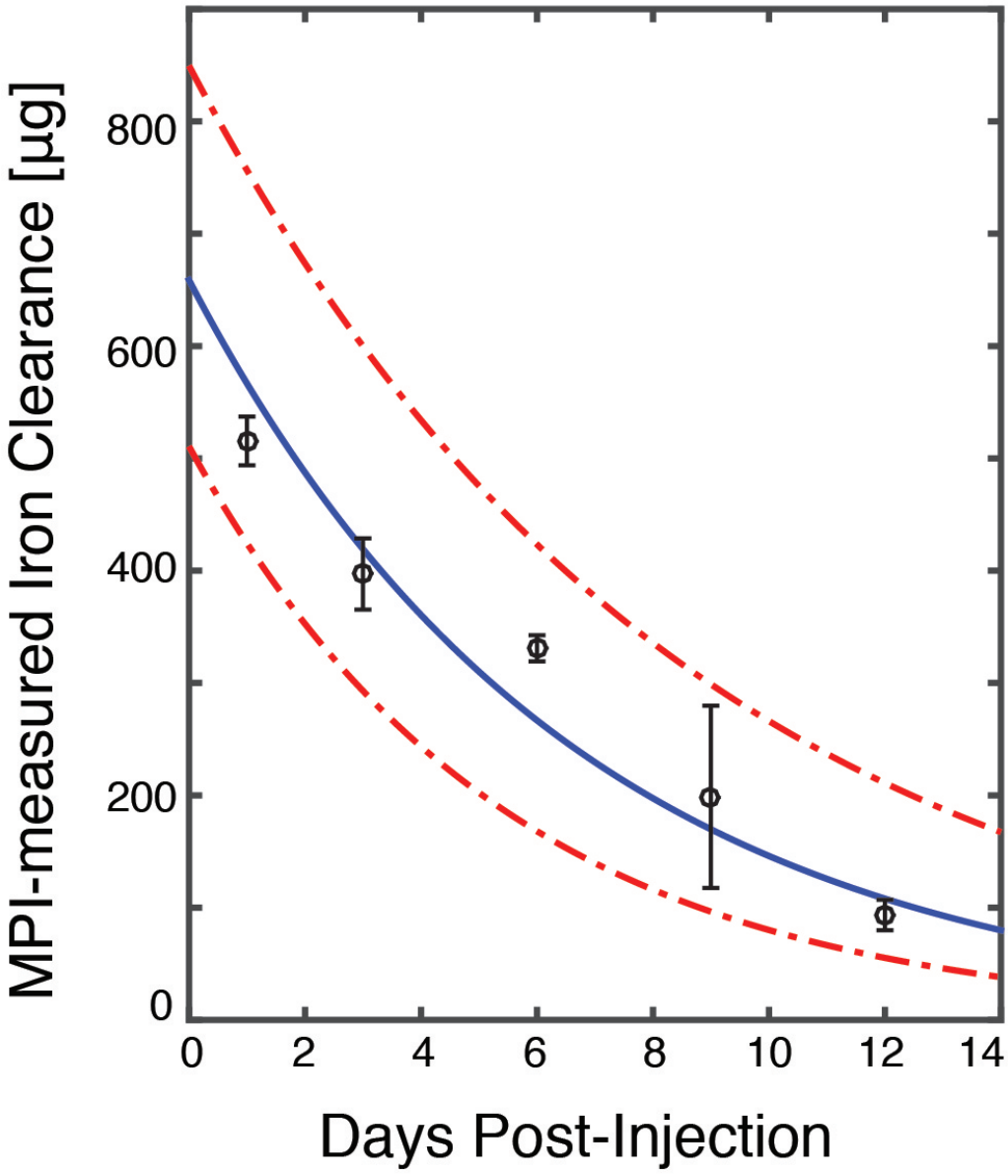

Figure 5.10: MPI quantification of *in vivo* SPIO clearance from hMSC injections. MPI measurements of *in vivo* iron clearance from labeled hMSC injections indicate *in vivo* clearance half-life at 4.6 days, with 95% confidence intervals at 3.7 and 6.0 days.

tracers, one challenge in MPI for cell tracking is in quantifying administrations of highly proliferative or apoptotic cells that may lose SPIO labels during cell division or apoptosis [25]. It is debatable whether the use of highly proliferative or undifferentiated cells are clinically feasible due to the increased risk for teratogenesis, and most clinical cell tracking

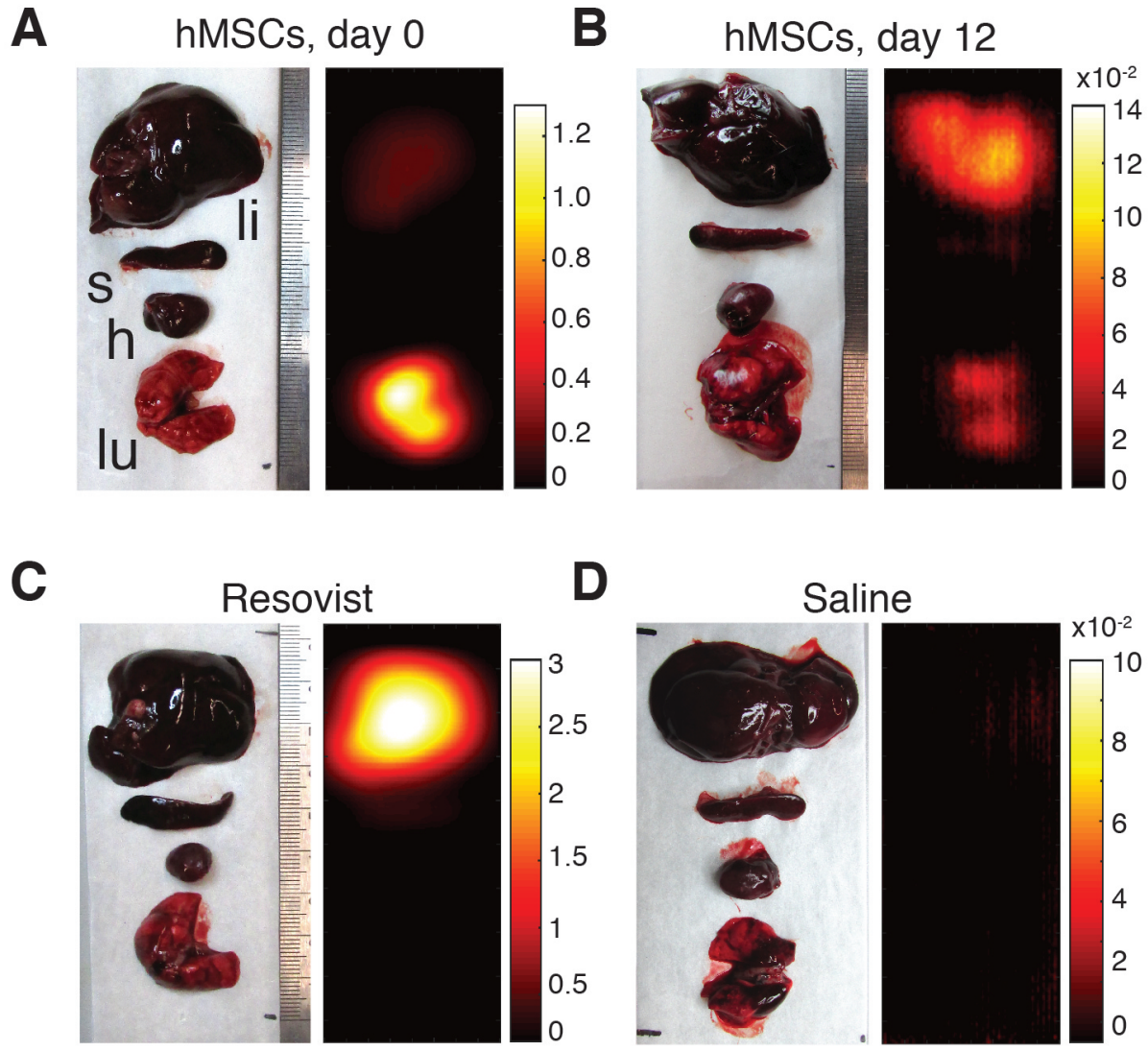

Figure 5.11: MPI analysis of postmortem SPIO biodistribution. MPI analysis of SPIO biodistribution for all groups was performed on liver, spleen, heart, and lung organs harvested postmortem. (A) MPI imaging of intravenous hMSC injections indicate localization of cells to lung tissue within one hour of injection. (B) 12 days after hMSC injection, MPI imaging shows substantial SPIO clearance and signal migration to liver and spleen. (C-D) Resovist SPIO intravenous injections localize immediately to liver and spleen, while no detectable MPI signal is found for control saline injections. The abbreviations li, s, h, and lu refer respectively to liver, spleen, heart, and lung. MPI imaging (n = 4 scans per animal): 4 × 3.75 × 10 cm FOV, 9 minute acquisition. All units are in µg Fe / mm^2.

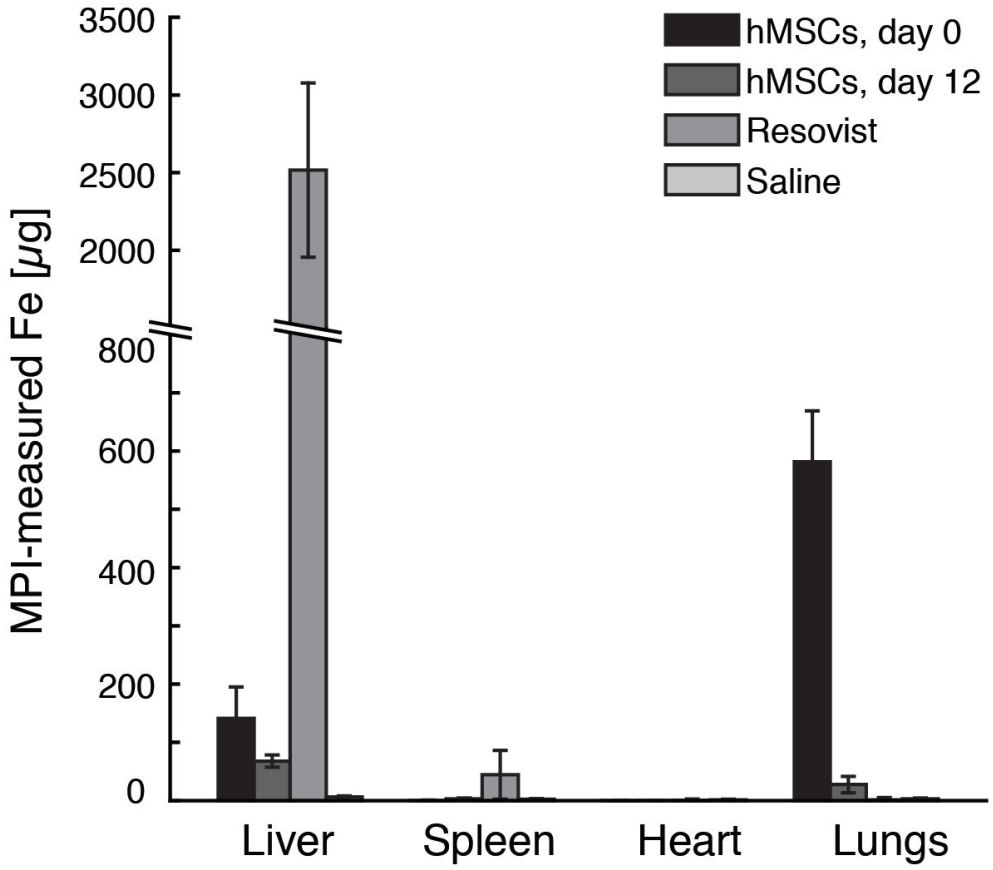

Figure 5.12: MPI-measured SPIO biodistribution for each experimental group.

studies have used differentiated adult progenitor cell models [25]. Nonetheless, several groups have attempted to engineer genetically encoded reporters for intracellular SPIO synthesis, but such approaches may incur a cost in clinical translatability and safety [27][110]. A similar challenge for direct labeling imaging techniques is the determination of cell viability *in vivo*, as the label in dead cells may be endocytosed by resident macrophages [25], leading to false positives in image contrast. In this regard, we and others have demonstrated relaxation- and aggregation-based SPIO contrast mechanisms for color-contrast MPI [111, 112], which may be used for determining the viability of implanted cells.

The spatial resolution of the 7 T/m MPI scanner used in the current study was around 1.5 mm full-width at half-maximum, which exceeds the spatial resolution of SPECT imaging and is comparable to preclinical PET imaging [25]. Many opportunities exist to further improve MPI spatial resolution, including the use of a field-free line instead of a field-free

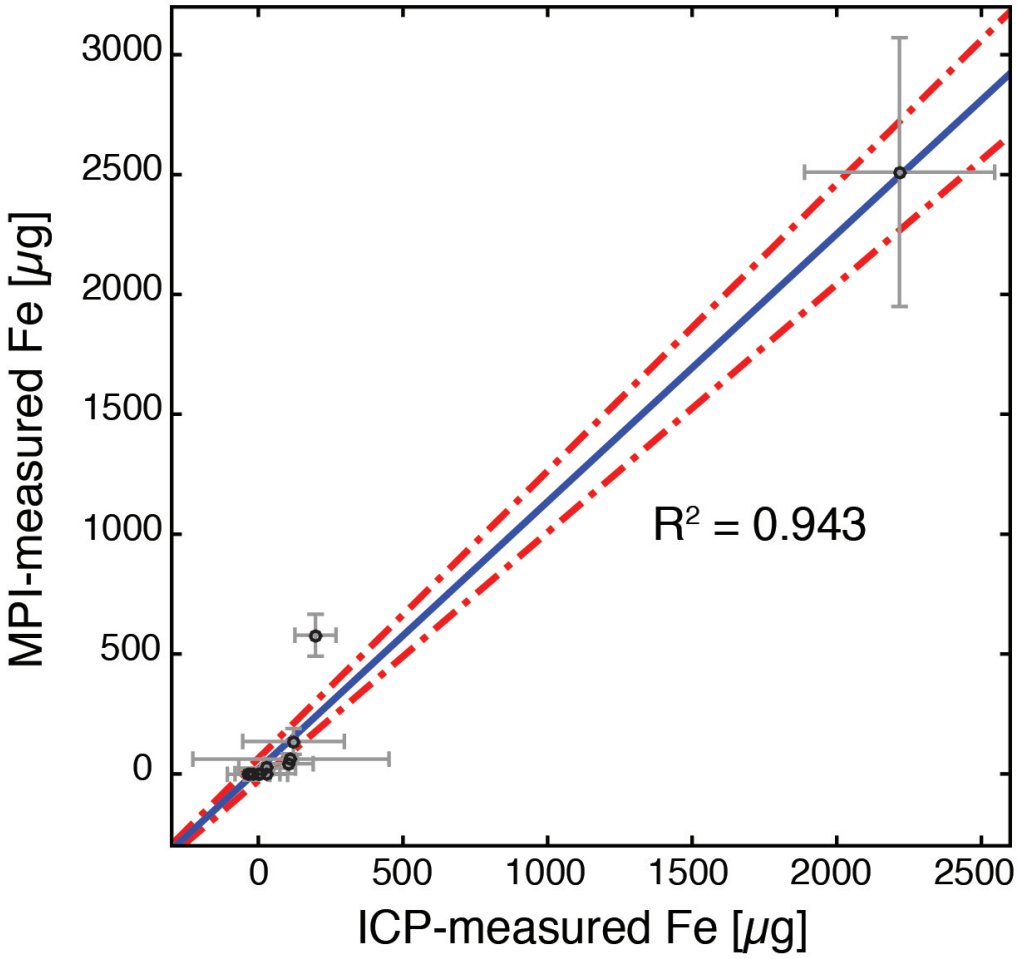

Figure 5.13: Comparison of MPI-measured SPIO biodistribution to induction-coupled plasma spectrometry. A scatterplot of MPI and ICP-measured iron content in each organ for each experimental group shows high correlation ($R^2 = 0.943$, 95% linear confidence intervals shown). Data points are mean ± s.d. for both MPI and ICP measurements for each organ for each experimental group (n = 3 animals each).

point [72] and the use of projection reconstruction MPI imaging, which has been shown to further improve spatial resolution by 50% [113]. Moreover, spatial resolution in MPI scales linearly with the applied magnetic field gradient [2, 40]. Our group has been working to develop a 6.3 T/m projection MPI scanner [114], which is expected to have a 3D MPI resolution of 600 µm using tailored SPIOs for MPI [79].

The high SNR and contrast afforded by MPI imaging may enable clinical applications beyond dynamic cell tracking and biodistribution analysis. The MPI images presented here of MSCs in the rat pulmonary microvasculature has implications for clinical MPI perfusion

imaging applications. As an example, the ventilation/perfusion (V/Q) nuclear lung scan is a standard technique for diagnosing pulmonary perfusion disorders such as pulmonary embolism. In V/Q perfusion scans, a radionuclide tag is conjugated to aggregated albumin proteins, at 100 µm in size, injected intravenously to the patient, and imaged via gamma camera or SPECT to determine radionuclide distribution and to infer perfusion defects in the lung microvasculature [115]. Pulmonary ventilation scans are performed similarly using inhaled radioactive aerosols or gases. Our results with SPIO-labeled MSCs here suggest that MPI may be applied for lung perfusion and ventilation imaging using SPIOs conjugated to macro-aggregated albumin particles or as aerosolized SPIOs [116]. MPI V/Q imaging may enable higher resolution scans with no radiation dose. Finally, MPI could enable further theranostic applications, including simultaneous imaging and delivery guidance of inhaled therapeutic aerosols for the treatment of respiratory disorders [117].

In conclusion, we have shown the use of Magnetic Particle Imaging to dynamically track the systemic administration of human mesenchymal stem cells labeled using superparamagnetic iron oxides. Here MPI imaging visualized the entrapment of MSCs in lung tissue and quantified the clearance and biodistribution of hMSCs over a 12-day period. Among existing available molecular imaging modalities, MPI shows a unique combination of highly sensitive, quantitative accuracy, and longitudinal monitoring that may accelerate the development of clinical cell therapies.

Chapter 6

Conclusions and Future Directions

In this work, I have demonstrated system electronics and hardware innovations in Magnetic Particle Imaging for improved detection sensitivity and described two applications of preclinical MPI toward *in vivo* tracking of SPIO-labeled cells. The physical basis of signal generation in MPI is completely distinct from that in other imaging and diagnostic modalities, giving it unique properties that may enable higher accuracy in diagnosing disease. Among these unique properties in MPI are extremely high image contrast for the SPIO tracer, signal linearity with tracer concentration, excellent detection sensitivity, and good patient safety. As such, MPI holds tremendous potential to accelerate preclinical research and to translate into diagnostic clinical imaging for a variety of diseases. These include angiography, perfusion imaging, cell tracking, cancer imaging, and inflammation imaging. The availability of a safe, high contrast, high sensitivity tracer-based imaging technique may greatly improve the sensitivity and specificity of diagnosis of these diseases.

Because the physical mechanisms behind MPI signal generation and detection are uniquely different from other imaging modalities, the development of MPI scanners also faces unique technical challenges that are not faced by other techniques. In this dissertation, we have described two main technical challenges that can severely limit the detection sensitivity of the MPI technique: 1) feedthrough interference from the drive coil to the MPI detector, and 2) noise in the MPI detector preamplifier.

To suppress the feedthrough interference from the MPI drive field into the detector system, I designed and implemented an actively controlled narrowband signal cancellation system that attenuates harmonic feedthrough by over 50 dB, to below the system noise floor. This active feedthrough control system is applicable to all existing MPI scanner systems, which use a simultaneous drive field/signal detection scanning methodology. However, in the future, I anticipate that other pulse sequences and MPI scanning schemes may also be used which do not include time-harmonic MPI drive fields. An example of such a scanning method may be the use of a square wave drive field, followed by detection of the temporal SPIO relaxation signal as it aligns to the drive field orientation. In such a scanning scheme, the drive field and detected signal can be temporally decoupled, obviating the need for feedthrough interference suppression.

In Chapter 3, I also showed that noise-matching schemes in MPI can enable detector noise-dominance. Detector coils in existing MPI scanners typically use a simple construction scheme comprised of solenoidal or saddle-shaped coils constructed using room temperature litz wire, with a serially attached gradiometer coil to attenuate common-mode magnetic interference from the drive field. The detector coils that we have designed in our existing preclinical MPI scanners at Berkeley are of the same configuration. However, these current detector coil designs are not optimized for noise; it is not possible to achieve body-noise dominance with these existing designs. To further improve the signal-noise ratio to body-noise dominance limits, the intrinsic electronic noise from the detector coils may need to be further reduced in future MPI scanner iterations. As an example, optimizing the detector coil geometry by improving the total copper in the detector coil (or, equivalently, increasing the total thickness of the detector coil at the cost of free bore space,) would significantly reduce the thermal noise in the coil while maintaining the coil sensitivity. A more exotic method to reduce scanner noise may be the use of cryogenically cooled detector coils and preamplifiers. At liquid nitrogen temperatures around 77 K, the total thermal noise of the detector coil and voltage noise of the preamplifier can be further reduced by a factor of two. The logistical difficulty involved in implementing such a method in existing MPI scanners is not prohibitive, making it a interesting avenue of research for the future.

To extend the usable noise-matched bandwidth in the MPI detector signal, one future approach may be to use more exotic circuit topologies in the implementation of the MPI detector preamplifier. In most existing MPI detector designs, the signal bandwidth is limited by the resonant frequency between the detector coil and the input capacitance of the high-impedance amplifier. At frequencies larger than this resonant frequency, the input impedance of the amplifier becomes lower than the source impedance of the detector coil, which reduces the input voltage signal into the preamplifier. The LC resonance also introduces a 180 degree phase shift in the detector voltage signal, which may affect the accuracy of image reconstruction. To reduce these effects introduced by the preamplifier input capacitance, one engineering approach may be to design a low-impedance preamplifier for the detector coil as a transimpedance amplifier, as in a low-noise, low-impedance common-base bipolar amplifier. The use of such a low-impedance preamplifier may achieve 3-dB noise matching to the detector coil while extending the total usable MPI bandwidth.

In Chapters 4 and 5 of this dissertation, I have also demonstrated the first uses of MPI for tracking SPIO-labeled cells *in vivo*. In these studies, I showed that MPI can be useful for tracking cell therapies for up to months in the brain and can be used to quantify and localize labeled cells administered systemically in the body. However, these initial experiments, while successful at demonstrating the quantitativeness, contrast, and sensitivity of *in vivo* MPI images for implanted cells, are in themselves only proofs-of-concepts of the potential of MPI for preclinical and clinical use. Building on the initial results from these experiments, studies in the near future may use MPI for systemic imaging of labeled cells for novel diagnostic or therapeutic applications.

One immediate application with potential for clinical translation may be to use MPI for tracking endogenously labeled circulating macrophages and immune cells. These cells

have been previously shown to migrate toward sites of inflammation and injury. Hence, a technique to systemically image the dynamic biodistribution of these cells may represent a promising avenue toward early diagnosis of inflammation-correlated diseases, such as tissue injury, autoimmune disease, myocardial infarction, and cancer.

Another application that may build upon the results presented in Chapter 5 is the use of MPI to image blood perfusion in tissue, particularly for imaging pulmonary perfusion. Ventilation/perfusion (V/Q) imaging in nuclear medicine has long been a standard technique to diagnose lung diseases such as pulmonary emboli, which can be life-threatening. In standard V/Q perfusion imaging, a large protein (typically aggregated albumin) is labeled with a nuclear tracer like Technicium-99 and injected venously, where it becomes enlodged in the pulmonary vasculature. However, these protein-tracer complexes cannot circulate to sites with abnormalities in pulmonary perfusion, such as an embolized pulmonary arteriole. Hence, dropouts in V/Q images may reveal sites of pulmonary disease. Results from our MPI study to track venous injections of labeled mesenchymal cells *in vivo* also revealed that SPIOs enlodged in pulmonary vasculature may be useful for assessing pulmonary perfusion. Therefore, the use of MPI to image venous injections of SPIO-labeled albumin aggregates may be a viable non-ionizing alternative to nuclear medicine techniques, enabling a safer method of assessing lung disease.

In conclusion, I have described in this dissertation both technical advances in Magnetic Particle Imaging that enable detector noise dominance to a preclinical MPI scanner for over 10-fold improvement in signal-noise ratio, as well as the first preclinical demonstrations of MPI for *in vivo* cell tracking. It is important to note that MPI technology is still emerging; many parameters in MPI remain to be optimized, such as pulse sequence design, gradient strength, detector circuit topology, and nanoparticle size and composition. Recent years have seen an increase in creative scanner designs and reconstruction techniques. Moreover, current state-of-the-art scanners in MPI remain confined to academic institutions for the foreseeable future. However, the future of the MPI field appears bright. The present state of MPI is reminiscent of MRI in the early 1980s; the technology is rapidly developing and, with good patient safety and the potential for high diagnostic value, has a clear path to clinical translation. Thus, the field of MPI holds abundant promise for advancing the frontiers of diagnostic medicine in detecting diseases earlier and with more sensitivity and specificity than ever before.

Bibliography

[1] Bernhard Gleich and Jürgen Weizenecker. "Tomographic imaging using the nonlinear response of magnetic particles". In: *Nature* 435.7046 (30 06 2005), pp. 1214–1217.

[2] Patrick W Goodwill and Steven M Conolly. "The X-space formulation of the magnetic particle imaging process: 1-D signal, resolution, bandwidth, SNR, SAR, and magnetostimulation". In: *IEEE Trans. Med. Imaging* 29.11 (Nov. 2010), pp. 1851–1859.

[3] J Weizenecker et al. "Three-dimensional real-time in vivo magnetic particle imaging". In: *Phys. Med. Biol.* 54.5 (July 2009), pp. L1–L10.

[4] Gerald Antoch et al. "To enhance or not to enhance? 18F-FDG and CT contrast agents in dual-modality 18F-FDG PET/CT". In: *J. Nucl. Med.* 45 Suppl 1 (Jan. 2004), 56S–65S.

[5] Edward a Neuwelt et al. "Ultrasmall superparamagnetic iron oxides (USPIOs): a future alternative magnetic resonance (MR) contrast agent for patients at risk for nephrogenic systemic fibrosis (NSF)?" In: *Kidney Int.* 75.5 (Mar. 2009), pp. 465–474.

[6] Min Lu et al. "FDA report: Ferumoxytol for intravenous iron therapy in adult patients with chronic kidney disease". In: *Am. J. Hematol.* 85.5 (May 2010), pp. 315–319.

[7] Bruce S Spinowitz et al. "Ferumoxytol for treating iron deficiency anemia in CKD". In: *J. Am. Soc. Nephrol.* 19.8 (Aug. 2008), pp. 1599–1605.

[8] Emine U Saritas et al. "Magnetic particle imaging (MPI) for NMR and MRI researchers". In: *J. Magn. Reson.* 229 (Apr. 2013), pp. 116–126.

[9] T Wawrzik et al. "Scanner setup and reconstruction for three-dimensional magnetic particle imaging". In: *SPIE Medical Imaging*. Ed. by John B Weaver and Robert C Molthen. Vol. 8672. International Society for Optics and Photonics, 29 03 2013,

[10] Patrick Vogel et al. "Traveling wave magnetic particle imaging". In: *IEEE Trans. Med. Imaging* 33.2 (Feb. 2014), pp. 400–407.

[11] Thorsten M Buzug et al. "Magnetic particle imaging: introduction to imaging and hardware realization". In: *Z. Med. Phys.* 22.4 (Dec. 2012), pp. 323–334.

[12] Kenya Murase, Ruixiao Song, and Samu Hiratsuka. "Magnetic particle imaging of blood coagulation". In: *Appl. Phys. Lett.* 104.25 (23 06 2014), p. 252409.

[13] *Bruker announces first Customer Installation of its Preclinical Magnetic Particle Imaging (MPI) Scanner at the University Medical Center Hamburg, Germany. — Bruker Corporation.* `https://www.bruker.com/nc/news-records/single-view/article/bruker-announces-first-customer-installation-of-its-preclinical-magnetic-particle-imaging-mpi-scan.html`. Accessed: 2015-6-26.

[14] Kenneth D Kochanek et al. "Deaths: final data for 2009". In: *Natl. Vital Stat. Rep.* 60.3 (29 12 2011), pp. 1–116.

[15] D A Schauer and O W Linton. "NCRP Report No. 160, Ionizing Radiation Exposure of the Population of the United States, medical exposure–are we doing less with more, and is there a role for health physicists?" In: *Health Phys.* 97.1 (July 2009), pp. 1–5.

[16] W Y Kim et al. "Coronary magnetic resonance angiography for the detection of coronary stenoses". In: *N. Engl. J. Med.* 345.26 (27 12 2001), pp. 1863–1869.

[17] Donal N Reddan et al. "Chronic kidney disease, mortality, and treatment strategies among patients with clinically significant coronary artery disease". In: *J. Am. Soc. Nephrol.* 14.9 (Sept. 2003), pp. 2373–2380.

[18] George Dangas et al. "Contrast-induced nephropathy after percutaneous coronary interventions in relation to chronic kidney disease and hemodynamic variables". In: *Am. J. Cardiol.* 95.1 (Jan. 2005), pp. 13–19.

[19] Rebecca Wertman et al. "Risk of Nephrogenic Systemic Fibrosis: Evaluation of Gadolinium Chelate Contrast Agents at Four American Universities". In: *Radiology* 248.3 (2008), pp. 799–806.

[20] Thomas Grobner and Friedrich C Prischl. "Patient characteristics and risk factors for nephrogenic systemic fibrosis following gadolinium exposure". In: *Semin. Dial.* 21.2 (Mar. 2008), pp. 135–139.

[21] Martin R Prince et al. "Incidence of nephrogenic systemic fibrosis at two large medical centers". In: *Radiology* 248.3 (Sept. 2008), pp. 807–816.

[22] Aneet Deo, Mitchell Fogel, and Shawn E Cowper. "Nephrogenic systemic fibrosis: a population study examining the relationship of disease development to gadolinium exposure". In: *Clin. J. Am. Soc. Nephrol.* 2 (2007), pp. 264–267.

[23] Lars M Bjorklund et al. "Embryonic stem cells develop into functional dopaminergic neurons after transplantation in a Parkinson rat model". In: *Proc. Natl. Acad. Sci. U. S. A.* (2002).

[24] I Jolanda M de Vries et al. "Magnetic resonance tracking of dendritic cells in melanoma patients for monitoring of cellular therapy". In: *Nat. Biotechnol.* 23.11 (2005), pp. 1407–1413.

[25] Patricia K Nguyen, Johannes Riegler, and Joseph C Wu. "Stem cell imaging: from bench to bedside". In: *Cell Stem Cell* 14.4 (2014), pp. 431–444.

[26] T Kevin Hitchens et al. “Combining perfluorocarbon and superparamagnetic iron-oxide cell labeling for improved and expanded applications of cellular MRI”. In: *Magn. Reson. Med.* (29 01 2014).

[27] Eric T Ahrens and Jeff W M Bulte. “Tracking immune cells in vivo using magnetic resonance imaging”. In: *Nat. Rev. Immunol.* 13.10 (2013), pp. 755–763.

[28] Jeff W M Bulte. “In vivo MRI cell tracking: clinical studies”. In: *AJR Am. J. Roentgenol.* 193.2 (Aug. 2009), pp. 314–325.

[29] Ali S Arbab et al. “Efficient magnetic cell labeling with protamine sulfate complexed to ferumoxides for cellular MRI”. In: *Blood* 104 (2004), pp. 1217–1223.

[30] Ka-Wing Au et al. “Effects of iron oxide nanoparticles on cardiac differentiation of embryonic stem cells”. In: *Biochem. Biophys. Res. Commun.* 379.4 (20 02 2009), pp. 898–903.

[31] Annelies Crabbe et al. “Effects of MRI contrast agents on the stem cell phenotype”. In: *Cell Transplant.* 19.8 (Jan. 2010), pp. 919–936.

[32] Charles H Cunningham et al. “Positive contrast magnetic resonance imaging of cells labeled with magnetic nanoparticles”. In: *Magn. Reson. Med.* 53.5 (May 2005), pp. 999–1005.

[33] Peter Reimer and Thomas Balzer. “Ferucarbotran (Resovist): a new clinically approved RES-specific contrast agent for contrast-enhanced MRI of the liver: properties, clinical development, and applications”. In: *Eur. Radiol.* 13.6 (2003), pp. 1266–1276.

[34] Richard Schäfer et al. “Transferrin receptor upregulation: in vitro labeling of rat mesenchymal stem cells with superparamagnetic iron oxide”. In: *Radiology* 244.2 (2007), pp. 514–523.

[35] Jong Kai Hsiao et al. “Magnetic nanoparticle labeling of mesenchymal stem cells without transfection agent: Cellular behavior and capability of detection with clinical 1.5 T magnetic resonance at the single cell level”. In: *Magn. Reson. Med.* 58.4 (2007), pp. 717–724.

[36] Hoe Suk Kim et al. “The effects of clinically used MRI contrast agents on the biological properties of human mesenchymal stem cells”. In: *NMR Biomed.* 23.November 2009 (2010), pp. 514–522.

[37] K Lüdtke-Buzug et al. “Particle-Size Distribution of Dextran- and Carboxydextran-Coated Superparamagnetic Nanoparticles for Magnetic Particle Imaging”. In: *World Congress on Medical Physics and Biomedical Engineering, September 7 - 12, 2009, Munich, Germany*. IFMBE Proceedings. Springer Berlin Heidelberg, 2009, pp. 226–229.

[38] P W Goodwill et al. “Ferrohydrodynamic relaxometry for magnetic particle imaging”. In: *Appl. Phys. Lett.* 98.26 (2011), p. 262502.

[39] Kuan Lu et al. “Linearity and shift invariance for quantitative magnetic particle imaging”. In: *IEEE Trans. Med. Imaging* 32.c (2013), pp. 1565–1575.

[40] Jürgen Rahmer et al. “Signal encoding in magnetic particle imaging: properties of the system function”. In: *BMC Med. Imaging* 9 (Jan. 2009), p. 4.

[41] Jürgen Rahmer et al. “Analysis of a 3-D system function measured for magnetic particle imaging”. In: *IEEE Trans. Med. Imaging* 31.6 (June 2012), pp. 1289–1299.

[42] Patrick W Goodwill and Steven M Conolly. “Multidimensional x-space magnetic particle imaging”. In: *IEEE Trans. Med. Imaging* 30.9 (Sept. 2011), pp. 1581–1590.

[43] Emine U Saritas et al. “Magnetostimulation limits in magnetic particle imaging”. In: *IEEE Trans. Med. Imaging* 32.9 (Sept. 2013), pp. 1600–1610.

[44] Patrick W Goodwill and Steven M Conolly. “Experimental Demonstration of X-Space Magnetic Particle Imaging”. In: *SPIE Proceedings in Medical Imaging*. Ed. by John B Weaver and Robert C Molthen. Vol. 7965. Mar. 2011,

[45] Ingo Schmale et al. “JFET Noise Modelling for MPI Receivers”. In: *Proceedings of IWMPI* (2010), pp. 148–153.

[46] P W Goodwill et al. “Narrowband Magnetic Particle Imaging”. In: *IEEE Trans. Med. Imaging* 28.8 (2009), pp. 1231–1237.

[47] Bo Zheng, Patrick Goodwill, and Steven Conolly. “Transmit filter design methods for magnetic particle imaging”. In: *SPIE Medical Imaging*. Ed. by John B Weaver and Robert C Molthen. Vol. 7965. International Society for Optics and Photonics, Mar. 2011,

[48] I Schmale et al. “An Introduction to the Hardware of Magnetic Particle Imaging”. In: *World Congress on Medical Physics and Biomedical Engineering, September 7 - 12, 2009, Munich, Germany*. Vol. 3. IFMBE Proceedings. Springer Berlin Heidelberg, 2009, pp. 450–453.

[49] Cyril Bateman. “Capacitor Sounds”. In: *Electronics World* (2002).

[50] Hans R E van Maanen Menno van der Veen. “Non-linear distortions in capacitors”. In: *Audio Engineering Society Convention Paper*. 2008.

[51] P Heinonen et al. “Properties of a thick-walled conducting enclosure in low-frequency magnetic shielding”. In: *J. Phys. E* 13.5 (1980), pp. 569–570.

[52] J L Dawson and T H Lee. “Automatic phase alignment for a fully integrated Cartesian feedback power amplifier system”. In: *IEEE J. Solid-State Circuits* 38.12 (Dec. 2003), pp. 2269–2279.

[53] Joel L Dawson and Thomas H Lee. “Cartesian feedback for RF power amplifier linearization”. In: *Proceedings of the American Control Conference*. Vol. 1. scl.hanyang.ac.kr, 2004, pp. 361–366.

[54] Simon R Cherry, James A Sorenson, and Michael E Phelps. *Physics in nuclear medicine*. Elsevier Health Sciences, 2012.

[55] Y Netzer. *The design of low-noise amplifiers*. 1981.

[56] W M Leach. "Fundamentals of low-noise analog circuit design". In: *Proc. IEEE* 82.10 (1994), pp. 1515–1538.

[57] Peter J Fish. *Electronic noise and low noise design*. McGraw-Hill Ryerson, Limited, 1994.

[58] Henry Ott. *Electromagnetic Compatibility Engineering*. John Wiley & Sons, 24 08 2009.

[59] C D Motchenbacher and Joseph Alvin Connelly. *Low noise electronic system design*. J. Wiley & Sons, 29 06 1993.

[60] J O Lekkala and J A V Malmivuo. "Noise reduction using a matching input transformer (magnetic field measurement system)". In: *J. Phys. E* 14.8 (1981), pp. 939–942.

[61] Paul Horowitz and Winfield Hill. *The Art of Electronics*. Cambridge University Press, 30 03 2015.

[62] A Macovski. "Noise in MRI". In: *Magn. Reson. Med.* 36 (1996), pp. 494–497.

[63] J Weizenecker, J Borgert, and B Gleich. "A simulation study on the resolution and sensitivity of magnetic particle imaging". In: *Phys. Med. Biol.* 52.21 (July 2007), pp. 6363–6374.

[64] R M Fano. "Theoretical limitations on the broadband matching of arbitrary impedances". In: *J. Franklin Inst.* 249.2 (Feb. 1950), pp. 139–154.

[65] D I Hoult. "The principle of reciprocity in signal strength calculations—A mathematical guide". In: *Concepts Magn. Reson.* 12.4 (Jan. 2000), pp. 173–187.

[66] H A Wheeler. "Simple Inductance Formulas for Radio Coils". In: *Radio Engineers, Proceedings of the Institute of* 16.10 (Oct. 1928), pp. 1398–1400.

[67] Denis J-M Poussart. "Low-Level Average Power Measurements: Noise Figure Improvements Through Parallel or Series Connection of Noisy Amplifiers". In: *Rev. Sci. Instrum.* 44.8 (1973), p. 1049.

[68] John Ardizzoni. *A Practical Guide to High-Speed Printed-Circuit-Board Layout*. Tech. rep. Analog Dialogue 39-09. Texas Instruments, Sept. 2005.

[69] James Baker-Jarvis and Sung Kim. *The Interaction of Radio-Frequency Fields with Dielectric Materials at Macroscopic to Mesoscopic Scales*. 2012.

[70] J W M Bulte et al. "Developing Cellular Mpi: Initial Experience". In: *Magnetic Nanoparticles - Particle Science, Imaging Technology, and Clinical Applications - Proceedings of the First International Workshop on Magnetic Particle Imaging* (2010), pp. 201–204.

[71] Justin J Konkle et al. “Projection reconstruction magnetic particle imaging”. In: *IEEE Trans. Med. Imaging* 32.2 (Feb. 2013), pp. 338–347.

[72] Patrick W Goodwill et al. “Projection x-space magnetic particle imaging”. In: *IEEE Trans. Med. Imaging* 31.5 (May 2012), pp. 1076–1085.

[73] Ying Meng et al. “Characterization of integrin engagement during defined human embryonic stem cell culture”. In: *FASEB J.* 24.4 (Apr. 2010), pp. 1056–1065.

[74] Stuart M Chambers et al. “Highly efficient neural conversion of human ES and iPS cells by dual inhibition of SMAD signaling”. In: *Nat. Biotechnol.* 27.3 (Mar. 2009), pp. 275–280.

[75] Donatella De Feo et al. “Neural stem cell transplantation in central nervous system disorders”. In: *Curr. Opin. Neurol.* 25.3 (2012), pp. 322–333.

[76] Kon Chu et al. “Human neural stem cells can migrate, differentiate, and integrate after intravenous transplantation in adult rats with transient forebrain ischemia”. In: *Neurosci. Lett.* 343.2 (May 2003), pp. 129–133.

[77] S Kelly et al. “Transplanted human fetal neural stem cells survive, migrate, and differentiate in ischemic rat cerebral cortex”. In: *Proc. Natl. Acad. Sci. U. S. A.* 101.32 (Oct. 2004), pp. 11839–11844.

[78] Jing Guo et al. “In vivo evaluation of cerebral transplantation of resovist-labeled bone marrow stromal cells in Parkinson’s disease rats using magnetic resonance imaging”. In: *Appl. Biochem. Biotechnol.* 163.5 (Mar. 2011), pp. 636–648.

[79] R Ferguson et al. “Magnetic Particle Imaging with Tailored Iron Oxide Nanoparticle Tracers”. In: *IEEE Trans. Med. Imaging* 0062.c (2014), pp. 1–1.

[80] R Matthew Ferguson et al. “Optimizing magnetite nanoparticles for mass sensitivity in magnetic particle imaging”. In: *Med. Phys.* 38.3 (2011), p. 1619.

[81] a G Roca et al. “Progress in the preparation of magnetic nanoparticles for applications in biomedicine”. In: *J. Phys. D Appl. Phys.* 42.22 (21 11 2009), p. 224002.

[82] Aidin Lak et al. “Synthesis of Single-Core Iron Oxide Nanoparticles as a Tracer for Magnetic Particle Imaging”. In: *International Workshop on Magnetic Particle Imaging* (2012), pp. 93–97.

[83] D Eberbeck et al. “How the size distribution of magnetic nanoparticles determines their magnetic particle imaging performance”. In: *Appl. Phys. Lett.* 98.18 (2011), p. 182502.

[84] Dietmar Eberbeck, Lutz Trahms, and Harald Kratz. “Evaluation of Different Magnetic Particle Systems with Respect to Its MPI”. In: *International Workshop on Magnetic Particle Imaging*. 2012, pp. 53–57.

[85] D E Markov et al. “Human erythrocytes as nanoparticle carriers for magnetic particle imaging”. In: *Phys. Med. Biol.* 55.21 (July 2010), pp. 6461–6473.

[86] J Rahmer et al. “Nanoparticle encapsulation in red blood cells enables blood-pool magnetic particle imaging hours after injection”. In: *Phys. Med. Biol.* 58.12 (21 06 2013), pp. 3965–3977.

[87] Rui Sun et al. “Physical and biological characterization of superparamagnetic iron oxide- and ultrasmall superparamagnetic iron oxide-labeled cells: a comparison”. In: *Invest. Radiol.* 40.8 (2005), pp. 504–513.

[88] Laura R Croft, Patrick W Goodwill, and Steven M Conolly. “Relaxation in x-space magnetic particle imaging”. In: *IEEE Trans. Med. Imaging* 31.12 (Dec. 2012), pp. 2335–2342.

[89] Adam M Rauwerdink and John B Weaver. “Viscous effects on nanoparticle magnetization harmonics”. In: *J. Magn. Magn. Mater.* 322.6 (Mar. 2010), pp. 609–613.

[90] G M Van Buul et al. “Ferumoxides-protamine sulfate is more effective than ferucarbotran for cell labeling: Implications for clinically applicable cell tracking using MRI”. In: *Contrast Media Mol. Imaging* 4.April (2009), pp. 230–236.

[91] Rachael a Panizzo et al. “In vivo magnetic resonance imaging of endogenous neuroblasts labelled with a ferumoxide-polycation complex”. In: *Neuroimage* 44.4 (15 02 2009), pp. 1239–1246.

[92] Moritz F Kircher, Sanjiv S Gambhir, and Jan Grimm. “Noninvasive cell-tracking methods”. In: *Nat. Rev. Clin. Oncol.* 8.11 (Nov. 2011), pp. 677–688.

[93] Walter J Rogers, Craig H Meyer, and Christopher M Kramer. “Technology insight: in vivo cell tracking by use of MRI”. In: *Nat. Clin. Pract. Cardiovasc. Med.* 3.10 (Oct. 2006), pp. 554–562.

[94] Elke Eggenhofer et al. “The life and fate of mesenchymal stem cells”. In: *Front. Immunol.* 5.MAY (2014), pp. 1–6.

[95] Martin J Hoogduijn et al. “Mesenchymal stem cells induce an inflammatory response after intravenous infusion”. In: *Stem Cells Dev.* 22.21 (2013), pp. 2825–2835.

[96] Matthew T Harting et al. “Intravenous mesenchymal stem cell therapy for traumatic brain injury”. In: *J. Neurosurg.* 110.6 (2009), pp. 1189–1197.

[97] Yaojiong Wu and Robert C H Zhao. “The role of chemokines in mesenchymal stem cell homing to myocardium”. In: *Stem Cell Rev.* 8.1 (Mar. 2012), pp. 243–250.

[98] Jianfeng Ge et al. “The Size of Mesenchymal Stem Cells is a Significant Cause of Vascular Obstructions and Stroke”. In: *Stem Cell Reviews and Reports* 10 (2014), pp. 295–303.

[99] E Eggenhofer et al. “Mesenchymal stem cells are short-lived and do not migrate beyond the lungs after intravenous infusion”. In: *Front. Immunol.* 3 (26 09 2012), p. 297.

[100] Uwe M Fischer et al. “Pulmonary passage is a major obstacle for intravenous stem cell delivery: the pulmonary first-pass effect”. In: *Stem Cells Dev.* 18.5 (June 2009), pp. 683–692.

[101] Jizong Gao et al. “The dynamic in vivo distribution of bone marrow-derived mesenchymal stem cells after infusion”. In: *Cells Tissues Organs* 169 (2001), pp. 12–20.

[102] Vasilis Ntziachristos et al. “Looking and listening to light: the evolution of whole-body photonic imaging”. In: *Nat. Biotechnol.* 23.3 (Mar. 2005), pp. 313–320.

[103] Serge Grabtchak, Logan G Montgomery, and William M Whelan. “Optical absorption and scattering properties of bulk porcine muscle phantoms from interstitial radiance measurements in 650–900 nm range”. In: *Phys. Med. Biol.* 59 (2014), pp. 2431–2444.

[104] Dara L Kraitchman et al. “Dynamic imaging of allogeneic mesenchymal stem cells trafficking to myocardial infarction”. In: *Circulation* 112.10 (2005), pp. 1451–1461.

[105] S a Nehmeh et al. “Effect of respiratory gating on reducing lung motion artifacts in PET imaging of lung cancer”. In: *Med. Phys.* 29.3 (2002), pp. 366–371.

[106] S Schrepfer et al. “Stem Cell Transplantation: The Lung Barrier”. In: *Transplant. Proc.* 39.2 (2007), pp. 573–576.

[107] Clemens Bos et al. “In Vivo MR Imaging of Intravascularly Injected Magnetically Labeled Mesenchymal Stem Cells in Rat Kidney and Liver”. In: *Radiology* 233.3 (2004), pp. 781–789.

[108] Naveen Gupta et al. “Intrapulmonary delivery of bone marrow-derived mesenchymal stem cells improves survival and attenuates endotoxin-induced acute lung injury in mice”. In: *J. Immunol.* 179.3 (Jan. 2007), pp. 1855–1863.

[109] Mauricio Rojas et al. “Bone Marrow–Derived Mesenchymal Stem Cells in Repair of the Injured Lung”. In: *Am. J. Respir. Cell Mol. Biol.* 33.2 (Aug. 2005), pp. 145–152.

[110] Moriel H Vandsburger et al. “MRI reporter genes: applications for imaging of cell survival, proliferation, migration and differentiation”. In: *NMR Biomed.* 26.7 (July 2013), pp. 872–884.

[111] D Hensley et al. “Preliminary experimental X-space color MPI”. In: *Magnetic Particle Imaging (IWMPI), 2015 5th International Workshop on*. Mar. 2015, pp. 1–1.

[112] J Rahmer et al. “First experimental evidence of the feasibility of multi-color magnetic particle imaging”. In: *Phys. Med. Biol.* 60.5 (July 2015), pp. 1775–1791.

[113] Justin Konkle, Patrick Goodwill, and Steven Conolly. “Development of a Field Free Line Magnet for Projection MPI”. In: *SPIE Proceedings in Medical Imaging*. Ed. by John B Weaver and Robert C Molthen. Vol. 7965. Mar. 2011,

[114] E Y Yu, P W Goodwill, and S M Conolly. “Preliminary characterization of a laminated iron-core 6.3 T/m FFL magnet”. In: *Magnetic Particle Imaging (IWMPI), 2015 5th International Workshop on*. Mar. 2015, pp. 1–1.

[115] B J McNeil. “A diagnostic strategy using ventilation-perfusion studies in patients suspect for pulmonary embolism”. In: *J. Nucl. Med.* 17.7 (July 1976), pp. 613–616.

[116] Kohei Nishimoto et al. “Application of Magnetic Particle Imaging to Pulmonary Imaging Using Nebulized Magnetic Nanoparticles”. In: *Open Journal of Medical Imaging* 5.02 (2015), p. 49.

[117] Petra Dames et al. “Targeted delivery of magnetic aerosol droplets to the lung”. In: *Nat. Nanotechnol.* 2.8 (Aug. 2007), pp. 495–499.